TECHNICAL ANALYSIS OF SOLID OXIDE ELECTROLYSIS CELL (SOEC) AND FISCHER-TROPSCH SYNTHESIS (FTS) PROCESS FOR CO_2 CONVERSION INTO SYNGAS AND GASOLINE FUEL THROUGH MODELLING AND SIMULATION

By:

Ariane D. Noula Kamkeng

Supervisor: Prof Meihong Wang

A thesis submitted in partial fulfilment of the requirement for the degree of

Doctor of Philosophy

Department of Chemical and Biological Engineering

Faculty of Engineering

The University of Sheffield

April 2022

Acknowledgment

Abstract

Within the current global energy systems, fossil fuels are one of the most important requirements for daily activities (such as transportation, power generation and heating) leading to 36.4 billion tons of CO_2 released into the atmosphere worldwide in 2021. This resulted in serious concerns regarding global warming and climate change. The Intergovernmental Panel on Climate Change (IPCC) recommends decreasing CO_2 emissions to maintain the global temperature increase below 1.5℃ by 2100. In this context, Power-to-fuels technologies arise as a potential solution for meeting CO_2 reduction targets through the deployment of CO_2-neutral fuels.

This research aims to investigate CO_2 conversion into syngas and gasoline fuel via CO_2/H_2O co-electrolysis in solid oxide electrolysis cells (SOECs), Fischer-Tropsch synthesis (FTS) and direct CO_2-FTS processes through modelling and simulation approach. The critical review of previous studies revealed that degradation issues in SOECs and the low yield of liquid fuels (C_{5+}) during the CO_2-FTS process are still of great concerns for commercial applications. Furthermore, no modelling studies were found in the open literature integrating SOEC structural degradation. Existing modelling studies on CO_2-FTS process to liquid fuels are based on experimental data with up to 78% selectivity to gaseous hydrocarbons (C_1 to C_4). This highlighted the need for more accurate SOEC and CO_2-FTS models to find effective strategies to improve SOEC long-term performance as well as CO_2 conversion and C_{5+} yield.

In this study, A 1-D pseudo-dynamic model of planar SOEC was developed and implemented in Aspen Plus® using Fortran® routines. The model is based on first principles and incorporates electrochemical/chemical reactions during CO_2/H_2O co-electrolysis and structural degradation of Ni-YSZ cathode, YSZ electrolyte and LSM-YSZ anode materials. Model validation was carried out for both SOEC performance and degradation for different feed gas compositions, temperatures (750–850℃) and current densities (0.5–1.5 A/cm²). The effects of operating conditions and deterioration of SOEC components on syngas production efficiency and SOEC long-term performance were studied. The results indicated that higher operating temperatures and current densities initially improve SOEC performance but lead to faster degradation rates. SOEC degradation is essentially due to LSM-YSZ anode delamination with an average degradation rate of 3.96 %/1000hrs after 20,000 hours of operation. Decreasing YSZ surface area at the cathode, coating the interconnect surface and decreasing La/Sr ratio on the anode side are necessary for achieving SOEC degradation rates below 1.0 %/1000hrs.

A steady-state model of the CO_2-FTS process was also developed and validated in Aspen Plus® using Fortran® routines. The model is based on first principles and a modified Anderson–Schulz–Flory (ASF) theory to predict gasoline range hydrocarbons (C_5-C_{11}). Model validation was performed for two H_2/CO_2 feed ratios (1.0 and 3.0). Two process configurations, including a three-stage reactor in series and a single reactor with recycle, were considered for ex-situ water removal to carry out performance analysis and comparison. Both CO_2-FTS process configurations showed significant improvements in CO_2 conversion with up to 61.0% gasoline yield. Though the single reactor with recycle achieved a higher CO_2 conversion and gasoline production rate than the 3-stage reactor in series, the comparative analysis at the same CO_2 conversion of 71.5% revealed that both process configurations have a similar process efficiency of roughly 66.4%.

An integrated SOEC-FTS process for gasoline fuel synthesis was simulated in Aspen Plus® software. Two configurations (open-loop system and recycle system with material recirculation to the FTS section) were considered for performance analysis. A comparative analysis (in terms of reactant flowrates, CO_2 conversion, gasoline yield, energy requirement and overall system efficiency) was performed between integrated SOEC-FTS with recycle to the FTS section and direct CO_2-FTS using reactors in series a single reactor with recycle. It was observed that SOEC efficiency was lower than that of previous studies arising from SOEC degradation rate considerations. The integrated SOEC-FTS process achieved the highest CO_2 conversion and gasoline yield but had the lowest process efficiency of 43.6%. However, the process efficiency of the 3-stage CO_2-FTS reactors in series and single CO_2-FTS reactor with recycle decreased by 62.7% and 60.4% respectively when considering the energy required for H_2 production.

The findings from this PhD research helps to promote the production of syngas and gasoline fuel from atmospheric CO_2 at commercial-scale.

Keywords:

Publications and Presentations from this PhD Thesis

Part of this thesis has been published in the following peer-reviewed journals:

- **Kamkeng, A. D. N.**, Wang, M., Hu, J., Du, W. and Qian, F. (2021). Transformation technologies for CO_2 utilisation: Current status, challenges and future prospects. *Chemical Engineering Journal*, 409: 128138.

- **Kamkeng, A. D. N.** and Wang, M. (2022). Long-term performance prediction of solid oxide electrolysis cell (SOEC) for CO_2/H_2O co-electrolysis considering structural degradation through modelling and simulation. *Chemical Engineering Journal*, 429: 132158.

Planned publications from this thesis include:

- **Kamkeng, A. D. N.** and Wang, M. Technical analysis of the modified Fischer-Tropsch synthesis process for direct CO_2 conversion into gasoline fuel: Performance improvement via ex-situ water removal.

- **Kamkeng, A. D. N.** and Wang, M. Power-to-fuels via integrated solid oxide electrolysis cell (SOEC) with Fischer-Tropsch synthesis (FTS) and direct CO_2-FTS process: A comparative analysis for CO_2 conversion into gasoline fuel.

Conference Presentation:

- **Kamkeng, A. D. N.**, Wang, M. and Aneke, M. (2019). CO_2/H_2O co-electrolysis in solid oxide electrolysis cells (SOECs): A modelling approach. *UKCCSRC Programme Conference*, Edinburgh Centre for Carbon Innovation, Edinburgh, United Kingdom, 4th – 5th, September 2019

- **Kamkeng, A. D. N.** and Wang, M. (2021). A model-based understanding of degradation in solid oxide electrolysis cells during syngas production. *ChemEng Day UK*, University of Bradford, Bradford, United Kingdom, 7th – 8th, April 2021 (Online)

- **Kamkeng, A. D. N.** and Wang, M. (2021). CO_2 transformation technologies and long-term performance of solid oxide electrolysis cells for CO_2/H_2O co-electrolysis. *Postgraduate Research Conference*, The University of Sheffield, Sheffield, United Kingdom, 25th, June 2021 (Online)

Table of Contents

List of Figures

List of Tables

Nomenclatures

A_{cell}	Cell active area (cm^2)
A_{tot}	Total active area of SOEC (cm^2)
A_{YSZ}	YSZ surface area per gram of composite (m^2/g)
b	Carbon number at break point
c	Olefin desorption rate constant
C and C'	Temperature-independent constant
d_i	Thickness of component i (cm)
D_{LSM}	LSM surface diffusion (cm^2/hr)
$E_{a,i}$	Component i activation energy (J/mol)
E_i	Activation energy for component i growth (J/mol)
E_{Sin}	Activation energy for sintering (J/mol)
F	Faraday constant (96,485 J/V.mol)
f_1 and f_2	fractions of hydrocarbons on each side of carbon break point
HHV_i	Higher heating value of component i (W and MW)
I	Current (A)
j	Current density (A/cm^2)
j_0	Exchange current density (A/cm^2)
$K_{g,i}$	Weight gain rate for component i growth (g/cm^4.hr)
K_i	Adsorption constant
k_i	Kinetic constant of hydrocarbon i formation
K_i^0	Standard adsorption constant
$K_{p,i}$	Parabolic constant for component i (cm^2/hr)
L_{TPB}	TPB length or TPB density (μm^{-2})

M_i	Molar mass of hydrocarbon i
$\bar{M}$	Average molar mass of hydrocarbon mixture
n	Number of electrons transferred per electrolysis
N	Number of particles within an electrode
N_{cell}	Number of cells in SOEC stack
$\dot{N}_{HC}$	Total molar extent of produced hydrocarbons (kmol/hr)
$\dot{n}_{\text{HC}_i}$	Molar extent of hydrocarbon i (kmol/hr)
$\dot{N}_{\text{in}}$	Cathode inlet flowrate (mol/sec)
$\dot{n}_{\text{i}_{\text{in}}}$ and $\dot{n}_{\text{i}_{\text{out}}}$	Inlet and outlet mole flow of FTS component i (kmol/hr)
$\mathcal{P}_{\text{cell}}$	Power utilisation per cell (W)
$\mathcal{P}_i$	Power utilisation in process i (MW)
P_{std} and P	Standard and operating pressure (bar)
Q_i	Enthalpy of adsorption of component i (J/mol)
R	Universal gas constant (8.314 J/mol.K)
R_i	Ohmic resistance of component i
r_{Ni} and r_{YSZ}	Ni and YSZ radius (m)
$R_{\text{Y3+}}$	Ionic radius (Å)
S_i	Selectivity towards hydrocarbon i (%)
T	Operating temperature (K)
t	Operating time (hr)
U	Operating voltage (V)
U_{EQ}	Equilibrium voltage (V)
U_{P}	Polarisation overpotential (V)
U_{S}	Ohmic overpotential (V)

V	Volume of Ni particles in the cathode electrode (m^3)
V_i	Volume fraction of component i
V_{Ni}^c	Ni volume fraction at percolation
W_i	Weight fraction of component i
X_i	Conversion of reactant i
x_i	Mole fraction of component i
X_R	Reactant conversion
Y_i	Yield of hydrocarbon i (%)
Z	Average particle coordination number
$Z_{YSZ,YSZ}$	Coordination number between YSZ particles

Greek letters

α	Chain growth probabilities
β	Charge transfer coefficient
$\Delta G_{f,i}$	Gibbs free energy of formation for component i (J/mol)
ΔH	Enthalpy change of reaction (J/mol)
ΔS	Entropy change of reaction (J/mol)
ΔU	Degradation rate (%/1000hrs)
η_i	Efficiency of process i (%)
η_{syngas}	Syngas production efficiency (%)
θ_i	Surface coverage fraction of component i
λ	Fitting parameter
ρ_i	Density of component i (g/cm^3)
σ_i	Conductivity of component i (S/cm)
σ_i^0	Pre-exponential factor for component i (S/cm)

τ Time constant (hr)

Φ Porosity

Abbreviations

ARENA	Australian Renewable Energy Agency
ASF	Anderson Schulz Flory
BOP	Balance-of-plant
BTL	Biomass to liquid fuels
CAPEX	Capital expenditures
CBTL	Coal and biomass to liquid fuels
CCS	Carbon capture and storage
CCUS	Carbon capture, utilisation and storage
CFB	Circulating fluidized-bed
CFD	Computational fluid dynamics
CGO	Ceria gadolinium oxide
CNT	Carbon nanotube
COS	Chromium oxide scale
CSIRO	Commonwealth Scientific and Industrial Research Organisation
CSTR	Continuous stirred tank reactor
DAC	Direct air capture
ECo	Efficient Co-Electrolyser
EG	Entrained gasification
EOR	Enhanced oil recovery
FBR	Fixed-bed reactor
FFB	Fixed fluidized-bed
FTS	Fischer-Tropsch synthesis
FTY	Fischer-Tropsch yield

GHSV	Gas hourly space velocity
GTL	Natural gas to liquid fuels
HC	Hydrocarbon
HHV	Higher heating value
HT	High temperatures
IEA	International Energy Agency
INL	Idaho National Laboratory
IPCC	Intergovernmental Panel on Climate Change
LHHW	Langmuir Hinshelwood Hougen Watson
LSC	Lanthanum strontium cobalt
LSCF	Lanthanum strontium cobalt iron oxide
LSM	Lanthanum strontium manganite
LT	Low temperatures
LZO	Lanthanum zirconate oxide
MCR	Microchannel reactor
MEA	Membrane electrode assembly
MLR	Monolithic loop reactor
MR	Membrane reactor
NTP	Non-thermal plasma
OPEC	Organization of the Petroleum Exporting Countries
OPEX	Operational expenditures
PEM	Proton exchange membrane
RC	Reactant conversion
RE	Relative error

RON	Research octane number
RWGS	Reverse water gas shift
SBCR	Slurry bubble column reactor
CSTR	Continuous stirred-tank reactor
SDC	Samaria-doped ceria
SEM	Scanning electron microscope
SOEC	Solid oxide electrolysis cell
TEA	Technical and economic analysis
TOFC	Topsøe Fuel Cells A/S
TPB	Triple phase boundary
TRL	Technology readiness level
WGS	Water gas shift
YSZ	Yttria-stabilised zirconia

1.   Introduction

1.1. Background[1]

1.1.1. CO₂ emissions, CCS and CCUS

The excessive use of fossil fuels in many anthropogenic activities (such as transportation, cement manufacturing and power generation) resulted in serious concerns regarding CO_2 emissions into the atmosphere. As of 2021, CO_2 emissions from fossil fuels worldwide reached 36.4 Gt (Figure 1.1) which was roughly 4.2 times higher than CO_2 emitted in 1959 (Carbon Brief, 2021). It has been widely recognised that CO_2 emissions considerably contribute to climate change and global warming which have severe impacts on the environment, for instance, increase in ocean and sea levels, acid rains, melting glaciers and changes in weather patterns (Khozema et al., 2020).
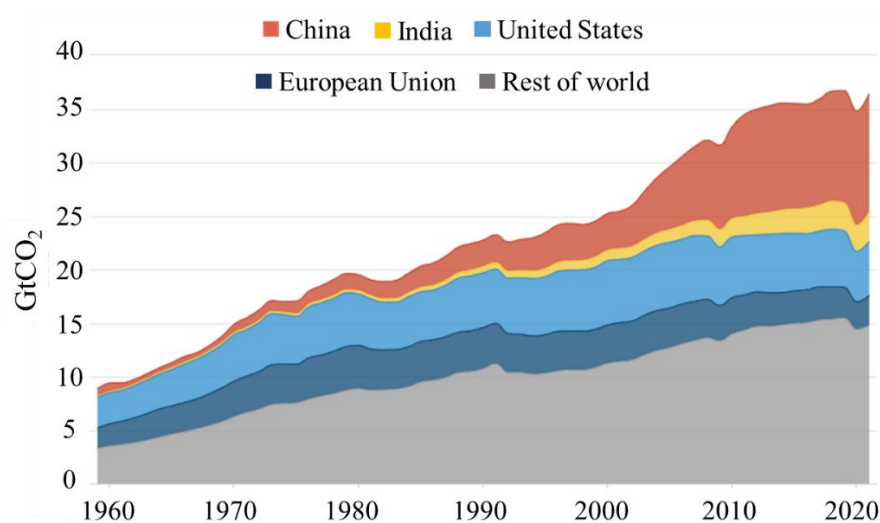
Figure 1.1: Global CO_2 emissions from fossil fuels between 1959 and 2021 (Carbon Brief, 2021)

As a result, the Intergovernmental Panel on Climate Change (IPCC) recommended decreasing CO_2 emissions to net-zero around 2050 so that the global temperature increase can be maintained below 1.5°C by 2100 (IPCC, 2018). Different approaches have been proposed for reducing CO_2 emissions including improvement of energy conservation and efficiency, deployment of renewable energies, use of low carbon fuels and carbon capture and storage

---

[1] Most of this Section has been published in Kamkeng, A. D. N., Wang, M., Hu, J. et al. (2021) Transformation technologies for CO_2 utilisation: Current status, challenges and future prospects. Chemical Engineering Journal, 409, 128138

(CCS). The latter is considered as a viable approach for achieving CO_2 emission reductions (Leung et al., 2014).

CCS refers to as CO_2 capture from large emission sources (such as cement manufacturing, power generation and oil refinery plants), transportation and storage in an underground geological formation (Wang et al., 2011). Nineteen CCS facilities are operating worldwide at a commercial-scale since 2019, with four more under construction. However, the reported CCS plants have an annual capture capacity of approximately 40 $MtCO_2$ representing 0.1% of the global CO_2 emissions (Global CCS Institute, 2019). Moreover, the International Energy Agency (IEA) predicted in 2011 that at least 60 CCS projects should be commercially deployed by 2020 to achieve 19% of CO_2 emission reduction targets (IEA, 2011). It was found that the slow deployment of commercial CCS technologies is essentially due to their high costs (Heuberger et al., 2016).

Therefore, the term CCS became CCUS (Carbon capture, utilisation and storage) wherein in addition to CO_2 storage, the economic value of the captured CO_2 is promoted through utilisation (Rodrigues et al., 2015). Permanent CO_2 storage via CCS and the economic advantage of CO_2 utilisation have made CCUS a more suitable concept for meeting CO_2 reduction targets. Nevertheless, CCS approaches are beyond the scope of this research, good CCS discussions are available elsewhere (Heuberger et al., 2016; Lei et al., 2020) and further discussions focus on CO_2 utilisation technologies.
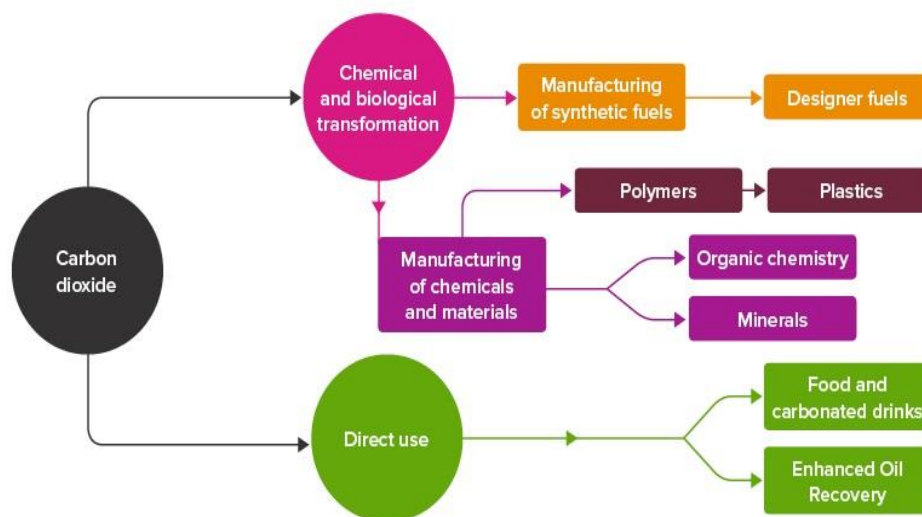
Figure 1.2: Direct and indirect CO_2 utilisation (The Royal Society, 2017)

CO_2 utilisation is divided into direct and indirect applications (Figure 1.2). Direct applications consist of using CO_2 at its pure state and without any transformation. A few examples include food preservation, carbonated drinks, enhanced oil recovery (EOR) and fire extinguishers

(Jarvis and Samsatli, 2018). On the other hand, indirect CO_2 utilisation refers to as CO_2 conversion into fuels, chemicals and materials via biological and chemical processes (Styring and Armstrong, 2011).

The total amount of CO_2 used via direct applications worldwide was estimated at 42.4 $MtCO_2$ in 2016 which corresponded to roughly 18% of CO_2 consumed through indirect applications (Aresta et al., 2016). Furthermore, it was forecast that CO_2 demand for direct uses will remain constant since its industry is quite stable (Naims, 2016; Norhasyima and Mahlia, 2018). In contrast, indirect CO_2 applications were predicted to exceed 332 $MtCO_2$ by 2030 (Aresta et al., 2016). Hence, CO_2 utilisation via transformation represents a better way of achieving CO_2 emission reduction targets.

1.1.2. Challenges for CO_2 conversion

Thermodynamically, the CO_2 molecule is very stable owing to the strong double bonds between carbon and oxygen atoms. As shown in Figure 1.3, products from CO_2 conversion have a much higher Gibbs free energy of formation than that of CO_2 ($\Delta G° = $ -394.4 kJ/mol) (Aresta et al., 2014).
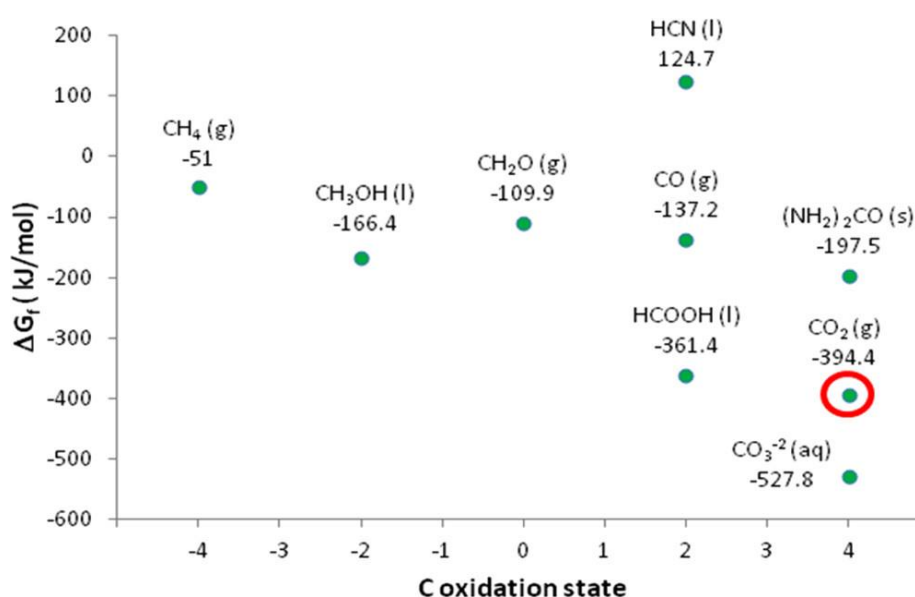
Figure 1.3: Gibbs free energy of CO_2 and formation of C_1 components (Aresta et al., 2014)

As result, three main technical challenges arise to overcome CO_2 stability including the considerable need for *energy input* which must be from carbon-neutral sources to prevent further CO_2 emissions, *active catalysts* and *high operating temperatures and/or pressures* to decrease the activation energy of CO_2 conversion processes (Styring and Armstrong, 2011; Alper and Orhan, 2017). Despite these technical challenges, its potential for achieving CO_2

emission reduction targets while at the same time converting waste CO_2 into a wide range of chemicals, fuels and materials is a powerful driving force for CO_2 utilisation.

1.1.3. Overview of CO₂ transformation technologies

Figure 1.4 illustrates nine CO_2 transformation technologies grouped into two biological and seven chemical conversion processes.
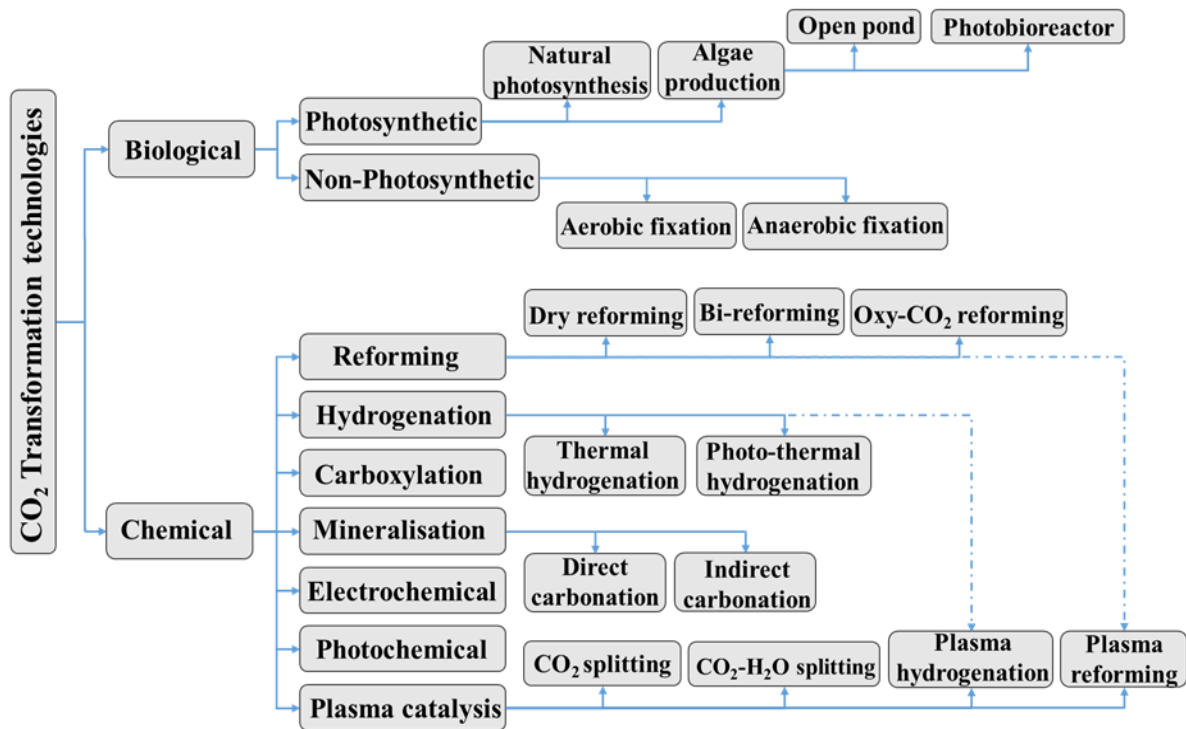
Figure 1.4: Biological and chemical CO_2 transformation technologies

1.1.3.1. Photosynthetic CO₂ fixation

Photosynthetic CO_2 fixation includes *natural photosynthesis* in which green plants absorb energy from sunlight for CO_2 and water reduction into energy-rich components such as glucose (Janssen et al., 2014), and *algae production* using inorganic nutrients, water, light and CO_2 as carbon source (Slade and Bauen, 2013). Natural photosynthesis is a normal process for maintaining life on Earth thus, it is not taken into consideration. Two significant systems are available for algae production including *photobioreactors* (Figure 1.5a) wherein algae are cultivated in enclosed and transparent array of tubes and *open or raceway pond* (Figure 1.5b) for algae cultivation in the open air (Williams and Laurens, 2010; Slade and Bauen, 2013).

Figure 1.5: Algae cultivation in (a) photobioreactors and (b) open ponds (Williams and Laurens, 2010)

1.1.3.2. Non-photosynthetic CO_2 fixation

Non-photosynthetic CO_2 fixation refers to as CO_2 conversion into value-added bio-products using microorganisms (for example, acetogens and methanogens) and a source of high-energy electrons (including electricity and chemicals). This method can be performed under aerobic or anaerobic conditions. During *aerobic CO_2 fixation*, microorganisms access oxygen from the surrounding environment whereas, in *anaerobic CO_2 fixation*, there is no oxygen entering the reaction medium (Hawkins et al., 2013; Lovley and Nevin, 2013).

1.1.3.3. Reforming

Reforming is an endothermic process in which natural gas is heated at very high temperatures (typically around $600 - 900℃$) in the presence of metal-based catalysts to produce a synthetic gas (usually called syngas) primarily composed of CO, H_2 and some amounts of H_2O and CO_2. This process is commonly referred to as methane reforming since natural gas is mainly composed of methane (CH_4). Three methods of methane reforming can be distinguished in the CO_2 utilisation context, *dry reforming*, *bi-reforming* and *oxy-CO_2 reforming*. The main difference between the three methods is based on the oxidant used. *Dry reforming* (Reaction 1.1) does not require any oxidant whereas, *bi* and *oxy-CO_2 reforming* processes respectively need water (Reaction 1.2) and oxygen (Reaction 1.3) as oxidants (Kathiraser et al., 2015; Abdullah et al., 2017).

$$CH_4 + CO_2 \rightarrow 2CO + 2H_2 \quad\quad (1.1)$$

$$3CH_4 + 2H_2O + CO_2 \rightarrow 4CO + 8H_2 \quad\quad (1.2)$$

$$3CH_4 + CO_2 + O_2 \rightarrow 4CO + 6H_2 \quad\quad (1.3)$$

5
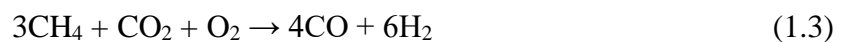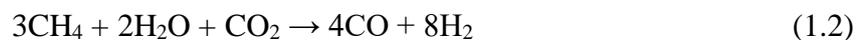
1.1.3.4. Hydrogenation

CO_2 hydrogenation process is simply the addition of H_2 to CO_2. H_2 compound has a much higher Gibbs free energy ($\Delta G° = 0$ kJ/mol) than CO_2 molecule therefore, CO_2 reduction through hydrogenation is more favourable thermodynamically. CO_2 hydrogenation is one of the most promising processes of CO_2 conversion because it leads to a wide range of chemicals and fuels such as formic acid, methane, methanol, higher alcohols, light olefins and liquid hydrocarbons (Ye et al., 2019; Saeidi et al., 2021). However, the source of hydrogen represents one of the main challenges for CO_2 hydrogenation since it must be produced using renewable sources to avoid further CO_2 emissions (Li et al., 2018).

There are three methods for the CO_2 hydrogenation process depending on the type of energy used. This includes *thermal*, *photothermal* and *plasma CO_2 hydrogenation* wherein heat, the combination of light and heat and plasma are used during the hydrogenation process respectively. The use of plasma or the combination of light and heat has the advantage of decreasing the high operating temperatures during thermal CO_2 hydrogenation (Jantarang et al., 2018; Wang et al., 2018). CO_2 hydrogenation usually leads to C_1 compounds such as methanol, methane, CO and formic acid (Wang et al., 2018; Ye et al., 2019). The synthesis of C_{2+} products (for instance, liquid hydrocarbons, C_2-C_4 olefins and higher oxygenated compounds) is more challenging owing to CO_2 thermodynamic stability. Hence, CO_2 hydrogenation to C_{2+} products is usually carried out via indirect routes using intermediates such as methanol and syngas (Li et al., 2018; Ye et al., 2019).

1.1.3.5. Carboxylation

The carboxylation process consists of attaching a functional CO_2 molecule to another chemical compound to synthesise polymers (also known as polymerization), ureas (RRNCONRR), carbamates ($R_1R_2NCOOR_3$) and organic carbonates (ROC(O)OR). CO_2 can also be used as a carboxylative agent for the direct HC carboxylation process wherein CO_2 is inserted into the C–H bond of alkanes, aromatics and olefins to produce carboxylic acids such as acetic, toluic and acrylic acids (Cuéllar-Franca and Azapagic, 2015; Alper and Orhan, 2017).

Although the aforementioned reactions are thermodynamically feasible, not all of them have been successfully achieved. Especially the acrylic acid as to date, no experimental studies have reported the direct synthesis of acrylic acid from CO_2 and ethylene, only the production of esters and sodium salts has been achieved (Wang et al., 2017).

1.1.3.6. Mineralisation

Also called carbonation, CO_2 mineralisation is defined as CO_2 reaction with chemical components containing alkaline earth oxides (for example magnesium and calcium oxides) for the synthesis of corresponding inorganic carbonates (such as magnesium and calcium carbonates). Thermodynamically, the CO_2 molecule has a higher Gibbs free energy than inorganic carbonates. Hence, CO_2 mineralisation process can theoretically release energy as described by Reaction (1.4) in which Me represents alkaline and alkali-earth metals including, Ca, Mg and Na (Azdarpour et al., 2015; Alper and Orhan, 2017).

$$CO_2 + MeO \rightarrow MeCO_3 + Heat \tag{1.4}$$

Two methods are available for CO_2 mineralisation including *direct* and *indirect carbonation.* During *indirect carbonation*, there is first extraction of alkaline and alkali-earth metals from natural minerals (such as serpentine and olivine) followed by carbonate precipitation in different reactors (Olajire, 2013).
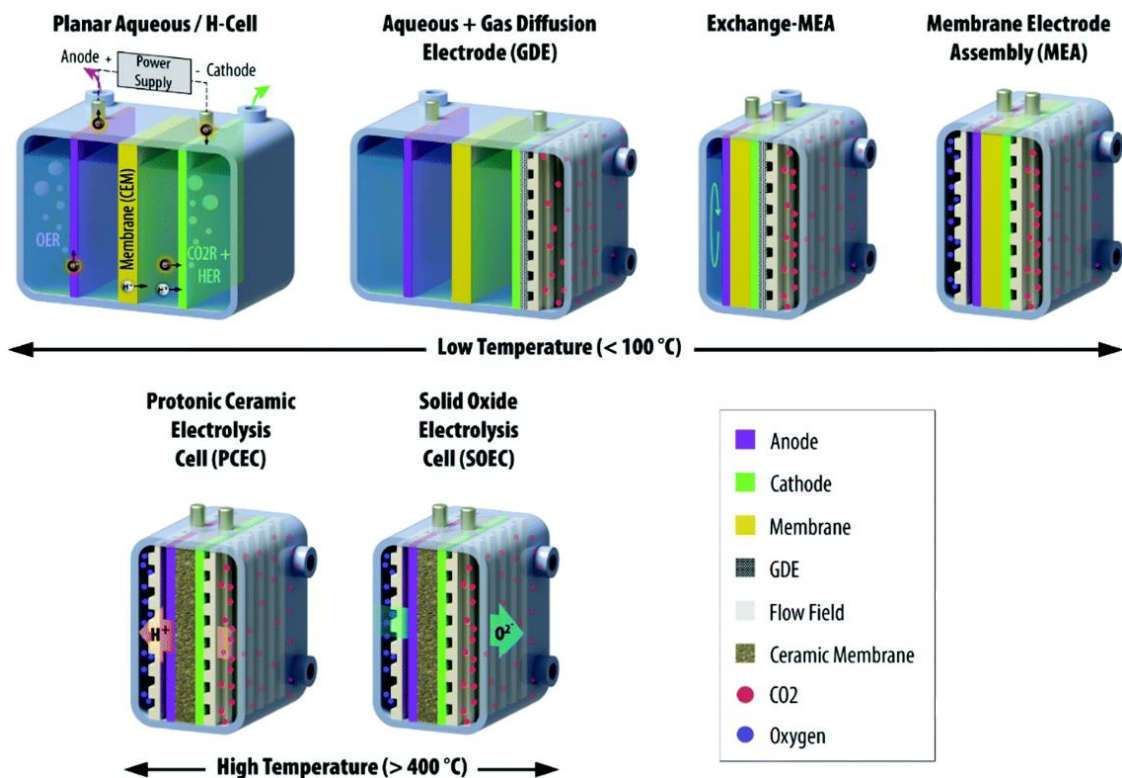
Figure 1.6: Overview of low and high-temperature electrolysers (Grim et al., 2020)

1.1.3.7. Electrochemical reduction

CO_2 electrochemical reduction refers to as CO_2 conversion to fuels and chemicals in an electrolyser using an electrical energy input. Electrolysers are commonly grouped based on their operating temperatures. This includes low (below 100℃) and high temperatures (above

7

400℃) as illustrated in Figure 1.6 (Grim et al., 2020). High-temperature electrolyser is further discussed in Section 1.1.4.

A typical low-temperature electrolyser consists of three main components including the negative electrode (or cathode), electrolyte and positive electrode (or anode). CO_2 electrochemical reduction occurs on the cathode side to produce value-added products whereas, H_2O oxidation takes place at the anode for the synthesis of electrons/protons (e-/H+) and oxygen (Malik et al., 2017). CO_2 electrochemical reduction is also a promising CO_2 transformation technology as it leads to a wide range of products including CO, methanol, methane, ethylene, formic acid, and formaldehyde. Furthermore, some electrolysers such as membrane electrode assembly (MEA) can operate under ambient conditions (Jarvis and Samsatli, 2018; Grim et al., 2020)..

1.1.3.8. Photochemical reduction

CO_2 photochemical reduction is an artificial photosynthesis process that aims to mimic how green plants synthesise glucose from water and CO_2 by using photocatalysts for CO_2 reduction into value-added products (Mikkelsen et al., 2010). It is paramount to distinguish between photochemical reduction and photosynthetic methods. Though both processes require light as an energy source, the latter uses microorganisms for CO_2 fixation (Janssen et al., 2014).
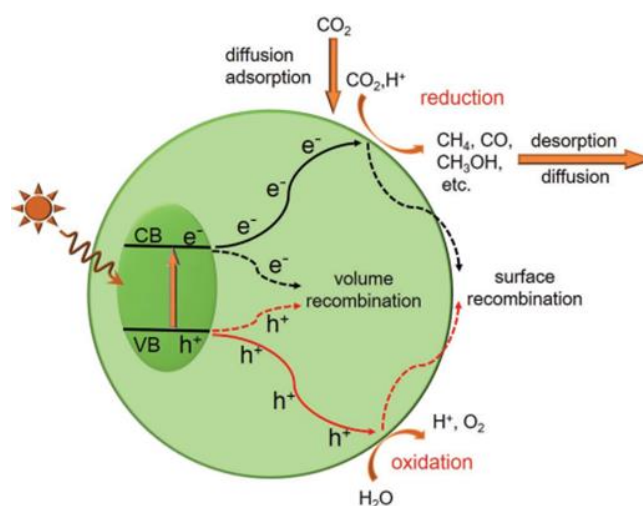
Figure 1.7: Schematic of CO_2 photochemical reduction steps (Wu et al., 2017)

As shown in Figure 1.7, CO_2 photochemical reduction consists of five steps including (1) Adsorption of light or photons to produce holes (h+) and electrons (e-), (2) separation of produced holes and electrons, (3) CO_2 adsorption on the photocatalyst surface, (4) photoreduction of CO_2 and H_2O oxidation, and (5) desorption of the formed products from the photocatalyst (Wu et al., 2017).

1.1.3.9. Plasma catalysis

Different types of energy including, light (such as laser and UV light), heat (e.g. electrically heated furnaces), and electrical discharges (for instance, plasma jet and microwave discharge), can be used to sufficiently heat a gaseous substance until its electrons are stripped from their respective atoms. This creates a set of free ions and electrons called ionized gas. The created ionized gas exists in the fourth state of matter known as plasma. Substances in plasma form are neutral overall since there are an equal amount of opposite charges. Moreover, they can conduct electricity due to the presence of free electrons.

Non-thermal plasma (NTP) consists of activating the ionized gas to produce highly energetic electrons (with energy between 1 and 10 eV) which can activate highly stable compounds such as CO_2. However, very low selectivity to desired products was reported using NTP alone. As a result, there has been an increasing interest to combine NTP with heterogeneous catalysts. This technique refers to as plasma catalysis (Snoeckx and Bogaerts, 2017; Grim et al., 2020).

Plasma catalysis is usually performed in either one-stage or two-stage configuration as portrayed in Figure 1.8. The combination of plasma and catalyst has shown better adsorption of gas molecules on the catalyst surface, higher process efficiency and lower operating temperatures (Tu et al., 2013; Bogaerts et al., 2018). Plasma catalysis is typically carried out with pure CO_2 (*CO_2 splitting*) or using CO_2 in reaction with H_2-containing components, for instance, H_2O (*CO_2-H_2O splitting*), CH_4 (*plasma reforming*) and H_2 (*plasma hydrogenation*) (Snoeckx and Bogaerts, 2017).

(a): One-stage configuration

(b): Two-stage configuration
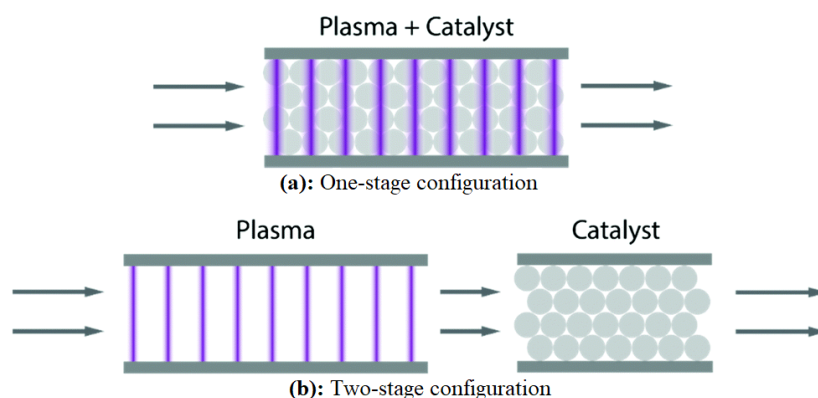
Figure 1.8: Schematic of stage configurations for plasma catalysis (Snoeckx et al., 2017)

1.1.4. Process description of synthetic fuel production from CO_2

1.1.4.1. Solid oxide electrolysis cells

Solid oxide electrolysis cells (SOECs) are electrocatalytic cells that use renewable electricity for H_2 or CO synthesis from H_2O or CO_2 electrolysis respectively. SOECs usually operate at

high temperatures (above 700°C) which decrease the electrical requirement during electrolysis. In comparison to other electrolysers, SOECs have the unique ability to co-electrolyse CO_2 and H_2O for syngas production (Graves et al., 2011; Stempien et al., 2014).

With regards to geometry, SOECs are either tubular or planar. Although better degradation rates (such as higher thermal and mechanical stabilities) are observed with tubular SOECs, planar SOEC structures are widely preferred owing to their higher production rates, ease to manufacture and shorter current collection paths (Hansen, 2015; Yun Zheng et al., 2017). Regarding the scale, single cells (Figure 1.9a) with uniform sizes are arranged to form a SOEC stack (Figure 1.9b). Then, SOEC modules are made by assembling several stacks. Modular SOEC design allows for scale-up of SOECs resulting in higher surface area and production capacity (Yun Zheng et al., 2017).
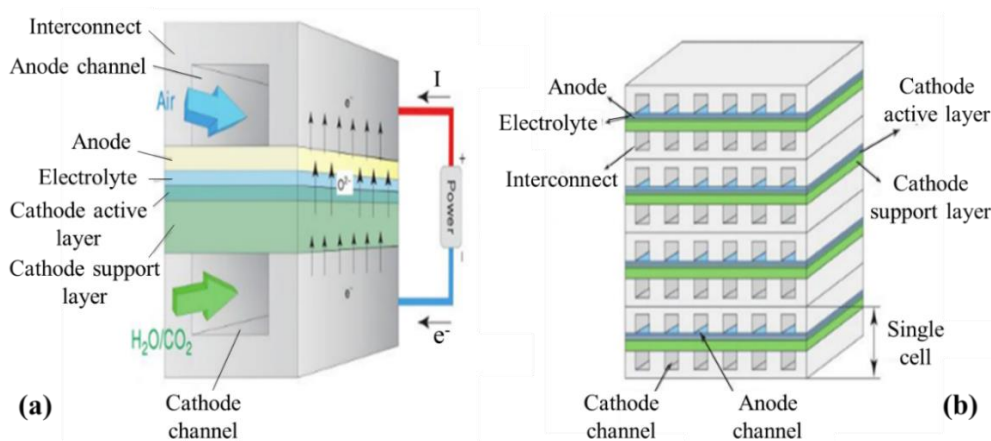
Figure 1.9: Schematic of (a) single cell and (b) stack of planar SOEC (Boehm et al., 2015)

Every single cell has three main components including a cathode or fuel electrode, a dense electrolyte (ion-conducting membrane) and an anode or oxygen electrode. During syngas synthesis, H_2O and CO_2 are co-electrolysis occur on the cathode side as described by Reactions 1.5 and 1.6 respectively. Both electrolysis reactions also produce O^{2-} ions which flow through the dense electrolyte to the anode electrode wherein they re-combine to generate electrons and oxygen as shown in Reaction (1.7) (Boehm et al., 2015; Yun Zheng et al., 2017).

$$H_2O + 2e^- \rightarrow H_2 + O^{2-} \tag{1.5}$$

$$CO_2 + 2e^- \rightarrow CO + O^{2-} \tag{1.6}$$

$$2O^{2-} \rightarrow O_2 + 2e^- \tag{1.7}$$

1.1.4.2. Fischer-Tropsch synthesis process

The Fischer-Tropsch synthesis (FTS) process is defined as a polymerization process in which hydrocarbon chains are synthesised from a carbon source via CO hydrogenation. Possible FTS reactions are described by Reactions (1.8) to (1.10) for alkanes (C_nH_{2n+2}), olefins (C_nH_{2n}) and alcohols ($C_nH_{2n+1}OH$) production from syngas respectively (Saeidi et al., 2015). The synthesis of long-chain HCs (C_{2+}) from CO_2 can be performed in one or multiple reactors. The latter aims to first convert CO_2 into syngas followed by FTS reactions in different reactors. The direct one-reactor method, also called modified CO_2-FTS process, combines CO_2 reduction to syngas through the reverse water gas shift (RWGS) Reaction (1.11) and CO hydrogenation to HCs via FTS in a single reactor (Li et al., 2018; Ye et al., 2019).

$$nCO + (2n+1)H_2 \;\rightarrow\; C_nH_{2n+2} + nH_2O \tag{1.8}$$

$$nCO + 2nH_2 \rightarrow C_nH_{2n} + nH_2O \tag{1.9}$$

$$nCO + (2n - 1)\,H_2 \rightarrow C_nH_{2n+1}OH + (n - 1)\,H_2O \tag{1.10}$$

$$CO_2 + H_2 \rightleftharpoons CO + H_2O \tag{1.11}$$
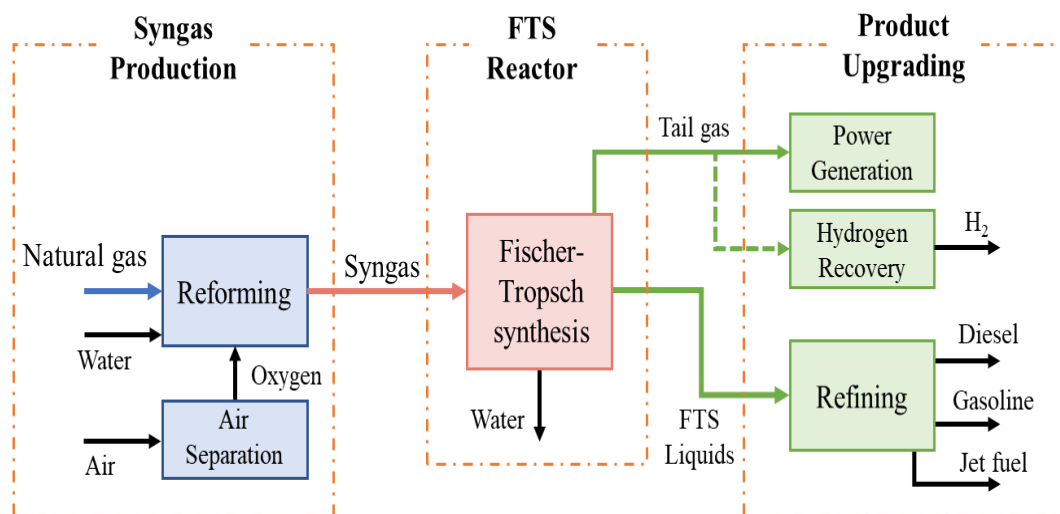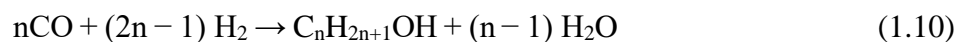
Figure 1.10: Block flow diagram of a typical FTS plant. Adapted from GSTC (2022)

Figure 1.10 depicts a simplified diagram of a typical FTS plant using natural gas as feedstock. The FTS plant has three main sections including syngas production, FTS reactor and product upgrading. The syncrude obtained from FTS reactions is separated into water, liquid condensate and tail gas. The liquid condensate is sent to the upgrading section for the synthesis of diesel, gasoline and/or jet fuel. The tail gas contains gaseous HCs and unconverted reactants. it can also be upgraded for H_2 recovery and/or power generation (de Klerk, 2011; Selvatico et al., 2016).

FTS reactions are highly exothermic and depending on the product composition, the enthalpy change per mole of converted CO is roughly 165–180 kJ/mol. Insufficient cooling systems will lead to higher catalyst deactivation and lower product selectivity. Therefore, all FTS reactors are designed to maximize heat removal (Saeidi et al., 2014). FTS reactors are divided into conventional reactors (fixed-bed, slurry bubble column and fluidized-bed reactors) and intensified reactors (monolithic, membrane and microchannel reactors). Table 1.1 details the advantages and limitations of each FTS reactor.

Table 1.1: Advantages and limitations of conventional and intensified FTS reactors (Saeidi et al., 2015, 2021; Martinelli et al., 2020)

Reactor	Advantages	Limitations
Conventional reactors		
Fixed-bed (FBR)	• Low maintenance cost • Easy to test at lab-scale using single tube • No need for a section to separate catalyst • Reduced losses due to wear and attrition	• Poor heat management • High mass transfer resistance • High capital costs • High pressure drop
Slurry bubble column (SBCR)	• Simplicity of operation • Lower capital costs than FBR • Low pressure drop • Can operate at higher temperature • Longer reactor run owing to online addition or removal of catalyst	• Difficult to scale-up • Deactivation of catalysts due to attrition • Require large reactors • Need careful design to avoid plugging
Fixed fluidized-bed (FFB) and circulating fluidized-bed (CFB)	• Higher fraction of gaseous HCs • Better heat exchange efficiency than FBR • Higher temperature control due to rapid circulation • No downtime for catalyst change • FFBs have higher capacity and lower capital and maintenance costs	• Require high temperatures to achieve acceptable productivity • CFBs require energy to circulate the catalyst • Carbon deposition owing to high operating temperatures • High linear velocities lead to erosion problems
Intensified reactors		
	• Simple reactor construction • Low pressure drop	• Large external recycle of liquid products is required • High capital costs

Monolithic (MLR)	• No need for product and catalyst separation • High gas and liquid mass transfer • No catalyst attrition	
Membrane (MR)	• In-situ water removal through the membrane layer • Negligible heat and mass transfer resistances • Reduced formation of by-products • High reaction rates	• Low productivity per unit of total reactor volumes • High costs of membrane modules • Concerns with heat removal
Microchannel (MCR)	Compared to conventional reactors: • Much smaller in size and more mobile • Higher catalytic activity • Better heat and mass transfer • High surface area-to-volume ratio • Optimum temperature control	• Concerns with the replacement of deactivated catalyst • Require accurate reactor and catalyst designs • High reactor cost due to manufacturing complexity

1.2. Motivation for this research

Within the current global industry, energy represents one of the most important requirements for daily life and activities including transportation, electricity, heating and cooling (Overland, 2016). Looking specifically at transportation fuels (for instance, jet fuel, gasoline and diesel), the demand is absolutely gigantic and was estimated at 54.5 million bbl/day in 2020. This is particularly true for gasoline fuel whose demand is forecast to reach 27.7 million bbl/day in 2030 (Sönnichsen, 2022).

With fossil fuels (especially crude oil) being the primary source for transport fuel synthesis, they account for 36% of CO_2 emissions worldwide which is predicted to increase by 22% before 2040 (OPEC, 2017). A transition to CO_2-free forms of energy thus, stopping using fossil fuels altogether seems desirable for a simplistic solution. However, this transition would profoundly disrupt the current economy owing to the limited capacity of electric vehicles and the intermittency of renewable energies such as wind and solar power (de Vasconcelos and Lavoie, 2019; Fernández-Torres et al., 2022).

Since decarbonizing the world transport industry which relies on fossil fuels could take several decades, it would be reasonable to undertake in parallel the synthesis of carbon-neutral fuels

that will reduce fossil CO_2 emissions into the atmosphere. In this context, Power-to-fuels (or more generally Power-to-X) concept arises as a potential solution to store intermittent renewable electricity for the production of synthetic fuels (de Vasconcelos and Lavoie, 2019). H_2 production through water electrolysis represents the most well-known Power-to-fuels technology (Wang et al., 2019). Furthermore, CO_2 is one of the most suitable carbon-based feedstock for Power-to-fuels technologies as it allows a closed CO_2-fuels-CO_2 cycle hence, CO_2-neutral fuels overall (Rosa, 2017; Vázquez et al., 2018; de Vasconcelos and Lavoie, 2019).

Considering both Power-to-fuels and CO_2 transformation technologies, hydrogenation and electrochemical reduction (particularly FTS and SOEC) are the most suitable processes to produce synthetic fuels from CO_2 and water using renewable energy. Moreover, gasoline is one of the most promising liquid fuels obtained from CO_2 either directly via the CO_2-FTS process or indirectly through the FTS process using syngas from SOEC as intermediate. Besides accounting for 59% of transport fuel consumption, gasoline fuel is also used in emergency electricity generators and to power equipment in farming and construction sectors (Mikayilov et al., 2020). Though renewable energies are beyond the scope of this research, their development are critical to provide the climate benefits of CO_2-neutral gasoline. To illustrate, a plant would consume roughly 453 MW to produce 4,500 bbl/day of gasoline via CO_2 hydrogenation (Fernández-Torres et al., 2022) leading to a total energy requirement of 2,788.5 GW to satisfy the world demand in gasoline fuel.

Therefore, it is paramount to assess the prospects of commercial deployment of carbon-neutral gasoline from atmospheric CO_2. Experiment-based studies are essential for understanding catalyst performance and reaction mechanisms. However, for commercial applications, further insights into interaction among operation units (such as compressors, heaters and reactors) and how they affect the overall system performance are highly needed. In this regard, modelling approaches and simulation software are indispensable techniques for process design and optimisation allowing process transition from laboratory to commercial scale.

1.3. Aim and objectives of this research

The aim of this research was to investigate the technical performance of synthetic fuel production from CO_2 using modelling and simulation approaches. More specifically, the research aimed to use Aspen Plus software to assess the performance of gasoline fuel synthesis

from CO_2 through direct CO_2-FTS and integrated SOEC-FTS processes with the sole purpose of improving CO_2-to-gasoline processes. To achieve the research aim, the following objectives were fulfilled:

- To provide a comprehensive review of experimental and modelling/simulation studies for syngas synthesis using SOEC and liquid fuel production via FTS and CO_2-FTS processes.

- To develop and validate a pseudo-dynamic model of planar SOEC for CO_2/H_2O co-electrolysis to syngas.

- To perform a long-term performance analysis of syngas production using SOEC and considering component structural degradation.

- To carry out modelling, simulation and validation of direct CO_2-FTS process to gasoline fuel.

- To perform a performance analysis of the CO_2-FTS process to gasoline considering ex-situ water removal techniques for the improvement of process performance.

- To perform process simulation and performance analysis of integrated SOEC-FTS to gasoline fuel.

- To carry out a comparative analysis between direct CO_2-FTS and integrated SOEC-FTS processes for gasoline fuel synthesis.

1.4. Novel contributions

Extensive modelling and simulation studies have been reported on SOEC systems for syngas production. However, most of these studies focused only on SOEC performance and did not consider SOEC degradation (Hawkes et al., 2006; O'Brien et al., 2009; Fu et al., 2010; Ni, 2012a, 2012b; Stempien et al., 2013b; Menon et al., 2015; Luo et al., 2015; Yi Zheng et al., 2017; Banerjee et al., 2018). A few models were proposed to clarify degradation mechanisms within SOEC systems (Virkar, 2010; Chatzichristodoulou et al., 2016; Nerat and Juričić, 2018; Navasa et al., 2018; C. Wang et al., 2020).

However, these models were developed for SOEC during water electrolysis. Furthermore, modelling studies on SOEC degradation carried out steady-state model validation in terms of voltage versus current density. Since SOEC degradation assesses the evolution of operating

voltage with time for a specific current density (Sohal et al., 2012), appropriate parameter validation is essential for the establishment of the SOEC degradation model.

Similarly, several studies have demonstrated the potential of liquid fuel synthesis via the FTS process using syngas (Guettel and Turek, 2009; Qian et al., 2012; Hooshyar et al., 2012; Ermolaev et al., 2015; Moazami et al., 2015; Selvatico et al., 2016; Seyednejadian et al., 2018; Chandra et al., 2021). Nevertheless, most of these studies assumed syngas production from non-renewable feedstock (such as natural gas and coal) leading to serious concerns regarding CO_2 emissions. Although some studies looked into integrated SOEC-FTS for a more sustainable process of liquid fuel synthesis (Becker et al., 2012; Stempien et al., 2015; Cinti, Baldinelli, et al., 2016; Samavati et al., 2018; Herz et al., 2018; Wang et al., 2019; Marchese et al., 2020), modelling studies on direct CO_2-FTS process remain scarce. This is potentially due to the low yield of liquid fuels (below 29%) observed during experimental studies arising from low CO_2 conversion.

To the best of my knowledge, two modelling studies are available in the open literature for CO_2-FTS process improvement via in-situ (Najari et al., 2019) and ex-situ (Meiri et al., 2017) water removal. However, Najari et al. (2019) focused on the CO_2-FTS process to gaseous hydrocarbons (C_1 to C_4). Though Meiri et al. (2017) investigated the CO_2-FTS process to liquid hydrocarbons and achieved up to 51% C_{5+} yield with 85% CO_2 conversion, their kinetic model was based on experimental data with very high selectivity towards gaseous hydrocarbons (between 45 to 78%). Therefore, the reported results could be highly inaccurate.

Taking these findings into consideration, the novel contributions of this research are as follows:

- A critical review of the different CO_2 transformation technologies (both experimental and modelling/simulation studies) and a comparative analysis of research trends and projects worldwide at laboratory, pilot, demonstration and commercial scale.

- A pseudo-dynamic model of planar SOEC operating in CO_2/H_2O co-electrolysis mode and incorporating the structural degradation of SOEC components materials.

- A novel design at a microstructure level of typical SOEC component materials: Ni-YSZ/YSZ/LSM-YSZ with a degradation rate of 0.89 %/1000hrs after 20,000 hours of operation.

- A steady-state model of the CO_2-FTS process based on first principles and a modified ASF distribution theory to predict gasoline range hydrocarbons (C_5 to C_{11}).

- Process configuration and performance analysis and comparison of CO_2-FTS process to gasoline fuel with ex-situ water removal through multiple reactors in series and single reactor with recycle.

- Process simulation of integrated SOEC-FTS to gasoline and comparative analysis between direct CO_2-FTS and SOEC-FTS processes to gasoline fuel.

1.5. Scope of this study

This research essentially focused on CO_2 conversion into synthetic fuels. The scope of this study is limited to first principles modelling, simulation and analysis of SOEC, FTS and CO_2-FTS processes for CO_2 conversion into syngas and gasoline fuel (red dashed lines in Figure 1.11). The study carried out model validation of each process at laboratory-scale using available data from the literature. As illustrated in Figure 1.11, SOEC for syngas production is mostly discussed in Chapters 3 and 4 whereas, CO_2-FTS process for gasoline fuel synthesis is elaborated in Chapter 5. The overlap shown by Chapter 6 represents the comparative analysis performed between direct CO_2-FTS and integrated SOEC-FTS processes.
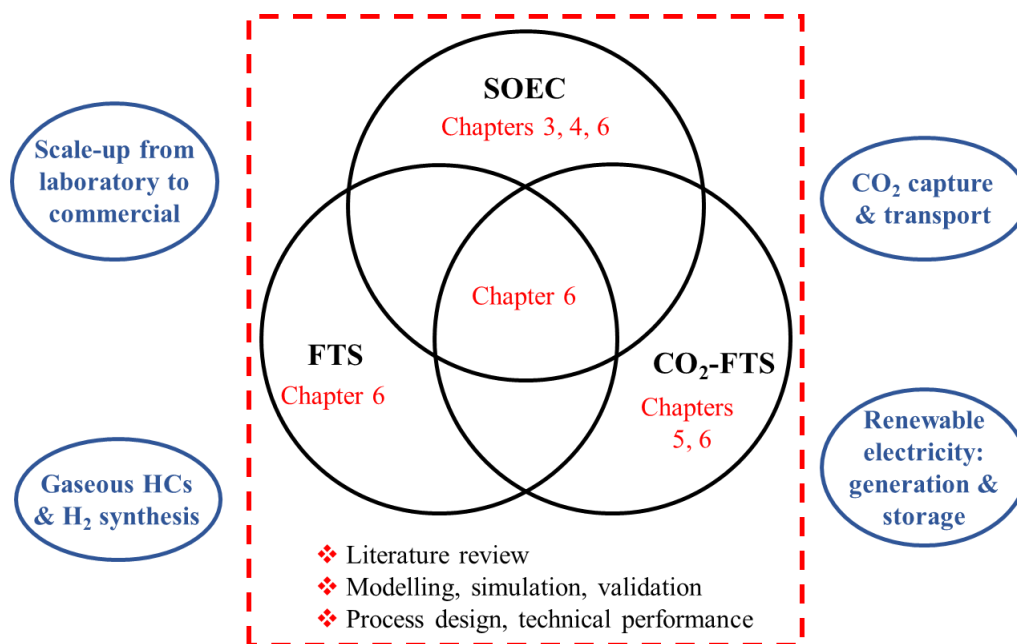
Figure 1.11: Overview on the scope of this study

It is important to specify that the following are beyond the scope of this research:

- CO_2 capture and transportation to the plants
- Generation and storage of renewable electricity as well as plant connectivity to the grid
- Gaseous hydrocarbons and hydrogen production

- Scale-up from laboratory to commercial-scale

Although model validation was performed at laboratory-scale in this research, performance analysis and comparison were carried out at commercial-scale to assess the prospects of industrial-scale CO_2-to-gasoline processes. Therefore, successful scale-up of catalysts and operation units was assumed. However, it was ensured in this research that results obtained at large-scale reflect the design and operational guidelines of CO_2 process plants at commercial-scale.

1.6. Research methodology and tools used for this study

1.6.1. Research methodology

CO_2 conversion to gasoline fuel via direct CO_2-FTS process or integrated SOEC-FTS process using syngas as intermediate is yet to be commercial. The processes are still facing some technical challenges hindering their commercial deployment, especially the degradation issue of SOEC component materials and the low yield of liquid fuels from the direct CO_2-FTS process. Figure 1.12 shows the research methodology followed to achieve the research objectives. Since SOEC and FTS models are validated in their corresponding sections (blue and green lines respectively), model validation of SOEC-FTS was not performed.
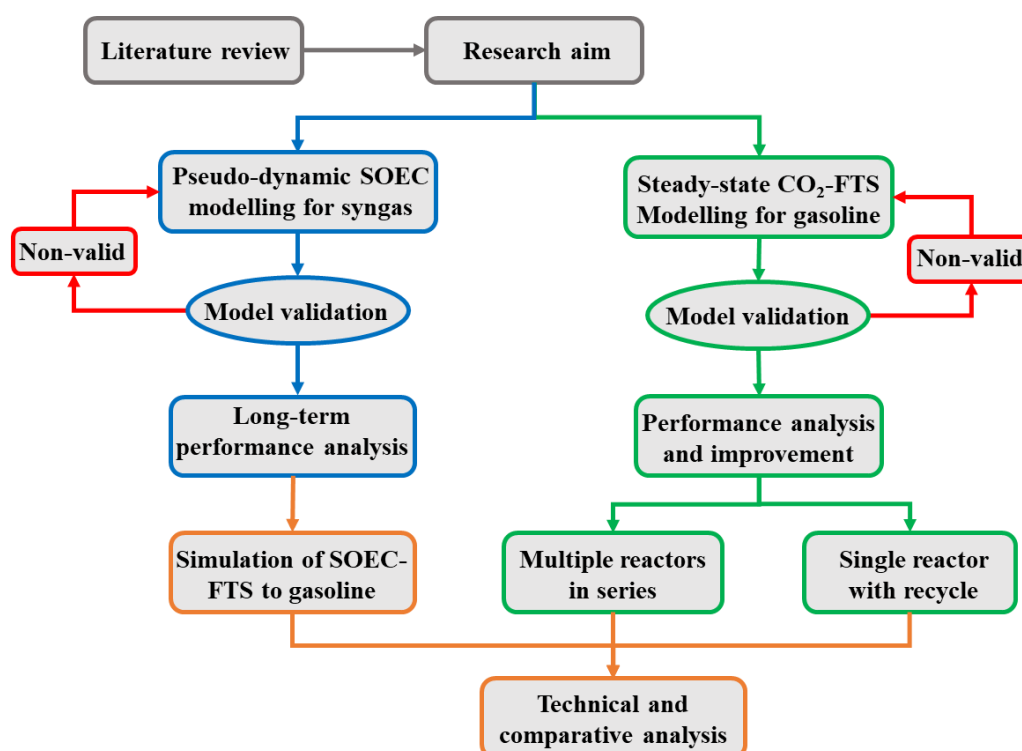
Figure 1.12: Overview of the research methodology

1.6.2. Software tool used in this research

Aspen Plus® stands for **A**dvanced **S**ystem for **P**rocess **EN**gineering and was developed by Aspen Technology Inc. It is an engineering software based on flowsheet simulation and is widely used in several industries such as power, refining, chemical and pharmaceutical. Furthermore, Aspen Plus® software includes Fortran® routines for model implementation and physical properties for chemicals, polymers, electrolytes and solids to carry out process design and optimisation as well as to assess the performance, energy requirement, cost and operational issues of a process plant (Al-Malah, 2016; AspenTech, 2022). As a result, Aspen Plus® software was deemed adequate for process simulation, model implementation and performance analysis in this study.

1.7. Outline of the thesis

Chapter 2 presents a critical review of previous studies on CO_2/H_2O co-electrolysis using SOEC and liquid fuel synthesis through FTS and CO_2-FTS processes. Both experiment (at laboratory, pilot, demonstration and commercial-scale) and modelling/simulation (including optimisation and TEA) based studies are considered.

Chapter 3 details the model development, simulation and validation of planar SOEC for CO_2/H_2O co-electrolysis and integrating structural degradation of SOEC component materials. Model validation was performed for both SOEC performance (syngas outlet composition) and degradation (operating voltage with time).

Chapter 4 elaborates SOEC long-term performance analysis. The effects of SOEC operating conditions (current density, temperature, feed gas composition and flowrate) and component structural damages on syngas production efficiency and degradation rate are examined. Material design of SOEC components is also investigated for long-term performance improvement.

Chapter 5 discusses the model development, simulation and validation of the CO_2-FTS process for gasoline fuel synthesis. Two process configurations (multiple reactors in series and single reactor with recycle) for ex-situ water removal are considered and their performances are analysed and compared in terms of CO_2 conversion, gasoline yield, energy requirement and process efficiency.

Chapter 6 focuses on the process simulation of integrated SOEC-FTS to gasoline fuel. It also details the performance analysis of open-loop and recycle SOEC-FTS systems. Finally, a comparative analysis of the performance of direct CO_2-FTS and SOEC-FTS processes to gasoline fuel is provided.

Chapter 7 concludes this study and elaborates recommendations for future work.

2. Literature review[2]

This chapter aims to critically review the recent research activities on SOEC for syngas production, FTS and direct CO_2-FTS processes for liquid fuel synthesis. Sections 2.1, 2.2 and 2.3 focus on experiment-based studies of SOEC, FTS and direct CO_2-FTS processes, respectively. For each process, existing experimental rigs and relevant studies are reviewed at lab, pilot and commercial-scale. Sections 2.4, 2.5 and 2.6 review the recent modelling and simulation-based studies of SOEC, FTS and direct CO_2-FTS processes, respectively. In each section, developed models as well as optimisation, technical and economic analysis (TEA) studies are reviewed. Key findings of the literature review and research gaps are summarised in Section 2.7.

2.1. Rigs for SOEC and experimental studies

2.1.1. Lab rigs of SOEC for CO_2/H_2O co-electrolysis and relevant experimental studies

2.1.1.1. SOEC Rigs for CO_2/H_2O co-electrolysis at lab scale

As mentioned in Section 1.1.4, SOEC structures can be either tubular or planar. However, given the volumetric and current collection advantages of planar designs, they are widely preferred (Yun Zheng et al., 2017). Table 2.1 summarises existing planar SOEC rigs that have been developed and tested for syngas production at a laboratory-scale. SOEC rigs are presented in ascending order of cell numbers. The number of cells of SOEC stack varies from 1 to 10 with a specific AC power below 1.0 kW. The cell configuration of electrode materials is cathode/electrolyte/anode.

An assembly of SOEC stack testing from DTU Energy Conversion is shown in Figure 2.1. The stack was designed by Topsøe Fuel Cells A/S (TOFC) for both water electrolysis and CO_2/H_2O co-electrolysis. The SOEC stack contains two repeating cells separated by interconnect plates with glass sealing underneath. Besides SOEC components, other balance-of-plant (BOP) equipment are also required to effectively operate a SOEC system. BOP components differ based on SOEC operating conditions and the size of the stack system.

---

[2] Most of this Chapter has been published in Kamkeng, A. D. N., Wang, M., Hu, J. et al. (2021) Transformation technologies for CO_2 utilisation: Current status, challenges and future prospects. Chemical Engineering Journal, 409, 128138

Table 2.1: Summary of SOEC Rigs for CO_2/H_2O co-electrolysis at laboratory-scale

Company	Location	Electrode materials	Number of cells	Operating T and applied j	Active cell area (cm^2)	AC power (kW)	Reference
Xi'an Polytechnic University	China	Ni-YSZ/YSZ/LSM-YSZ	1	800°C and 0.4 A/cm^2	63.0	N/S	(Li et al., 2019)
DTU Energy Conversion	Denmark	Ni-YSZ/YSZ/LSM-YSZ	2	800°C and 0.5 A/cm^2	16.0	N/S	(Sun et al., 2013)
FuelCell Lab	Italy	Ni-YSZ/YSZ/LSM-YSZ	4	750°C and 0.5 A/cm^2	80.0	0.20	(Cinti et al., 2016)
EPFL	Switzerland	Ni-YSZ/YSZ/LSC-CGO	6	750 – 850°C and 0.5 A/cm^2	50.0	0.70	(Diethelm et al., 2013)
Technical Research Centre of Finland	Finland	Ni-YSZ/YSZ/LSCF and LSC	6	700 – 800°C and 0.65 A/cm^2	80.0	0.85	(Kotisaari et al., 2017)
DTU Energy Conversion	Denmark	Ni-YSZ/YSZ/LSCF-CGO	8	700 – 800°C and 0.5 A/cm^2	87.7	0.62	(Agersted et al., 2016)
		Ni-YSZ/YSZ/LSM-YSZ	10	850°C and 0.75 A/cm^2	92.2	N/S	(Ebbesen et al., 2011)
Idaho National Laboratory (INL)	USA	Ni-YSZ/YSZ/LSM-YSZ	10	800 – 830°C and 0.5 A/cm^2	64	N/S	(Stoots et al., 2009)
CEA-LITEN	France	Ni-YSZ/YSZ/LSC-CGO	10	800°C and 0.8 A/cm^2	100	0.92	(Reytier et al., 2015)
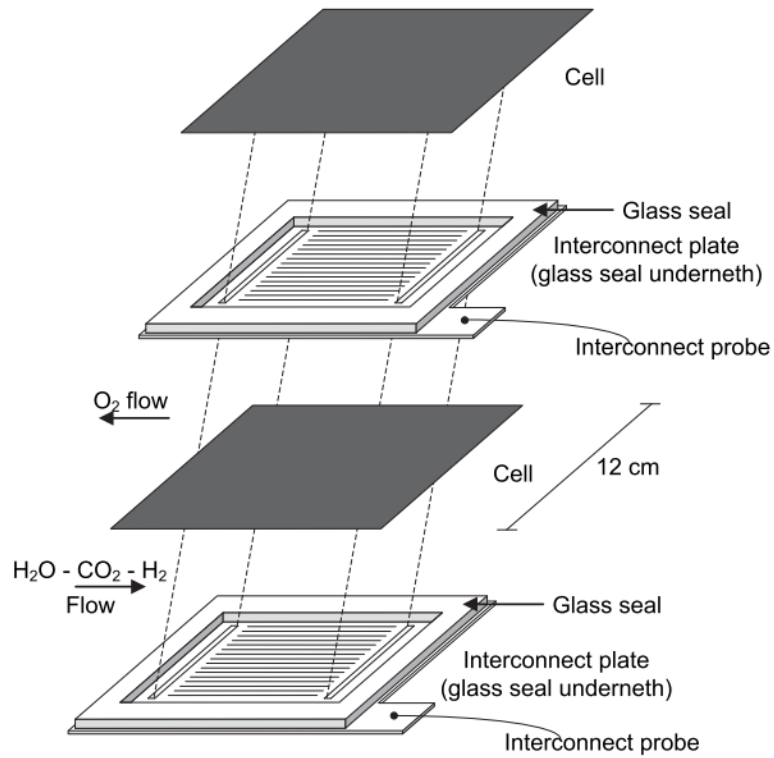
Figure 2.1: Schematic diagram of a two-cell stack assembly from DTU Energy Conversion (Ebbesen et al., 2011)
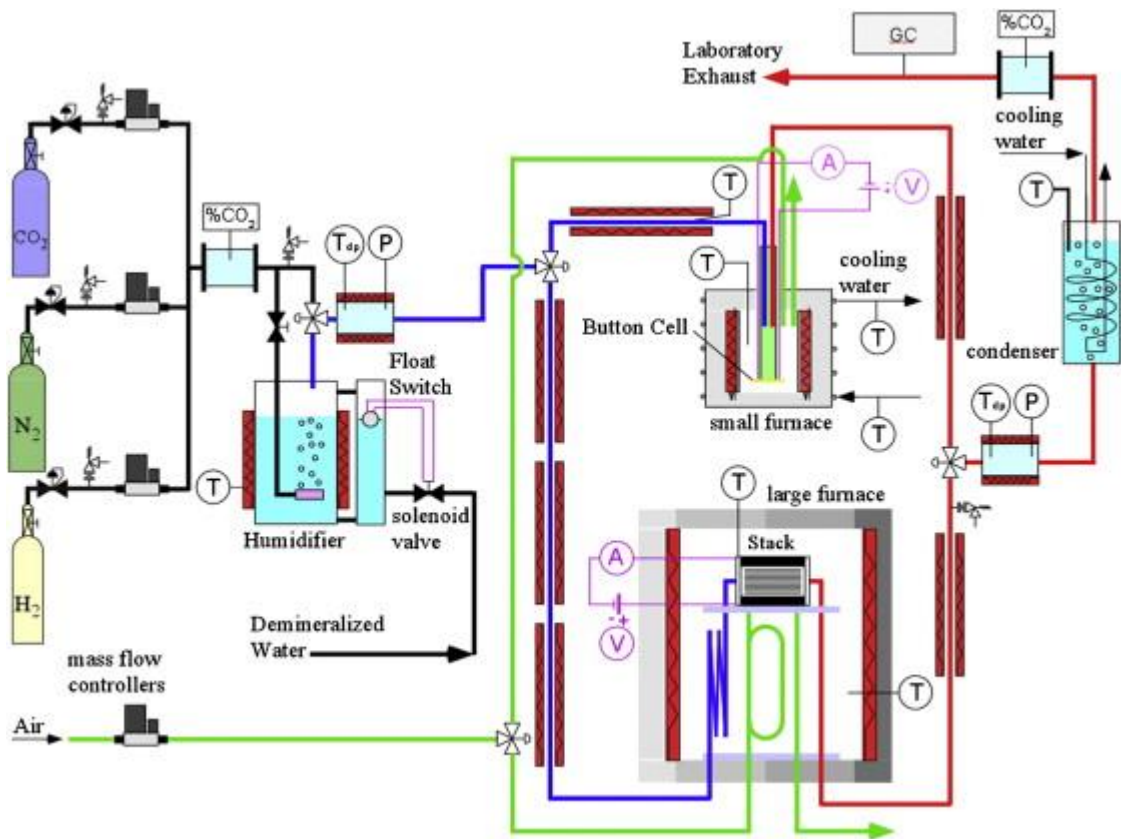
Figure 2.2: Schematic diagram of the bench-scale SOEC system from Idaho National Laboratory (Stoots et al., 2010)

For instance, Figure 2.2 depicts the schematic diagram of the lab-scale SOEC rig developed at the Idaho National Laboratory (INL) in USA. Details of the SOEC stack are provided in Table 2.1. In this system, BOP components and their functions are as follows:

- Detecting systems such as thermocouples, infrared sensors and gas chromatography to monitor gas line temperatures, inlet reactant concentrations and product mole compositions, respectively.

- Mass flow controllers to establish inlet reactant flowrates.

- N_2 as an inert gas carrier to allow independent variations of flowrates and partial pressures.

- Voltage probes to measure each cell voltage and impedance.

- Condenser to remove residual water from the produced syngas (Stoots et al., 2009, 2010).

2.1.1.2. Relevant studies

Compared to H_2O electrolysis, CO_2/H_2O co-electrolysis is somewhat complicated due to H_2O and CO_2 reduction through WGS and RWGS reactions, respectively. Though some studies focus on the kinetics of CO_2/H_2O co-electrolysis, there are still some disputes regarding the reaction pathways. To elaborate, Stoots et al. (2009) from INL in USA assessed the electrochemical performance of SOEC electrodes during electrolysis and co-electrolysis. As observed in Figure 2.3, the operating voltages of H_2O electrolysis and CO_2/H_2O co-electrolysis were very comparable. Similar results were reported by Kim-Lohsoontorn and Bae (2011) using Ni-GDC/YSZ/LSCF cell components.
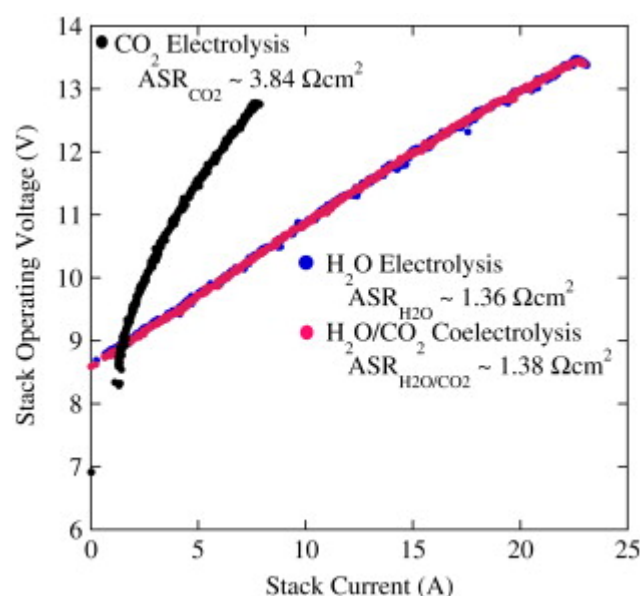
Figure 2.3: Operating voltages for co-electrolysis and electrolysis reactions (Stoots et al., 2010)

The authors concluded that during co-electrolysis, CO_2 reduction to CO is mostly through RWGS but not from CO_2 electrolysis. On the other hand, experimental results using SOEC rigs from DTU Energy Conversion in Denmark (Graves et al., 2011) and Tsinghua University in China (Li et al., 2013) showed that the electrochemical impedance and polarisation voltages of co-electrolysis were between those of electrolysis reactions. Hence, they concluded that CO was synthesised from both CO_2 electrolysis and RWGS reactions.

The effects of operating conditions on SOEC performance were also investigated. Yang et al. (2015) reported that increasing SOEC temperature from 800 to 900℃ decreases the polarisation resistance of electrodes from 0.27 to 0.14 Ω using Ni-SDC-YSZ/YSZ/LSM-SDC-YSZ and $25\%CO_2/50\%H_2O/25\%H_2$ feed gas composition (mol%). Moreover, Li et al. (2013) found that the ohmic resistances dropped from 1.01 to 0.22 Ω when the operating temperature increased from 550 to 750℃.

Chen et al. (2015) observed that CO and H_2 contents in the produced syngas respectively increase from 19 to 37% and 29 to 41% when the current density rises from 0.2 to 1.0 A/cm^2 using Ni-YSZ/YSZ/LSCF cell configuration and $40\%CO_2/40\%H_2O/20\%H_2$ feed gas composition. Comparable results were found by Cinti et al. (2016) for various feed gas compositions using the SOEC rig from FuelCell Lab in Italy. Therefore, the authors concluded that the outlet syngas composition can be adjusted by varying the applied current density and feed gas composition.

The effects of operating pressure were investigated by Riedel et al. (2020) using a 10-cell stack made of Ni-CGO/YSZ/LSCF materials and $30\%CO_2/60\%H_2O/10\%H_2$ feed gas composition. Their results indicated that high pressures favour the methanation reaction since CH_4 mol% increased from 0.2 to 4.9% with pressure increase from 1.4 to 8.0 bar at 790℃ and 0.2 A/cm^2. Similar results were found by Bernadet et al. (2017) using the SOEC rig from DTU Energy Conversion.

The durability of SOEC systems was also studied. Moçoteguy and Brisse (2013) assessed SOEC degradation mechanisms and grouped them into thermal failure leading to mechanical stress, structural degradation arising from component deterioration and electrochemical or chemical degradation. Among them, it is widely believed that structural degradation is one of the most noteworthy issues during long-term operations (Sohal et al., 2012; Moçoteguy and Brisse, 2013; Nerat and Juričić, 2018).

Several studies on SOEC degradation have been performed at DTU Energy Conversion using Ni-YSZ/YSZ/LSM-YSZ cell configuration at 800 – 850℃ and up to 1.5 A/cm^2 current density. SOEC rigs were operated for up to 1,500 hours and achieved a reactant conversion of 60% (Graves et al., 2011, 2015; Chen et al., 2013; Sun et al., 2013). Agersted et al. (2016) from DTU Energy Conversion also investigated SOEC durability using Ni-YSZ/YSZ/LSCF-CGO component materials at 700 – 800℃. SOEC stack was operated for 2,200 hours at 0.25 A/cm^2 current density and additional 3,800 hours at 0.5 A/cm^2 current density with 50% reactant conversion. The authors reported that adding the CGO barrier layer between the anode and electrolyte considerably decreases SOEC degradation rate by 68.9%. Several other advanced materials were therefore studied to improve SOEC durability during co-electrolysis such as SDC, BSCF, SSC-SDC and BSCF-SDC. A good review of these novel SOEC materials was carried out by Zheng et al. (2017).

2.1.2. Pilot plants of SOEC for CO₂/H₂O co-electrolysis and relevant experimental studies

The limited size of single cells (below 100 cm^2) calls for the design of SOEC modules to achieve the required syngas production for meeting the commercial-scale demands (Yun Zheng et al., 2017). Successful implementation of SOEC rigs at a pilot-scale bridges the gap between lab-scale experiments and commercial applications.

Table 2.2: Summary description of SOEC pilot projects for CO₂/H₂O co-electrolysis (CORDIS, 2019; CSIRO, 2021)

Parameter	ECo	Liquid fuel carrier R&D
Location	Lyngby, Denmark	Victoria, Australia
Start date	May 2016	September 2018
Duration	3 years	3 years
End-products	Syngas, methane, liquid fuels	Syngas, hydrogen
Status	Operating	Completed
Budget	€3.24 million	$2.5 million
Funded by	EU Framework program	ARENA
Coordinator	DTU Energy Conversion	CSIRO Energy

However, only two projects (ECo and Liquid fuel carrier R&D projects) were found in the open literature with the aim to increase the technology readiness level (TRL) of SOEC rigs during co-electrolysis from 3 to 5. Details on these projects are given in Table 2.2. Despite the successful design of electrode materials and TEA analysis at large-scale, SOEC stacks were only tested at a laboratory-scale (Wang et al., 2019; Kulkarni et al., 2021). Hence, pilot plants of SOEC rigs for CO_2/H_2O co-electrolysis are yet to be built and operated.

2.1.3. Commercial plants of SOEC for CO_2/H_2O co-electrolysis and relevant experimental studies

To date, no commercial plants and/or planned projects of SOEC rigs for CO_2/H_2O co-electrolysis have been reported in the open literature.

2.2. Rigs for FTS using syngas and experimental studies

2.2.1. Lab rigs of FTS for liquid fuel synthesis and relevant experimental studies

Several lab-scale FTS rigs can be found in the literature with FTS reactor size usually equal to or less than 1.0 L (Edwards, 2012). R&D activities on lab-scale FTS rigs using syngas were reviewed by Saeidi et al. (2014) and Martinelli et al. (2020). A summary of a few experimental studies that achieved more than 70.0% selectivity towards liquid fuel (C_{5+}) at a laboratory-scale as well as FTS reactor details is provided in Table 2.3. It can be seen that up to 94.2%, 91.6% and 86.3% CO conversion, C_{5+} selectivity and yield, respectively have been reported during lab-scale experiments with CH_4 selectivity between 3.4 to 19.7%.

FTS process using syngas has been operated since 1923 over various metals catalysts, for instance, Co, Fe, Ni and Ru. Under practical operating conditions, Ru is the most active catalyst for producing liquid fuel hydrocarbons (HCs) whereas, Ni essentially promotes CH_4 synthesis. However, Ru was found not suitable for large-scale FTS applications due to its high cost and low availability. Therefore, Co and Fe-based are the most viable catalysts for the FTS process (Saeidi et al., 2015; Porosoff et al., 2016).

Table 2.3: Summary of studies performed for FTS process to liquid fuels at lab-scale

Reactor type	Reactor volume (mL)	H_2/CO	Catalyst	Operating T and P	X_{CO} (%)	Selectivity (%)		C_{5+} yield (%)	Reference
						CH_4	C_{5+}		
MCR	2.0	2.1	Co-Re/Al$_2$O$_3$	225°C and 20 bar	91.0	8.0	87.0	79.2	(Myrstad et al., 2009)
Monolithic	N/S	2.0	Co-Re/Al$_2$O$_3$	210-232°C and 20 bar	65.0	10.0	88.0	57.2	(W. Liu et al., 2009)
FBR	1.4	2.1	Co-Re/Al$_2$O$_3$	228°C and 20 bar	77.0	9.0	85.0	65.4	(Myrstad et al., 2009)
Monolithic	171.0	2.0	Co-Mo/Al$_2$O$_3$ nanocatalyst	240°C and 35 bar	81.0	13.2	83.9	67.9	(Farzad et al., 2014)
FBR	N/S	2.0	Fe-Na/CNT	300°C and 20 bar	75.3	3.4	75.2	56.6	(Cheng et al., 2015)
SCBR	1,000.0	0.7	Fe-Cu-K/SiO$_2$	260°C and 22.5 bar	84.0	4.5	75.6	63.5	(Todic et al., 2016)
FBR	22.6	1.0	Fe-Mn/HZSM-5	320°C and 30 bar	86.7	10.8	66.1	57.3	(Xu et al., 2018)
FBR	10.0	2.0	Ru/Co-Mg-Zr/SAD	220°C and 30 bar	94.2	5.9	91.6	86.3	(Mandal et al., 2018)
FBR	25.0	2.0	Co/SBA-15	230°C and 20 bar	74.5	19.7	71.0	52.9	(Li et al., 2021)

2.2.1.1. Co-based catalysts

Co catalysts have the advantage to operate at low pressures between 1 to 10 bar and are cheaper than Ru catalysts. Furthermore, Co oxides showed less probability of re-oxidation in H_2O-containing reaction mediums than Fe oxides (Adeleke et al., 2020). Co content and choice of support are important factors to optimally perform the FTS process. A Co-based catalyst usually contains 15 to 30wt.% Co and is deposited on supports with high reaction surface area. This increases the number of active Co sites during the FTS process and considerably influences the catalyst's adsorption, activity and selectivity properties.

The most common supports include Al_2O_3, carbon material (C), SiO_2 and TiO_2 (Shimura et al., 2015; Adeleke et al., 2020). At 225°C, 1 bar and using H_2/CO ratio of 2 in FBR, the FTS activity of Co catalyst supports were classified as follows: $Co/MgO < Co/C < Co/SiO_2 < Co/Al_2O_3 < Co/TiO_2$ (Reuel et al., 1984). The reaction conditions also affect the activity of Co catalysts. The effect of CO_2 in the syngas was studied using FBR and Co-based catalysts such as Co/Al_2O_3 (Zhang et al., 2002; Scalbert et al., 2015), Co/SiO_2 (Chen et al., 2018), Co/SiO_2-HZSM/5 (Li et al., 2010) and Co/Carbon nanofibers (Díaz et al., 2014). The results indicated that CH_4 selectivity increases with CO_2 mole fraction in the feed gas. This is because CO_2 in the feed stream could limit the WGS reaction and/or CO_2 and CO are competing during adsorption on the active catalyst sites (Díaz et al., 2014).

Table 2.4: Effects of operating parameters on FTS process to liquid fuels using Co-based catalysts (Horáček, 2020)

Parameter	X_{CO}	Selectivity	
		CH_4	C_{5+}
Increasing T	Increase	Increase	Decrease
Increasing P	Increase	Decrease	Increase
Increasing GHSV	Decrease	Unchanged	Decrease
Increasing H_2/CO	Increase	Increase	Increase

Horáček (2020) analysed the influence of operating conditions (including temperature (T), pressure (P), gas hourly space velocity (GHSV) and CO/H_2 ratio) on FTS performance using Co/ZrO_2, Co/SiC, Co/SiO_2, Co/Al_2O_3 and Co/TiO_2 catalysts in FBR and slurry-phase reactors. The results of this study are presented in Table 2.4. The effect of water during FTS using Co-based catalysts is yet to be clarified. Some studies suggested that water addition has a negligible effect on the overall FTS reaction rate (Jacobs et al., 2007; Botes, 2009) whereas, others

reported a positive water effect on the catalyst activity such as better reactant diffusion and lower CH_4 selectivity (Ma et al., 2011, 2014).

Jacobs et al. (2007) explained that the effect of water depends on the support type and the strength of its interaction with Co particles. The strength of interaction for different supports was classified as follows: $SiO_2 < TiO_2 < Al_2O_3$. Weak interactions showed a positive water effect whilst strong interactions led to a negative water effect. However, for Co/Al_2O_3 both positive and negative water effects have been reported (Botes, 2009; Ma et al., 2011). This may explain why Todić et al. (2015) concluded that the effect of water with Co-based catalysts is somewhat conflicting as it depends on several parameters including H_2O content, partial pressure, catalyst support, loading and promoter.

Another important factor for the FTS process using Co catalyst is the type of reactor and/or reactor design. Myrstad et al. (2009) compared the performance of MCR and FBR during FTS using Co/Al_2O_3 promoted with 0.5–1.0wt.% Re at 20–30 bar, 225–240°C and $CO/H_2=2.1$. Both reactors showed a CH_4 selectivity between 8–12%. However, MCR achieved up to 91% CO conversion and 87% C_{5+} selectivity for a time on stream (TOS) of 120 hrs whereas, FBR reached 77% CO conversion and 85% C_{5+} selectivity for a longer TOS of 130 hrs. Furthermore, the relative catalyst deactivation rate in FBR was 2.2 times higher than that of MCR.

Piermartini et al. (2017) assessed the effect of channel widths of MCR on product distribution during FTS at 30 bar, 215–230°C and CO/H_2 of 1.8 using Co/Al_2O_3 promoted with 0.5wt.% Re. They observed that when increasing the channel width from 0.8 to 1.5 mm, α decreased by 2.1–3.3% i.e. more light HCs and less wax with CH_4 selectivity up to 20%. This is due to heat transfer deficits in wider structures. Monolithic reactors were studied by Liu et al. (2009) and Farzad et al. (2014) using Co/Al_2O_3 and carbon nanotubes supported Co catalysts respectively. Both studies achieved 80% selectivity towards C_{5+} with less than 15% CH_4 selectivity at 15–35 bar, 220–240°C and CO/H_2 ratio of 2.

2.2.1.2. Fe-based catalysts

Fe catalysts have lower costs than Co, Ni and Ru catalysts. Furthermore, they can be used for both LT and HT-FTS processes giving them a wider range of operating temperatures (Saeidi et al., 2015). Riedel et al. (1999) compared the activity of Co and Fe-based catalysts for CO_2-containing syngas in FBR using a 30 ml/min feed flowrate at 10 bar and temperatures of 250°C for Fe and 190°C for Co. Increasing CO_2 content in syngas resulted in higher CH_4 synthesis for Co catalysts while Fe-based catalysts showed a better formation of light olefins and liquid HCs

with no excessive CH_4 due to higher WGS activity. This is because, in the presence of Fe catalysts, the WGS reaction consumes H_2O obtained from FTS to produce additional H_2 and CO_2 (Cano et al., 2017).

Fe-based catalysts usually require promoters to enhance the catalyst's performance and stability during the FTS process. Studies reported that K promoter donates electrons towards Fe which improves FTS activity by increasing CO adsorption, suppressing CH_4 formation and promoting higher HCs synthesis (Zhang et al., 2010; Cheng et al., 2016). It was observed that the addition of alkaline metal promoters (such as Mg and Ca) increases the production of liquid fuels and enhances Fe stability by reducing the catalyst carburisation (Yang et al., 2006; Tao et al., 2006). Whereas, the use of Mn promoter favoured CO hydrogenation light C_2-C_4 olefins selectivity (Liu et al., 2015).

The importance of Fe supports was demonstrated by Torres Galvis et al. (2012) in their comparative experiments using bulk Fe and various supported Fe nanocatalysts (including Fe/CNF, Fe/α-Al_2O_3, Fe/γ-Al_2O_3, Fe/SiO_2 and Fe/β-SiC). Figure 2.4 portrays the FTS activity (expressed as FTY) and product selectivities after 64 hours of reaction at 340°C, 10 bar and H_2/CO ratio of 1. Fe/α-Al_2O_3 and Fe/CNF exhibited the highest selectivity to C_2-C_4 olefins and C_{5+} HCs with less than 15% CH_4 selectivity. This was due to the extensive carbon filament growth and particle fragmentation observed in bulk Fe which inhibited the catalyst performance (Galvis et al., 2012).
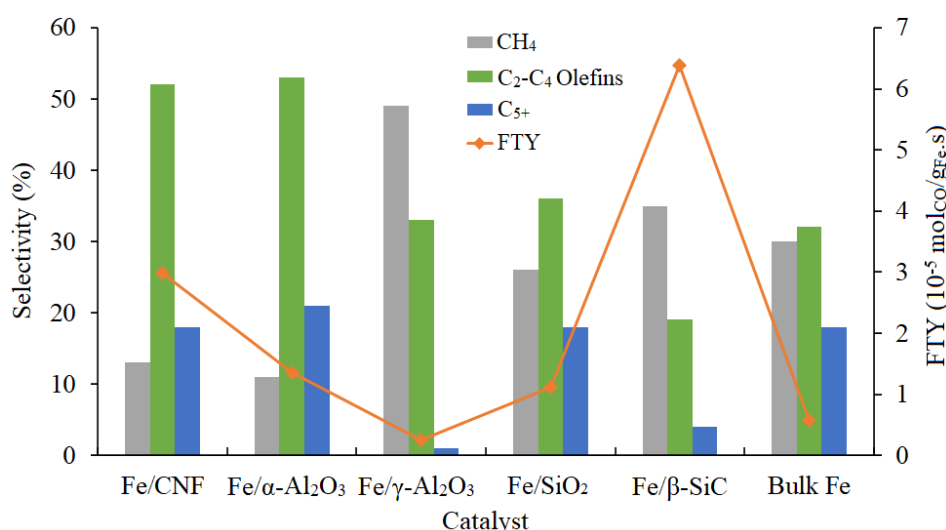
Figure 2.4: FTS performance using unsupported and supported Fe catalysts. Data obtained from (Galvis et al., 2012)

The operating conditions are also important parameters to consider during the FTS process to liquid HCs using Fe-based catalysts. Todic et al. (2016) assessed the effect of temperature,

pressure and H_2/CO ratio on product selectivity during FTS using Fe-Cu-K/SiO_2 in a 1.0 L slurry reactor. They found that an increase in pressure from 8 to 25 bar led to higher selectivity towards C_{5+} products with lower CH_4 formation. On the other hand, increasing H_2/CO and temperature (from 0.6 to 2.0 and 220 to 260℃, respectively) decreased C_{5+} selectivity whereas CH_4 synthesis increased. Similar results were observed by Mirzaei et al. (2009) using Fe-Mn/Al_2O_3 in FBR at 260-420℃, 1-15 bar and H_2/CO ratio of 1-3.

The effect of temperature on CO conversion was studied by Mierczynski et al. (2018) using Fe/Al_2O_3-Cr_2O_3 in a FBR at 30 bar with H_2/CO of 2 and 90 ml/min flowrate. The authors reported that increasing the reaction temperature increases CO conversion and achieved 75% CO conversion at 280℃. Mirzaei et al. (2009) also analysed the effect of operating conditions on CO conversion. They concluded that CO conversion increases with H_2/CO ratio and temperature whilst higher pressures decrease CO conversion.

H_2O is another key parameter affecting the FTS process. Varying amounts of H_2O are produced during FTS depending on the reaction conditions which may negatively affect FTS reaction rates and product selectivities (Teimouri et al., 2021). Pendyala et al. (2010) investigated the effect of H_2O on FTS performance using K-promoted Fe catalyst in a 1.0 L continuous stirred tank reactor (CSTR) at 13 bar, H_2/CO of 0.7 and different temperatures. Their results indicated that at 230℃, the addition of 10 vol% H_2O in the feed gas decreased CO conversion from 45 to 15%. However, at 270℃, CO conversion increases with vol% H_2O and reached 80% at 15 vol% H_2O. This was because lower temperature increases Fe deactivation due to Fe_3O_4 phase transformation (Pendyala et al., 2010; Teimouri et al., 2021).

2.2.2. Pilot plants of FTS for liquid fuel synthesis and relevant experimental studies

Though FTS process using syngas has been successfully deployed at commercial-scale, this section provides a few examples of FTS rigs at pilot-scale. Table 2.5 summarises the specification of three FTS pilot plants for liquid fuel synthesis.

Shimura et al. (2015) studied the effects of metal promoters (Ba, Ca, Ce, La, Mg, Mn, Mo, Sr, Ti, V, Y, Zn and Zr) on Co/Al_2O_3 catalyst performance using the 12.5L SCBR from the BTL facility in Japan during FTS at 230℃, 10 bar and 100 ml/min flowrate. They observed that La and V promoters improve Co/Al_2O_3 activity by increasing Co surface area and turnover frequency (TOF). The addition of 2%La and 0.5%V on Co/Al_2O_3 achieved 77% CO conversion (1.6 times higher than Co/Al_2O_3 alone), 81% C_{5+} and 8% CH_4 selectivities (Shimura et al.,

2015). Experimental investigations on Mark II plant were reported by Ermolaev et al. (2015). The authors measured C_{5+} productivity, CO conversion and hot spot temperature to assess the potential of scaling-up Mark II from pilot to commercial-scale.

Table 2.5: Summary of operational FTS pilot plants using syngas (Y. Liu et al., 2009; Ermolaev et al., 2015; Placido et al., 2018)

Parameter	Mark II	CBTL	BTL
Company	INFRA Technology	University of Kentucky	AIST Chugoku Center
Location	Houston, USA	Kentucky, USA	Hiroshima, Japan
Plant capacity	7.2 ton/day	1 bbl/day	15.6 L/day
Commissioned year	2014	2018	2008
Reactor type	FBR	MCR	SCBR
Catalyst	Co-Z	Co-Pt/Al$_2$O$_3$	Co-Mn-Zr/SiO$_2$
Raw material	N/S	Coal and biomass	Biomass (Wood)

Recently, a power-to-fuels technology was experimentally verified by Vázquez et al. (2018) at the SOLETAIR pilot plant. Figure 2.5 portrays the process flow diagram of SOLETAIR pilot facility. The plant is located at the Lappeenranta University of Technology in Finland and was launched in 2017. It aims to produce liquid fuels from a two-step synthesis unit (RWGS and FTS) using Co-based catalysts and CO_2 from direct air capture (DAC) unit and H_2 from a proton exchange membrane (PEM) electrolyser. Although initial results indicated successful synthesis of liquid fuels with a production rate of 6.2 kg/day, the authors concluded that the pilot facility was still at a proof-of-concept stage owing to CO_2 and H_2 production limitations from the DAC and PEM units, respectively (Vázquez et al., 2018).
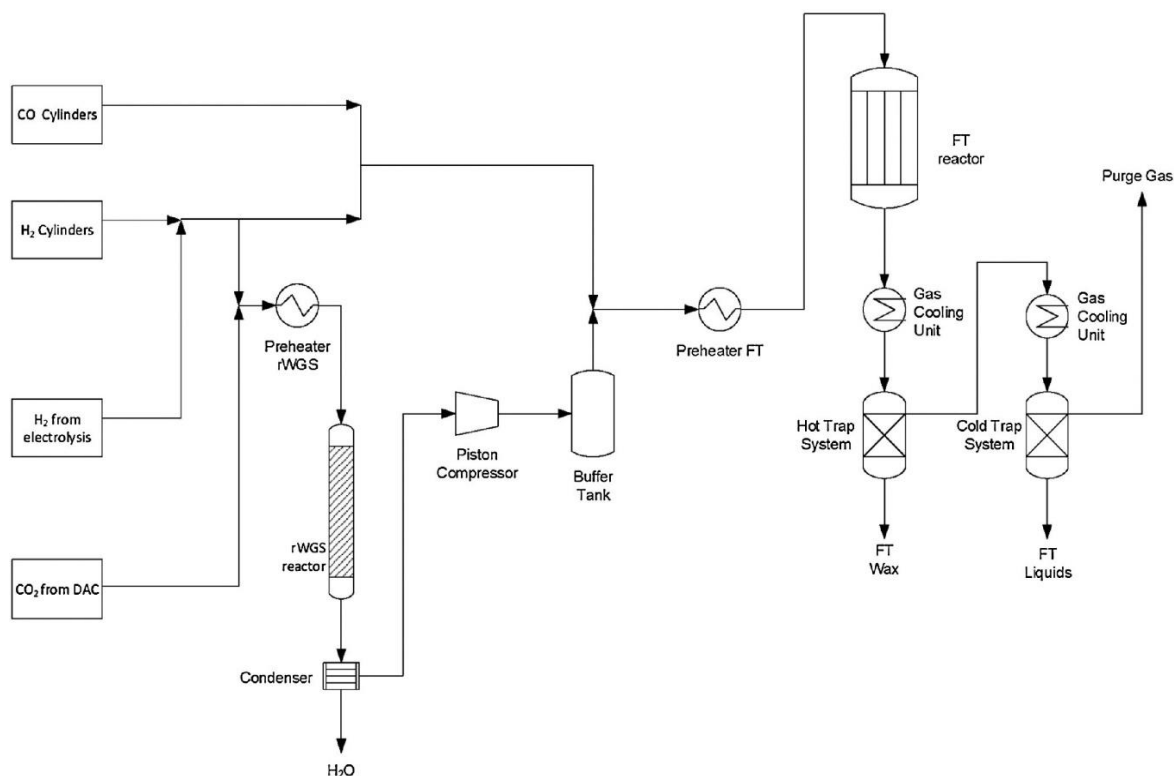
Figure 2.5: Process flow diagram of the SOLETAIR pilot facility (Vázquez et al., 2018)

2.2.3. Commercial plants of FTS for liquid fuel synthesis and relevant experimental studies

FTS process using syngas has been widely deployed at commercial-scale in several industries across the world. A few successful operational FTS plants at industrial-scale are elaborated in Table 2.6. Except for PetroSA in South Africa, all commercial FTS plants using natural gas as raw material are operated by Shell and Sasol (Martinelli et al., 2020). Although a plant capacity of 165,000 bbl/day has been successfully operated, syngas is essentially produced from non-renewable sources which release large amounts of CO_2 into the atmosphere.

2.3. Rigs for direct CO_2-FTS and experimental studies

The direct CO_2 conversion into C_{2+} hydrocarbons via the modified FTS process has recently gained much attention due to its ease of operation. This process combines CO_2 reduction to CO via RWGS and CO hydrogenation to HCs via FTS in a single reactor. Therefore, efficient catalysts should be active for both RWGS and FTS reactions under the same operating conditions (Ye et al., 2019). Similar to the traditional FTS process, products from the modified CO_2-FTS process can be wide depending on the catalyst's type, composition and structure. This section focuses on the synthesis of liquid HCs (C_{5+}).

34

Table 2.6: Summary of operational FTS plants at commercial-scale (Martinelli et al., 2020)

Company	Location	Reactor type	Raw material	Catalyst	Commissioned year	Capacity (bbl/day)
PetroSA	Mossel Bay, South Africa	CFB	Natural gas	Fe	1992	36,000
Shell	Bintulu, Malaysia	FBR	Natural gas	Co/SiO_2	1993	14,700
Sasol	Sasolburg, South Africa	SBCR	Coal	Fe	1994	2,500
Sasol	Secunda, South Africa	FFB	Coal	Fe	1995	165,000
Oryx GTL	Ras Laffan, Qatar	SBCR	Natural gas	Co/Al_2O_3	2006	34,000
Synfuels China	Inner Mongolia, China	SBCR	Coal	Fe	2009	160,000
Pearl GTL	Ras Laffan, Qatar	FBR	Natural gas	Co/SiO_2	2011	140,000
Escravos GTL	Escravos, Nigeria	SBCR	Coal	Co/Al_2O_3	2014	34,000

Table 2.7: Summary of studies performed for CO_2-FTS process to liquid fuels at lab-scale

Reactor type	Reactor diameter (mm)	H_2/CO_2	Catalyst	Operating T and P	X_{CO2} (%)	Selectivity (%)		C_{5+} yield (%)	Reference
						CH_4	C_{5+}		
FBR	N/S	3.0	$CuFeO_2$-6	300°C and 10 bar	17.3	2.7	66.3	11.5	(Choi et al., 2017)
FBR	14.0	1.0	Na-Fe_3O_4/HZSM-5	320°C and 30 bar	22.0	4.0	78.0	17.2	(Wei et al., 2017)
FBR	10.0	3.0	Fe-K/SiC	300°C and 25 bar	41.7	10.3	56.0	23.4	(Jiang et al., 2018)
FBR	N/S	3.0	Co-Cu/TiO_2	240°C and 50 bar	18.4	26.1	42.1	7.7	(Shi et al., 2018)
FBR	7.0	2.7	Co/MIL-53(Al)	260°C and 30 bar	25.3	35.2	35.0	8.9	(Tarasov et al., 2018)
FBR	14.0	2.0	Na-Fe_3O_4/HMCM-22	320°C and 30 bar	26.0	8.0	74.0	19.2	(Wei et al., 2018)
FBR	N/S	1.0	Co_6/MnO_x	200°C and 40 bar	15.3	N/S	53.2	8.1	(He et al., 2019)
FBR	7.4	3.0	Fe-K/MPC	300°C and 25 bar	50.6	15.4	44.5	22.5	(Hwang et al., 2020)
FBR	6.0	3.0	Na-Fe@C/ HZSM-5-0.2	320°C and 30 bar	33.3	4.8	84.8	28.2	(Y. Wang et al., 2020)
FBR	10.0	3.0	Fe-Mn-K	320°C and 30 bar	38.2	10.4	61.9	22.3	(Yao et al., 2020)

2.3.1. Lab rigs of CO_2-FTS for liquid fuel synthesis and relevant experimental studies

Several studies have been performed on the CO_2-FTS process to liquid fuels at laboratory-scale. In comparison to the traditional FTS process, CO_2 conversion via the modified CO_2-FTS process is more challenging not only due to CO_2 thermodynamic stability but also because the RWGS reaction is endothermic ($\Delta H_{573K} = 38$ kJ/mol) hence requires higher temperatures whilst FTS reactions are exothermic ($\Delta H_{573K} = -166$ kJ/mol) and high temperatures tend to favour light HCs with lower selectivity towards liquid C_{5+} HCs (He et al., 2019; Ye et al., 2019).

Table 2.7 summarises a few studies on the CO_2-FTS process to liquid fuels performed at lab-scale. All experiments were carried out using FBRs with an inner diameter between 6.0 to 14.0 mm and up to 450 mm in height. Although up to 84.8% C_{5+} selectivity has been achieved, the yield of liquid fuels was found below 29.0% due to low CO_2 conversion. It is widely believed that low CO_2 conversion during the CO_2-FTS process arises from excessive water produced from both RWGS and FTS reactions which negatively affect RWGS reaction rates (Guo et al., 2018; Saeidi et al., 2021).

Co-based catalysts showed fairly low selectivities towards C_{5+} HCs between 12.1 to 53.2% using Co-Pt-K/SiO$_2$ (Owen et al., 2013), Co/MIL-53(Al) (Tarasov et al., 2018), Co-Cu/TiO$_2$ (Shi et al., 2018) and Co$_6$/MnO$_x$ (He et al., 2019) catalysts. Experimental details on these studies are elaborated in Table 2.7. On the other hand, Fe-based catalysts showed a good ability to catalyse both RWGS and FTS reactions thus, have been applied in several studies to produce liquid fuels via the modified CO_2-FTS process (Ding et al., 2014; Choi et al., 2017; Jiang et al., 2018; Khan et al., 2020; Khangale et al., 2020; Yao et al., 2020; Hwang et al., 2020).

Recently, Wei et al. (2017) introduced multifunctional Fe-based catalysts supported on zeolites to control HCs selectivity during the CO_2-FTS process. They prepared Na-Fe$_3$O$_4$/HZSM-5 nanocatalyst and reported for the first time the direct synthesis of gasoline with 78.6% selectivity via CO_2-FTS in a FBR at 30 bar, 340℃, H$_2$/CO$_2$ of 1.0. Characterization results (Figure 2.6) revealed that the acid sites on HZSM-5 zeolite were responsible for the surface basicity as well as the oligomerization, isomerization and aromatization of CO_2 to long-chain HCs (Wei et al., 2017).
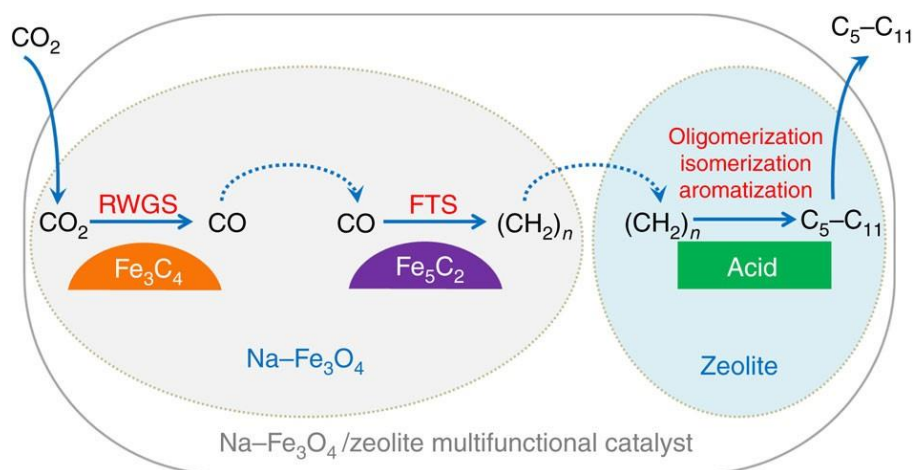
Figure 2.6: CO_2-FTS reaction scheme to gasoline-range hydrocarbons (Wei et al., 2017)

The acidic properties of zeolites during CO_2-FTS in a FBR at 30 bar, 320℃, H_2/CO_2 of 3 and using Na-Fe@C/ HZSM-5 were further studied by Wang et al. (2020). The authors performed FTIR spectroscopy and confirmed the existence of Lewis and Brønsted acid sites in HZSM-5 zeolite. Their analysis concluded that the synergistic effect between Lewis and Brønsted acid sites plays a key role in enhancing Fe catalytic performance (Y. Wang et al., 2020). Another study reported a selectivity of 74.0% towards C_{5+} HCs with 26% CO_2 conversion and 8% CH_4 selectivity using multifunctional Na-Fe_3O_4 catalyst supported on HMCM-22 zeolite for CO_2-FTS in a FBR at 30 bar, 320℃ and H_2/CO_2 of 2 (Wei et al., 2018).

The operating conditions (including temperature, pressure and H_2/CO_2 ratio) are key parameters governing CO_2-FTS product distribution and catalyst activity. Studies have shown that increasing the reaction temperature leads to higher CO_2 conversion and lower selectivity to liquid C_{5+} HCs due to the high production of methane (Jiang et al., 2018; Tarasov et al., 2018; Khangale et al., 2020). For example, for a temperature increase from 260 to 340℃, CH_4 selectivity increases from 5.0 to 11.0% and 35.2 to 53.2% using FeK (Jiang et al., 2018) and Co/MIL-53(Al) (Tarasov et al., 2018) catalysts, respectively. Jiang et al. (2018) explained that higher operating temperature would shift the RWGS Reaction (1.11) forwards leading to more CO_2 conversion.

Wei et al. (2017) studied the effects of H_2/CO_2 ratio on CO_2-FTS performance using Na-Fe_3O_4/HZSM-5 nanocatalyst in a FBR at 30 bar and 320℃. They found that increasing H_2/CO_2 ratio from 1.0 to 6.0 increases CO_2 conversion from 22.0 to 54.0%. Whereas, selectivities to gasoline fuel and methane respectively decrease (from 78.0 to 68.0%) and increase (from 4.0 to 10.0%). Similar trends were observed by (Khan et al., 2020) using $FeAlO_x$-5 catalyst at 35 bar and 330℃. On the other hand, the effect of the reaction pressure on CO_2-FTS performance

is somewhat conflicting. In a study using FeK catalyst in a FBR at 300°C and H_2/CO_2 of 3, no significant changes to both product selectivity and CO_2 conversion were observed when varying the pressure from 10 to 30 bar (Jiang et al., 2018).

However, Khangale et al. (2020) found that an increase in pressure from 1 to 20 bar leads to higher CO_2 conversion and CH_4 selectivity varying respectively from 13.3 to 41.0% and 18.5 to 88.9% whilst, C_{5+} selectivity remains almost unchanged. Another study reported that changing the operating pressure from 5 to 35 bar resulted in CO_2 conversion and C_{5+} selectivity increase from 2.6 to 26.7% and 40.8 to 71.7%, respectively with a decrease in CH_4 selectivity from roughly 52.0 to 8.0% using $FeAlO_x$-5 catalyst at 330°C and H_2/CO_2 ratio of 2 (Khan et al., 2020).

2.3.2. Pilot plants of CO_2-FTS for liquid fuel synthesis and relevant experimental studies

To date, no pilot plants of the modified CO_2-FTS process for liquid fuel synthesis have been reported in the open literature.

2.3.3. Commercial plants of CO_2-FTS for liquid fuel synthesis and relevant experimental studies

Though the traditional FTS process using syngas has been successfully deployed at commercial-scale, no commercial plants of the modified CO_2-FTS process for liquid fuel synthesis have been found in the open literature.

2.4. Modelling/simulation, optimisation and TEA of SOEC for CO_2/H_2O co-electrolysis

2.4.1. Modelling/simulation and optimisation studies on SOEC performance

SOEC models reported in the literature were all mechanistic models based on first principles and laws of physics. To date, no empirical SOEC model under co-electrolysis was found in the open literature. 1D and 2D steady-state models of planar SOECs were proposed by Ni (2012a) and Ni (2012b) respectively. The models were based on mass/heat transfer and included electrochemical reactions, methanation and RWGS reaction kinetics to assess their contributions during CO_2 and H_2O co-electrolysis. Their results indicated that at a temperature

range of 600 – 800℃ and low operating voltages, RWGS contributes to CO formation and does not promote CH_4 synthesis.

Stempien et al. (2013) carried out macro-level and steady-state modelling in Aspen HYSYS® of planar SOEC combined with a power plant. The authors performed steady-state optimization to investigate the effects of syngas recirculation, mole flux and operating temperature on SOEC performance. They observed that higher temperatures improve SOEC performance and the optimum designs were 800℃, 10 – 20% recycle ratio and 0.9 – 1.3 A/cm² for a syngas efficiency of 46.2% at 1.54V. The syngas efficiency simply refers to as the ratio of the energy output from the heat of combustion of produced syngas to the total energy supplied to SOEC (Banerjee et al., 2018).

Menon et al. (2015) and Luo et al. (2014) investigated the effects of SOEC operating conditions and electrode microstructures on compound distributions using a 2D micro model of planar SOEC in DETCHEM™ and COMSOL MULTIPHYSICS® respectively. The models were based on electrochemistry, mass transport and the Butler-Volmer approach to evaluate electrode polarisations. A 3D steady-state model of planar SOEC was developed by Hawkes et al. (2006) using the computational fluid dynamics (CFD) technique in FLUENT software. Their study provided detailed profiles of outlet gas composition, temperature and operating voltage and reached a syngas efficiency of 55.0% at 850℃ and 1.1 V.

Dynamic SOEC models were also proposed to analyse SOEC performance during operation disturbances such as component failures and changes in operational strategies. Zheng et al. (2017) studied the transient response of temperature, voltage, power density and syngas mole fraction during operation switches from SOEC to SOFC using a 1D dynamic model. Their model considered dynamics in mass and energy conservation as well as electrochemical/chemical reactions. A 2D micro and dynamic model of tubular SOEC was developed by Luo et al. (2015) in COMSOL MULTIPHYSICS®. The model was based on electrochemical reactions, momentum and mass/heat transfer and was used to assess the transient behaviour of CO_2/H_2O co-electrolysis in SOEC systems connected to unstable and intermittent renewable energies. The authors also performed a dynamic process analysis and reported 66.0% syngas efficiency at 700℃ and 1.33V.

Banerjee et al. (2018) developed a 3D dynamic modelling using the CFD technique in DETCHEM™ to investigate large-scale applications of planar SOECs. The model incorporates mass and heat transfer, gas transport through porous electrodes and electrochemical reactions.

They also carried out steady-state process optimisation and transient response analysis during operation switches between co-electrolysis and electrolysis modes. A syngas efficiency of 68.5% was achieved at 1.3V and 850℃. Steady-state model validation was performed for all steady-state and dynamic models above-mentioned by comparing voltage versus current density against experimental data.

2.4.2. Modelling/simulation and optimisation studies on SOEC degradation

A few models were proposed to clarify degradation mechanisms within SOEC systems and improve their durability. Virkar (2010) developed a 1D steady-state model based on charge transport to understand the degradation mechanisms of anode delamination. His results indicated anode degradation is mostly due to high O_2 pressure near the anode/electrolyte interface. A 2D steady-state model of planar SOEC was proposed by Chatzichristodoulou et al. (2016) to study the distribution of electrochemical and chemical overpotential across the electrolyte. The model is based on mass transfer and charge transport and was used for process analysis of current density, temperature, pressure and feed gas composition.

Nerat and Juričić (2018) developed a 2D steady-state model of tubular SOEC in COMSOL MULTIPHYSICS®. Their model is based on energy, charge and momentum conservation and they aimed to investigate the effects of anode delamination on the SOEC conversion efficiency. Their results showed that when the delaminated-to-cell area ratio increases from 0 to 0.05, conversion efficiency drops by 0.12 at 1.0 A/cm² current density. Navasa et al. (2018) used a 3D steady-state model of planar SOEC in COMSOL MULTIPHYSICS® to study the overpotential and temperature distributions through the electrodes. Their model incorporates electrochemical reactions, species transport and mass/heat/momentum transfer to predict the spatial variations of overpotential, temperature and gas composition through the electrodes.

However, the aforementioned models were developed for SOEC operating in water electrolysis mode. Recently, Wang et al. (2019) looked into long-term SOEC operation during CO_2/H_2O co-electrolysis using a 2D steady-state model in Aspen Customer Modeler®. Nevertheless, the authors only investigated SOEC temperature and assumed a constant degradation rate of 1.4 %/1000hrs based on SOEC experiments carried out at DTU Energy Conversion. Their study concluded that thermal failures can be limited by decreasing the temperature gradient between SOEC inlet and outlet. For the modelling studies on SOEC degradation, steady-state model validation was also carried out by comparing voltage versus current density against experimental data.

2.4.3. TEA studies on SOEC for CO_2/H_2O co-electrolysis

O'Brien et al. (2009) carried out a technical analysis of large-scale syngas production using SOEC in UniSim software. The large-scale SOEC plant was designed based on experimental data obtained from the INL facility in USA. Assuming a cell active area of 225 cm^2, their results showed that a syngas production capacity of 86.4 ton/day can be achieved at 0.25 A/cm^2, 35 bar and 800℃ if 600 MW energy is supplied to the SOEC plant. However, previous experimental studies have demonstrated that high SOEC operating pressures favour CH_4 formation. Hence, the results obtained for syngas composition and/or production rate (thus, process efficiency and energy requirement) could be highly inaccurate.

Fu et al. (2010) performed a TEA study on SOECs for syngas production. The plant was simulated in Aspen Plus® using Ni-YSZ/YSZ/LSM-YSZ component material for a syngas production capacity of 5.0 ton/day. They reported that 1.61 MW of energy was required to produce 5.8 ton/day of syngas leading to a syngas production efficiency of 71.0% and a syngas cost of 775.0 €/ton. Recent TEA studies reported for SOEC under co-electrolysis are usually integrated with the FTS process for syngas synthesis. Therefore, a review of these studies was carried out in the FTS process section.

2.5. Modelling/simulation, optimisation and TEA of FTS for liquid fuel synthesis

2.5.1. Modelling/simulation and optimisation studies on FTS using syngas

Extensive works have been carried out on modelling and optimisation of FTS reactors at different dimensions. Qian et al. (2012) proposed a 1D steady-state model of slurry bubble column reactor (SBCR) for FTS based on first principles. The model accounts for the non-uniform distribution of Co/AC catalyst in SBCR and is used to analyse the effect of operating conditions on CO conversion, product selectivity and catalyst concentration along the SBCR bed. The results showed that increasing the pressure, temperature and H_2/CO ratio led to an increase in CO conversion while, SBCR bed height and liquid C_{5+} selectivity decreased (Qian et al., 2012).

Another 1D steady-state model based on mass and heat balance was developed by Hooshyar et al. (2012) to assess the effect of catalyst structuring on liquid C_{5+} synthesis in fixed-bed reactor (FBR) and SBCR. The authors observed that for SBCR, reducing the liquid axial dispersion

coefficient by 75% improves C_{5+} selectivity by 20% with 88% CO conversion. Whereas, C_{5+} synthesis is enhanced by more than 40% in FBR when the catalyst diffusion length is decreased by a factor of 2 at 53% CO conversion (Hooshyar et al., 2012).

Guettel and Turek (2009) compared the performance of conventional (SBCR and FBR) and intensified (MLR and MCR) reactors for the FTS process using a 1D steady-state modelling based on mass and heat transfer. They aimed to investigate the effect of catalyst activity on process efficiency and efficiency losses. Their results (Figure 2.7) indicated that the microchannel reactor (MCR) has the highest productivity of 473.44 bbl/day per m^3 of catalyst with 69.9% CO conversion at 249℃ followed by SBCR, monolithic loop reactor (MLR) and FBR. FBR exhibited the lowest efficiency of 9% due to severe mass transfer resistance (Guettel and Turek, 2009).
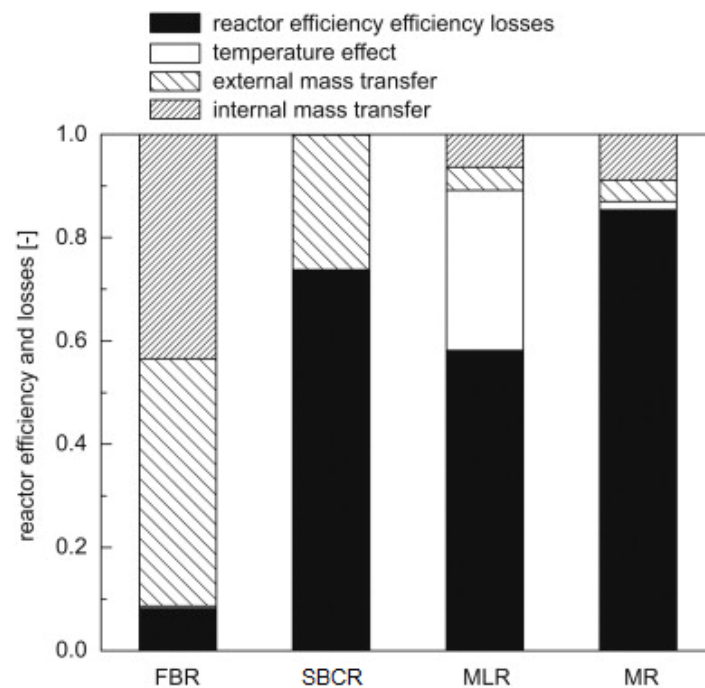
Figure 2.7: Process efficiency and losses for different FTS reactors (Guettel and Turek, 2009)

Recently, a 1D steady-state model of a wall-cooled packed bed reactor was proposed by Chandra et al. (2021) to assess the transport phenomena during the FTS process. The model is based on mass/momentum balance and includes both fluid and solid phase transport. The authors studied the effects of the reactor wall temperature and H_2/CO ratio on CO conversion and C_{5+} production. The results showed that controlling the operating/reactor temperature is paramount to achieving the highest C_{5+} selectivity (Chandra et al., 2021). It is important to point out that for all 1D models aforementioned, the software used for model implementation

was not specified and no model validation was performed which may question the validity of the reported results.

Moazami et al. (2015) studied the behaviour of FTS process and FBR performance for N_2-rich syngas using 1D steady-state modelling based on mass, species and momentum conservation in MATLAB. They performed model validation by comparing CO profiles and product selectivity against experimental data for different temperature (230–270℃), pressure (10–25 bar) and GHSV (1.8–3.6 L/g_{cat}.hr) ranges. The influence of the temperature and GHSV on CO conversion and product selectivity were also investigated.

Seyednejadian et al. (2018) developed a 1D dynamic model of SBCR in MATLAB based on mass/energy balance and LHHW kinetics for the FTS reactions. Steady-state model validation was carried out by comparing CO conversion and product selectivity for different feed flowrates (3.5, 5.0 and 7.5 m^3/hr) against experimental data. Their results indicated that steady-state condition is achieved within 10 minutes from start-up. The distribution of components along the reactor and the effects of temperature on product selectivity were also studied. A 2D steady-state model of FBR for the FTS process was developed by Ermolaev et al. (2015) to investigate the hot spot evolution in the catalytic bed. The model is based on momentum balance, mass and energy conservation and considers LHHW kinetics to describe FTS reaction rates. Model validation was performed by comparing CO conversion and C_{5+} productivity rate for different GHSV (1000–4000 h^{-1}) and temperatures (188–227℃,) against experimental data from the Mark II pilot facility.

2.5.2. TEA studies on FTS process for liquid fuel synthesis

A technical analysis of two FTS plant configurations using syngas from natural gas reforming was carried out by Selvatico et al. (2016) in Aspen Plus®. A kinetic model based on the LHHW approach was developed to assess FTS equation rates and model validation was performed using experimental data from Todic et al. (2013). Two plant configurations were studied including a recycle design with tail gas recirculation to the FTS reactor and an open-loop design wherein FTS tail gas is used for power generation. For a 500 ton/hr of syngas mass flow, 65.7 and 49.6 ton/hr liquid fuel production were observed in the recycle and open-loop configuration, respectively. However, both plant designs achieved a similar process efficiency of 43.6% (Selvatico et al., 2016).

With the aim to make the FTS process more sustainable, several TEA studies have been performed on liquid fuel production from CO_2 and H_2O using the integrated SOEC-FTS

process (Becker et al., 2012; Stempien et al., 2015; Cinti, et al., 2016; Samavati et al., 2018; Herz et al., 2018; Wang et al., 2019; Marchese et al., 2020).
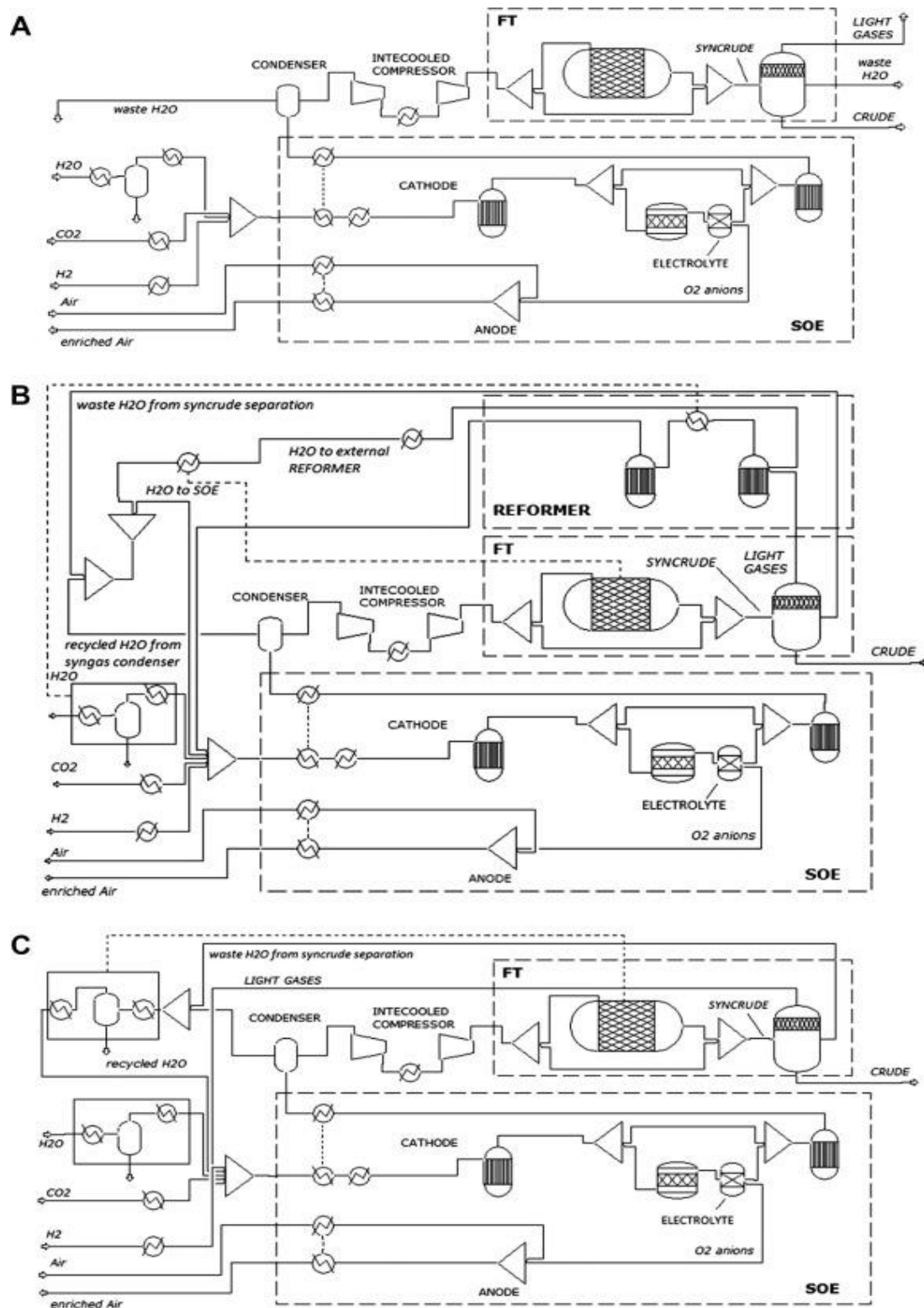
Figure 2.8: SOEC-FTS process configurations. (A): Open-loop system, (B): FTS light gas recycle to a reformer then SOEC and (C): FTS light gas recirculation to SOEC (Cinti, Baldinelli, et al., 2016)

Becker et al. (2012) carried out a TEA study to assess the coupled performance of the integrated SOEC-FTS process Aspen Plus®. They reported that 58.3 MW of energy is required to produce 19.4 kgal/day of diesel and gasoline fuels from 332.6 ton/day of CO_2. An overall process efficiency of 54.8% was achieved and the cost of products was estimated between 4.4 to 15.0 $/GGE for 0.02–0.14 $/kWh electricity cost. Stempien et al. (2015) performed a technical analysis of the SOEC-FTS system in Aspen HYSYS®. The integrated process reached 66.7% overall efficiency assuming the energy from hot streams is recovered and re-used for SOEC steam generation and feed gas compression. Another SOEC-FTS technical analysis was conducted by Cinti et al. (2016) in Aspen Plus® for a plant capacity of 1.0 bbl/day.

The authors considered three system configurations as illustrated in Figure 2.8. Their results indicated that the open-loop configuration (Figure 2.8a) has the lowest efficiency of 46.4%. Whereas, the highest overall efficiency of 57.2% was achieved by performing heat recovery and FTS tail gas recirculation to the SOEC section (Layout C in Figure 2.8). Herz et al. (2018) improved the process design proposed by Cinti et al. (2016) by adding an air combustion unit for additional syngas production using FTS light gas. The new SOEC-FTS system achieved 61.8% process efficiency (68.0% without considering 10.0% heat loss to the system).

The authors also carried out an economic assessment using 332.6 ton/day of CO_2 mass flow. They reported that the SOEC-FTS plant has a CAPEX 2.1 to 4.4 times higher than that of the existing commercial FTS plants elaborated in Table 2.6 (Herz et al., 2018). Samavati et al. (2018) performed a comparative analysis between SOEC-FTS and EG-FTS processes in Aspen Plus®. For a diesel production rate of 158.4 kgal/day and without heat recovery, the EG-FTS plant achieved a process efficiency of 57.7% whilst that of the SOEC-FTS process was 55.0%. By performing heat integration, the SOEC-FTS overall efficiency reached 78.9%.

2.6. Modelling/simulation, optimisation and TEA of direct CO_2-FTS for liquid fuel synthesis

2.6.1. Modelling/simulation and optimisation studies on direct CO_2-FTS process

Despite successful demonstrations of direct CO_2-FTS process to liquid fuels at lab-scale, very limited modelling/simulation studies for CO_2-FTS process optimisation have been found in the open literature. Meiri et al. (2017) proposed a kinetic model for CO_2-FTS process simulation in CHEMCAD. They aimed to assess the effects of reactor configuration on CO_2 conversion,

CH_4 and C_{5+} selectivities. Although their study demonstrated the importance of water removal to achieve higher CO_2-FTS reaction rates and C_{5+} selectivity, the developed kinetic model was based on experimental data with very high selectivity (between 45 to 78%) towards light HCs (Meiri et al., 2015). Therefore, the reported results on liquid fuel selectivity and/or CO_2 conversion could be highly inaccurate.

A 1-D model of a membrane reactor for the CO_2-FTS process was developed by Najari et al. (2019). The model is based on mass and heat conservation and was used to investigate the effects of in-situ water removal through a hydrophilic membrane on CO_2 conversion and hydrocarbon selectivity at different operating conditions. No model validation was performed as membrane reactors for the direct CO_2-FTS process have not been studied experimentally yet. Furthermore, the authors focused on gaseous compounds ranging from C_1 to C_4.

2.6.2. TEA studies on direct CO_2-FTS process for liquid fuel synthesis

A TEA study on direct CO_2 conversion to gasoline fuel at a commercial-scale was performed by Fernández-Torres et al. (2022) using Aspen HYSYS®. The authors aimed to investigate tail gas oxy-combustion for electricity generation using the Allam cycle, Rankine cycle and gas turbines to generate extra revenue for the CO_2-FTS plant. Their results indicated that the net electricity generation was 2.92, 1.95 and 2.06 kWh/L of produced gasoline when the CO_2-FTS plant is coupled with Allam cycle, Rankine cycle and gas turbines, respectively. Furthermore, for a gasoline production rate of 23.65 ton/hr, CAPEX and OPEX were estimated between 73 to 128 M\$ and 244 to 1951 M\$/yr respectively (Fernández-Torres et al., 2022).

2.7. Summary

In this Chapter, syngas production using SOEC systems and liquid fuel synthesis through FTS and CO_2-FTS processes were critically reviewed. The review included experimental studies carried out at laboratory, pilot and commercial scales as well as modelling/simulation, optimisation and TEA studies. The key findings are summarised below:

- Most studies investigated planar SOEC and Ni-YSZ/YSZ/LSM-YSZ component materials for syngas synthesis. Up to 10-cell stack has been tested at lab-scale with up to 60% reactant conversion for 1,500 hours. Higher SOEC temperatures decreased ohmic and polarisation resistances whereas, increasing SOEC pressure led to higher CH_4 mole fraction in the produced syngas.

- To date, no pilot and commercial plants have been reported for CO_2/H_2O co-electrolysis to syngas and CO_2-FTS process to liquid fuels.

- Fe and Co-based catalysts can effectively produce liquid fuels via the FTS process with up to 94.2% CO conversion and 86.0% C_{5+} yield. FTS process has been successfully deployed at commercial-scale with up to 160,000 bbl/day plant capacity.

- CO_2-FTS process showed promising results for direct fuel synthesis from CO_2. This was particularly true for Fe-based catalysts which achieved up to 84.8% C_{5+} selectivity. However, the C_{5+} yield was still very low (below 29.0%) due to low CO_2 conversion caused by excessive water production.

- For both FTS and CO_2-FTS processes and using Fe-based catalysts, increasing the reaction temperature results in higher CO or CO_2 conversion and lower C_{5+} selectivity. Moreover, a lower H_2/CO or H_2/CO_2 ratio promotes C_{5+} synthesis but decreases CO or CO_2 conversion.

In spite of considerable research in CO_2 conversion into syngas and liquid fuels, SOEC, FTS and CO_2-FTS processes are still facing several technical barriers. A few challenges and research gaps that need to be addressed are as follows:

- Component structural degradation is still of great concern for SOEC commercial applications. Furthermore, no modelling studies integrating SOEC component degradation during CO_2/H_2O co-electrolysis were found in the open literature.

- There are still serious concerns arising from large CO_2 emissions during the traditional FTS process. Hence, studies on more sustainable liquid fuel synthesis processes are highly required.

- Liquid fuel yield during the CO_2-FTS process is still too low for industrial applications. Moreover, the only study found on modelling/simulation and optimisation of the CO_2-FTS process to liquid fuel was based on experiments for light HCs synthesis. These underlined the need for a more accurate CO_2-FTS process model so as to find effective strategies to improve CO_2 conversion and C_{5+} yield.

The key papers from the literature that were useful to carry out this research are summarised in Table 2.8.

Table 2.8: Summary of key papers used for this research

Reference	Use in this PhD study
(Faes et al., 2009; Stempien et al., 2014; Farlenkov et al., 2015)	Provided insights on mixed potential theory of CO_2/H_2O co-electrolysis and SOEC degradation modelling.
(Cinti, Discepoli, et al., 2016)	Provided data for the validation of SOEC performance.
(Ebbesen et al., 2011; Sun et al., 2013)	Provided data for the validation of SOEC degradation.
(Saeidi et al., 2014; Todić et al., 2015)	Provided insights on ASF distribution theory and FTS reaction mechanisms
(Donnelly et al., 1988; Todic et al., 2013)	Gave insights on double ASF theory and growth probability of light hydrocarbons.
(Wei et al., 2017)	Provided data for model validation of CO_2-FTS process
(Fernández-Torres et al., 2022)	Provided information on CO_2-FTS process at industrial-scale.
(O'Brien et al., 2009)	Gave information on large-scale syngas production using SOEC rigs.
(Becker et al., 2012; Selvatico et al., 2016)	Provided insights on FTS and SOEC-FTS process simulations in Aspen Plus®.

3. Model development and model validation of SOEC during CO$_2$/H$_2$O co-electrolysis considering structural degradation[3]

3.1. Introduction

The degradation issue occurring within SOEC systems represents one of the main challenges hindering their applications at commercial-scale. Although up to 68.5% syngas production efficiency has been achieved, it was observed that the degradation of SOEC components was not accounted for in previous modelling and simulation studies. Therefore, this Chapter aims to develop and validate a SOEC model for CO$_2$/H$_2$O co-electrolysis considering the structural degradation of cathode, electrolyte and anode materials. Section 3.2 details the pseudo-dynamic model development of a planar SOEC operating under co-electrolysis. SOEC process simulation is elaborated in Section 3.3 and Section 3.4 discusses the validation of the pseudo-dynamic SOEC model.

3.2. 1-D pseudo-dynamic model development of planar SOEC for CO$_2$/H$_2$O co-electrolysis

3.2.1. Study of the CO$_2$/H$_2$O co-electrolysis process

CO$_2$ and H$_2$O streams enter a planar SOEC to produce syngas via co-electrolysis. Details on the co-electrolysis process are elaborated in Section 1.1.4.1.

3.2.2. Assumptions for model development

The 1-D pseudo-dynamic model of planar SOEC was developed under the following assumptions:

- SOEC model was divided into two sub-models: (1) The equilibrium voltage model calculating the minimum required voltage and (2) the degradation model simulating the overpotentials due to the structural deterioration of SOEC component materials.

---

[3] Most of this Chapter has been published in Kamkeng, A. D. N. and Wang, M. (2022) Long-term performance prediction of solid oxide electrolysis cell (SOEC) for CO$_2$/H$_2$O co-electrolysis considering structural degradation through modelling and simulation. Chemical Engineering Journal, 429, 132158

- The governing equations of the equilibrium voltage are generic for all SOEC systems operating under co-electrolysis mode. However, the modelling equations of the structural degradation are necessarily specific to the selected materials. Though any material can be susceptible to degradation, degradation mechanisms depend on the material composition (Yun Zheng et al., 2017). This study focused on the typical SOEC component materials: Ni-YSZ cathode, YSZ electrolyte and LSM-YSZ anode.

- SOEC operating voltage is represented by the sum of the equilibrium voltage and overpotentials resulting from structural degradation of SOEC components.

- SOEC model is a pseudo-dynamic model i.e. only the structural degradation of SOEC component materials was modelled dynamically whereas, the heat or mass accumulation within the cell was ignored.

- For theoretical simplicity, all degradation mechanisms due to particle diffusion are only along the X-axis whilst other dimensions were neglected.

- Other assumptions that are specific to each sub-model are given in their corresponding sections.

3.2.3. Model for SOEC equilibrium voltage

Also called open cell voltage, the equilibrium voltage (U_{EQ}) refers to as the minimum voltage applied to a SOEC system for the electrochemical reactions to take place (Moçoteguy et al., 2013). It is evaluated using the mixed potential theory because, at the triple phase boundary (TPB), more than one electrolysis reaction occurs. The mixed potential model is the combination of potentials resulting from H_2O and CO_2 co-electrolysis (Stempien et al., 2014). Furthermore, it considers the contribution of each electrochemical reaction based on the reactant coverage at the TPB (Equation 3.1).

$$U_{EQ} = \theta_{CO_2} \cdot U_{CO_2} + \theta_{H_2O} \cdot U_{H_2O} \tag{3.1}$$

$$U_{CO_2} = -\frac{\Delta G_{f,CO_2}}{n \cdot F} - \frac{RT}{n \cdot F} ln \left[\frac{x_{CO_2}}{x_{CO} \, x_{O_2}^{0.5}} \left(\frac{P}{P_{std}} \right)^{-0.5} \right] \tag{3.2}$$

$$U_{H_2O} = -\frac{\Delta G_{f,H_2O}}{n \cdot F} - \frac{RT}{n \cdot F} ln \left[\frac{x_{H_2O}}{x_{H_2} \, x_{O_2}^{0.5}} \left(\frac{P}{P_{std}} \right)^{-0.5} \right] \tag{3.3}$$

$$\theta_i = \frac{K_i \times x_i}{\sum_j K_j \, x_j} \tag{3.4}$$

$$K_i = K_i^0 exp\left(\frac{Q_i}{R \cdot T}\right) \qquad (3.5)$$

The standard chemical potential of CO_2 and H_2O electrolysis reactions was calculated using the Gibbs energy difference as expressed by Equations (3.2) and (3.3), respectively. To assess each reactant coverage (Equations 3.4 and 3.5), it was assumed that the adsorption of gaseous compounds on the electrode surface follows the modified Langmuir adsorption law in which the influence of empty sites on the equilibrium voltage is neglected (Moçoteguy et al., 2013; Stempien et al., 2014).

The concentration overpotential, due to the mass transport limitation of gaseous molecules, was not explicitly calculated in this work. However, its calculation depends on the reactant and product concentrations at the TPB (Ni, 2012b; Buttler et al., 2015) which were considered in the mixed potential theory as described by Equations (3.2) to (3.4). Therefore, the contribution of concentration overpotentials is implicitly expressed in the equilibrium voltage model.

3.2.4. Model for overpotentials from SOEC component degradation

3.2.4.1. Ni-YSZ degradation model

The degradation of Ni-YSZ cathode is essentially due to Ni particle growth at high temperatures through sintering. The sintering mechanism is commonly referred to as the re-organisation and loss of active surface area via condensation, evaporation and/or migration (Sehested et al., 2006; Yun Zheng et al., 2017). The increase in Ni particle size within the YSZ phase reduces the contact between Ni phases which affects both Ni-YSZ electronic conductivity and the TPB length (Faes et al., 2009). Ni-YSZ degradation model was developed under the following assumptions:

- The agglomeration of Ni particles occurs via the formation of Ni_2-OH complexes on Ni surface in the presence of H_2O (Sehested et al., 2006).

- All particles are spherical and randomly packed within the cathode electrode.

- The size of YSZ particle remains unchanged due to YSZ high melting temperatures (Yun Zheng et al., 2017).

Ni size evolution with time is evaluated based on the sintering model proposed by Sehested et al. (2006) and adapted in this study for Ni-YSZ composites as shown by Equations (3.6) and (3.7). Equation (3.7) is simply the integrated form of Equation (3.6). The volume of Ni particles

and the TPB length at the initial and after the time t of operation are described by Equations (3.8) and (3.9).

$$\frac{d(r_{Ni})}{dt} = C \frac{W_{Ni}}{W_{YSZ} \times A_{YSZ} \times r_{Ni}^6} \left(\frac{x_{H_2O}}{x_{H_2}^{0.5}}\right) exp\left(-\frac{E_{sin}}{R \cdot T}\right) \tag{3.6}$$

$$r_{Ni} = \left|r_{Ni,0}^7 + C' \frac{W_{Ni} \times t}{W_{YSZ} \times A_{YSZ}} \left(\frac{x_{H_2O}}{x_{H_2}^{0.5}}\right) exp\left(-\frac{E_{sin}}{R \cdot T}\right)\right|^{1/7} \tag{3.7}$$

$$t = 0; \quad V_0 = \frac{4}{3}\pi \cdot N_0 \cdot r_{Ni,0}^3 \text{ and } L_{TPB,0} = 2\pi \cdot N_0 \cdot r_{Ni,0} \tag{3.8}$$

$$\text{After time } t; V = \frac{4}{3}\pi \cdot N \cdot r_{Ni}^3 \text{ and } L_{TPB} = 2\pi \cdot N \cdot r_{Ni} \tag{3.9}$$

At constant density, the mass balance of Ni particles requires $V = V_0$. Hence,

$$N \cdot r_{Ni}^3 = N_0 \cdot r_{Ni,0}^3 \tag{3.10}$$

The TPB length change (Equation 3.11) resulting from the increase in Ni particle size was then obtained by combining Equations (3.8) to (3.10).

$$L_{TPB} = \frac{r_{Ni,0}^2}{r_{Ni}^2} \times L_{TPB,0} \tag{3.11}$$

The relationship between the polarisation voltage (representing the overpotential due to change in TPB) and current density is expressed by Equation (3.12) which is based on the high field approximation of the Butler-Volmer equation (Faes et al., 2009). Equation (3.13) was obtained after time differentiation of Equation (3.12) wherein the subscript I represents the cathode or anode electrode.

$$j = j_0 exp\left(\frac{\beta \cdot n \cdot F}{R \cdot T} \times U_{P,i}\right) \Rightarrow ln\left(\frac{j}{j_0}\right) = \frac{\beta \cdot n \cdot F}{R \cdot T} \times U_{P,i} \tag{3.12}$$

$$dln\left(\frac{j}{j_0}\right) = \frac{\beta \cdot n \cdot F}{R \cdot T} \times dU_{P,i} = \frac{\beta \cdot n \cdot F}{R \cdot T}\left(\frac{dU_{P,i}}{dt}\right) dt \tag{3.13}$$

$$ln\,(j) - ln\left(\frac{j_O}{j_{O,0}}\right) = \frac{\beta \cdot n \cdot F}{R \cdot T} \times U_{P,i}(t) \tag{3.14}$$

$$U_{P,i}(t) = \frac{R \cdot T}{\beta \cdot n \cdot F}\left[ln\,(j) - ln\left(\frac{L_{TPB}}{L_{TPB,0}}\right)\right] \tag{3.15}$$

The polarisation voltage as a function of current density and TPB length (Equation 3.15) was derived from the integration of Equation (3.13) considering that the TPB length is proportional to the exchange current density. Combining Equations (3.11) and (3.15) gives the polarisation voltage at the cathode electrode (Equation 3.16).

$$U_{P,Cat}(t) = \frac{R \cdot T}{\beta \cdot n \cdot F}\left[ln\,(j) - \, ln\left(\frac{r_{Ni,0}^2}{r_{Ni}^2}\right) \right] \tag{3.16}$$

The electronic conductivity of the Ni-YSZ composite is the combination of Ni and YSZ conductivities (Equation 3.17). However, the second term in Equation (3.17) was neglected since σ_{YSZ} is quite low compared to σ_{Ni} (Clemmer and Corbin, 2009).

$$\sigma_{Ni-YSZ} = V_{Ni} \cdot \sigma_{Ni} + V_{YSZ} \cdot \sigma_{YSZ} \tag{3.17}$$

Equations (3.18) to (3.21) express Ni effective conductivity based on the percolation theory which describes the connectivity of particles within a network structure and its effects on the system physical properties (Wu and McLachlan, 1997; Chen et al., 2009). Ohm's law was then used to evaluate the ohmic overpotential on the cathode side as shown by Equation (3.22).

$$\sigma_{Ni} = \sigma_{Ni,0}\left(\frac{V_{Ni} - V_{Ni}^c}{1 - \Phi/(1+\Phi) - V_{Ni}^c} \right)^2 \tag{3.18}$$

$$\sigma_{Ni,0} = 3.27 \times 10^4 - 10.65 \times T \tag{3.19}$$

$$Z\,\frac{V_{Ni}^c/r_{Ni}}{V_{Ni}^c/r_{Ni} + (1 - V_{Ni}^c)/r_{YSZ}} = 1.764 \tag{3.20}$$

$$Z = Z_{YSZ,YSZ}\,\frac{V_{Ni}/r_{Ni} + V_{YSZ}/r_{YSZ}}{V_{YSZ}/r_{YSZ}} \tag{3.21}$$

$$U_{S,Cat}(t) = \frac{d_{Ni-YSZ}}{\sigma_{Ni-YSZ}} \times j \tag{3.22}$$

3.2.4.2. YSZ degradation model

The degradation of YSZ electrolyte is caused by the gradual phase transformation of YSZ crystal structure from cubic to tetragonal at high temperatures and under reducing environments. The phase transformation is mostly due to cation diffusion which results in a decrease in YSZ ionic conductivity (Hattori et al., 2004; Zhu and Lin, 2018). The evolution of YSZ conductivity with operating time was calculated using Equations (3.23) and (3.25) based on YSZ structure stability dopant radius (Jiang and Wachsman, 1999).

$$\sigma_{El}(t) = \sigma_{El,0}\left[\lambda + (1-\lambda)exp\left(-\frac{t}{\tau}\right)\right] \tag{3.23}$$

$$\tau = 7.23 \times 10^{-38} exp\left(89.8 \times r_{Y^{3+}}\right) \tag{3.24}$$

$$\sigma_{El,0} = \frac{\sigma_{El}^0}{T} exp\left(-\frac{E_{a,El}}{R \cdot T}\right) \tag{3.25}$$

The ohmic overpotential in the electrolyte was then evaluated according to Ohm's law as expressed by Equation (3.26).

$$U_{S,El}(t) = \frac{d_{El}}{\sigma_{El}(t)} \times j \tag{3.26}$$

3.2.4.3. LSM-YSZ degradation model

Several factors are responsible for the degradation of LSM-YSZ anode among which the formation of secondary phases and LSM-YSZ phase coarsening are widely considered as the two primary causes of LSM-YSZ material degradation (Moçoteguy and Brisse, 2013; Farlenkov et al., 2015; Yun Zheng et al., 2017).

(a) Formation of secondary phases

Secondary layers originate from two main mechanisms. At the interface between LSM-YSZ and YSZ electrolyte, oxygen ions are oxidized to form gaseous oxygen (Reaction 1.3). This creates high O_2 partial pressures near the LSM-YSZ interface and favours the formation of $La_2Zr_2O_7$ (LZO) due to ZrO_2 from YSZ reaction with $LaMnO_3$ from LSM as described by Reaction 3.27 (Keane et al., 2012).

$$0.25O_2 + ZrO_2 + LaMnO_3 \rightleftharpoons 0.5La_2Zr_2O_7 + MnO_2 \tag{3.27}$$

$$2Cr^0 + 1.5O_2 \rightleftharpoons Cr_2O_{3(s)} \tag{3.28}$$

Due to their low cost, good electrical conductivity and easy availability, Fe-Cr alloys (for instance, Crofer 22APU and Haynes 230) are preferred interconnect materials used to connect the anode of a single cell to the cathode of the adjoining cell to form a SOEC stack. Nevertheless, at high operating temperatures and the interface between the anode and the interconnect, there is chromium oxide scale (COS) formation owing to oxidation of Cr compounds by gaseous O_2 as shown by Reaction 3.28 (Larrain et al., 2006; Moçoteguy and Brisse, 2013).

To develop the model for the formation of secondary layers, the following were considered:

- The formation of the LZO layer is due to Mn^{2+} diffusion from LSM to YSZ and subsequent diffusion of La^{3+} and Zr^{4+} towards the anode-electrolyte interface (Mitterdorfer and Gauckler, 1998).

- COS is a single-phase layer and represented by Cr_2O_3. Cr_2O_3 formation takes place via Cr^{3+} and O^{2-} diffusion (Larrain et al., 2006).

Wagner's law for parabolic oxidation was then used to evaluate the thickness of secondary layers with time (Equations 3.29 and 3.30) in which the subscript I represents LZO or COS layer. The ohmic overpotential on the anode side resulting from LZO and COS formation was calculated using Equations 3.31 to 3.33 (Larrain et al., 2006).

$$d_i^2(t) = \left(K_{P,i} \times t\right) exp\left(-\frac{E_i}{R \cdot T}\right) \tag{3.29}$$

$$K_{P,i} = \frac{K_{g,i}}{\left(X_{O,i} \times \rho_i\right)^2} \tag{3.30}$$

$$U_{S,An}(t) = (R_{COS} + R_{LZO}) \times j \tag{3.31}$$

$$R_i = \frac{d_i(t)}{\sigma_i} \tag{3.32}$$

$$\sigma_i = \frac{\sigma_i^0}{T} exp\left(-\frac{E_{a,i}}{R \cdot T}\right) \tag{3.33}$$

(b) LSM-YSZ phase coarsening

At high temperatures and with increasing operating time, the microstructures of the anode electrode (particularly near the anode/electrolyte interface) become denser and coarser due to particle diffusion towards the anode interface. The change in particle phase distribution will affect the TPB length on the anode side (Liu et al., 2012; Ananyev et al., 2018). The following assumptions were considered to develop LSM-YSZ degradation model due to particle coarsening:

- LSM-YSZ degradation only results from LSM phase coarsening. This is because experimental results demonstrated that YSZ phase coarsening does not significantly evolve at high temperatures (Liu et al., 2012; Ananyev et al., 2018).

- LSM phase coarsening is caused by the diffusion of Mn^{2+} particles LSM surface towards the anode interface to reach TPB active sites (Farlenkov et al., 2015).

Fick's second law of diffusion was used to describe the mass transport of diffused particles in one dimension as indicated by Equation (3.34) wherein the TPB length represents the concentration of diffused particles. Equation (3.35) is the solution to Equation (3.34) obtained when the surface concentration is zero hence, $x = 0$ and $L_{TPB} = L_{TPB,0}$ (Crank, 1975; Farlenkov et al., 2015).

$$\frac{\partial}{\partial t} L_{TPB} = D_{LSM} \times \frac{\partial^2}{\partial x^2} L_{TPB} \tag{3.34}$$

$$\left(D_{LSM} \frac{d}{dx} L_{TPB} \right)_{x=0} = \frac{L_{TPB,0} \times D_{LSM}}{\sqrt{\pi \cdot t \times D_{LSM}}} \tag{3.35}$$

$$\frac{L_{TPB}}{L_{TPB,0}} = 1 - 2 \times \left(\frac{t \times D_{LSM}}{\pi} \right)^{1/2} \tag{3.36}$$

$$U_{P,An}(t) = \frac{R \cdot T}{\beta \cdot n \cdot F} \left[ln\,(j) - ln \left| 1 - 2 \times \left(\frac{t \times D_{LSM}}{\pi} \right)^{1/2} \right| \right] \tag{3.37}$$

The change in TPB length with time was then calculated using Equation (3.36) which was obtained by integrating Equation (3.35). The polarisation voltage on the anode side (Equation 3.37) was then obtained by combining Equations (3.15) and (3.36). Finally, SOEC operating voltage, which represents the total required voltage applied to SOEC was calculated using Equation (3.38).

$$U(t) = U_{EQ} + \sum \left[U_{P,i}(t) + U_{S,i}(t) \right] \tag{3.38}$$

3.3. SOEC model implementation

The implementation of SOEC model was carried out in Aspen Plus® software. Aspen Plus® Library does not have a built-in block to simulate a SOEC rig. Therefore, available blocks in Aspen Plus® Library were combined to represent the SOEC unit and Fortran® routines were implemented for the structural degradation model. Peng-Robinson was chosen as the property method for SOEC process simulation. This is because it provides more reliable results for non-polar compounds including H_2, CO_2, and CH_4. Furthermore, the Peng-Robinson physical property has been successfully used in previous modelling and simulation studies on SOEC (Stempien et al., 2015; Khesa and Mulopo., 2021).

The SOEC unit flowsheet developed in this study is illustrated in Figure 3.1. The feed gases first go to a Gibbs reactor block (PRE-ELEC) wherein they reach equilibrium based on the RWGS reaction as described by Reaction (3.39). A separator block (CAT-SEP) then removes

the reactant gases (CO_2 and H_2O) from other gases and the resulting stream (CO_2-H_2O) is sent to a stoichiometry reactor block (ELEC). CO_2 and H_2O co-electrolysis reactions take place in the stoichiometry reactor block (ELEC) following Reactions (1.5) and (1.6). Fortran® routines assess the reactant conversion (Equation 3.40), which was calculated based on Faraday's law, and the required SOEC operating voltage. Table 3.1 summarises SOEC modelling equations that were implemented in Aspen Plus®.
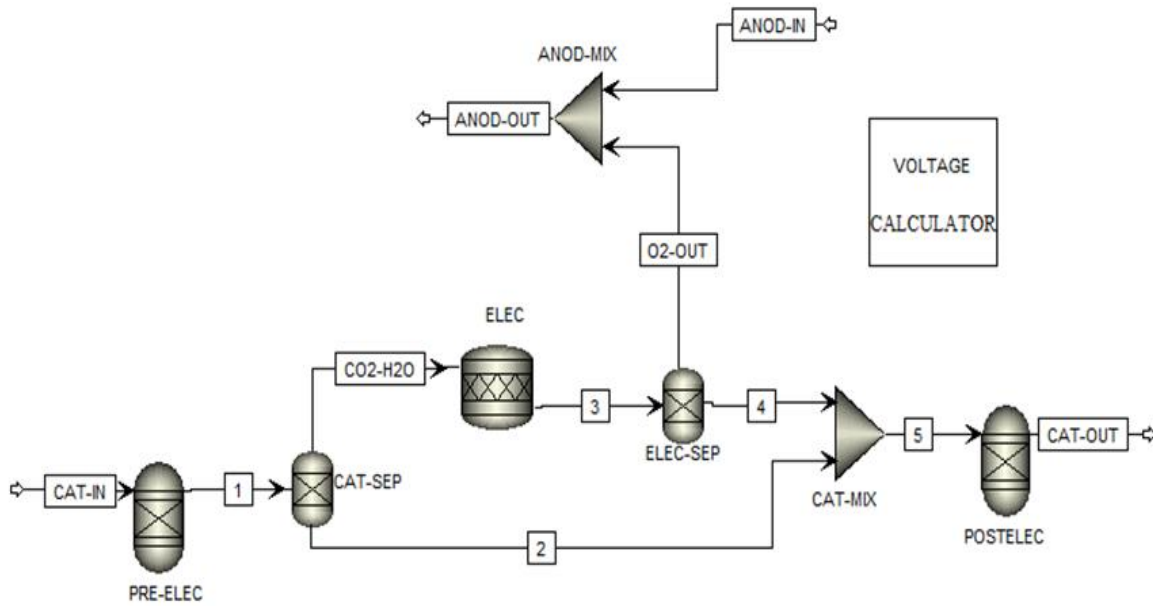
Figure 3.1: SOEC process flowsheet in Aspen Plus®

$$CO_2 + H_2 \rightleftharpoons H_2O + CO \qquad (3.39)$$
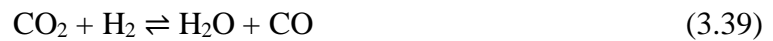
$$X_R = \frac{I}{n \times F \times \dot{N}_{in}} = \frac{A_{cell} \times N_{cell} \times j}{n \times F \times \dot{N}_{in}} \qquad (3.40)$$

Table 3.1: Summary of SOEC modelling equations

Parameter	Equation
Equilibrium voltage	
Adsorption constant	Equation (3.5)
Surface coverage fraction	Equation (3.4)
Standard chemical potential of H_2O and CO_2 electrolysis	Equations (3.2) and (3.3)
Equilibrium voltage	Equation (3.1)
Overpotential from cathode degradation	

Ni radius	Equation (3.7)
Polarisation voltage at the cathode	Equation (3.16)
Intrinsic Ni conductivity	Equation (3.19)
Average coordination number	Equation (3.21)
Ni volume fraction at percolation	Equation (3.20)
Ni effective conductivity	Equation (3.18)
Ni-YSZ conductivity	Equation (3.17)
Ohmic voltage at the cathode	Equation (3.22)
Overpotential from electrolyte degradation	
Time constant	Equation (3.24)
Intrinsic YSZ conductivity	Equation (3.25)
YSZ ionic conductivity	Equation (3.23)
Ohmic voltage at the electrode	Equation (3.20)
Overpotential from anode degradation	
Conductivity of secondary layers	Equation (3.31)
Thickness of secondary layers	Equation (3.29)
Ohmic resistance	Equation (3.32)
Ohmic voltage at the anode	Equation (3.31)
Polarisation voltage at the anode	Equation (3.37)
Reactant conversion	Equation (3.40)
SOEC operating voltage	Equation (3.38)

The stream 3 leaving the stoichiometry block (ELEC) also goes through a separation stage in which oxygen is removed from other gases. This step was required to account for the fact that in reality, syngas and oxygen are synthesized in different compartments. Finally, cathodic flows (Streams 2 and 4) are combined and sent to a second Gibbs reactor block (POSTELEC) wherein the gas mixture reaches equilibrium based on both methanation (or steam methane reforming) and RWGS (Reactions 3.41 and 3.39 respectively).

$$H_2O + CH_4 \rightleftharpoons CO + 3H_2 \tag{3.41}$$

The assumptions of methanation and RWGS reactions taking place before and after the electrochemical reactions are based on kinetic values obtained in the presence of Ni and at high operating temperatures (Sun et al., 2013; Cinti et al., 2016). At the anode electrode, the oxygen stream exiting the separator block (ELEC-SEP) is mixed with a sweep air stream. Though SOEC can efficiently operate without a sweep gas and thus, produce pure oxygen on the anode side, considerable technical challenges arise from storing and handling pure O_2 at high temperatures (Samavati et al., 2018).

3.4. SOEC model validation

SOEC model validation was performed using experimental data from the literature. Data from two sets of experiments were chosen to numerically validate SOEC performance and structural degradation of SOEC components. Throughout this section, single cells are made of Ni-YSZ/YSZ/LSM-YSZ material in which YSZ contains 8.0 mol% of Y_2O_3 and LSM composition is $(La_{0.75}Sr_{0.25})_{0.95}MnO_3$. The interconnect material is Crofer 22 APU stainless steel which contains 20–24 wt.% Cr. During all experiments, hydrogen was added to the inlet feed gas to prevent Ni oxidation on the cathode side whereas, a continuous O_2 and/or air stream was supplied to prevent LSM-YSZ change of state at the anode electrode.

3.4.1. Validation of SOEC performance

SOEC performance validation was carried out using experiments from the FuelCell Lab at the University of Perugia by Cinti et al. (2016). SOEC stack consists of four planar cells supplied by Forschungszentrum Jülich. Further details on the experimental SOEC rig are provided in Section 2.1.1 (Table 2.1). Three experimental tests were conducted to assess the influence of the feed gas composition on SOEC performance in CO_2 and H_2O co-electrolysis mode. The experimental conditions and SOEC parameters are given in Table 3.2.

Table 3.2: Experimental conditions and SOEC parameters from FuelCell Lab. Data taken from (Cinti, et al., 2016)

Parameter	Test 1	Test 2	Test 3
Composition of cathode feed: $CO_2/H_2O/H_2$ (%mol)	20/70/10	30/60/10	40/50/10
Cathode flowrate (mol/hr)	8.53		
Cathode thickness (μm)	7 – 10		
Anode flowrate (mol/hr)	8.92		

Anode thickness (μm)	10 – 15
Electrolyte thickness (μm)	8 – 10
SOEC operating pressure (bar)	1.0
SOEC Operating temperature (℃)	750
Number of cells	4
Cell size (cm^2)	10×10
Active cell area (cm^2)	80

Model validation results for SOEC performance are given in terms of mole fractions of outlet components CO_2, H_2 and CO. Figure 3.2. illustrates model predictions and experimental values of syngas outlet composition as a function of the current density for different feed gas compositions. The results were obtained by simulating the SOEC model under the operating conditions given in Table 3.2. Since experimental data are provided on a dry basis, the cathode outlet stream (CAT-OUT in Figure 3.1) was cooled down to roughly ambient conditions and water was removed from the stream using a two-phase outlet flash drum.
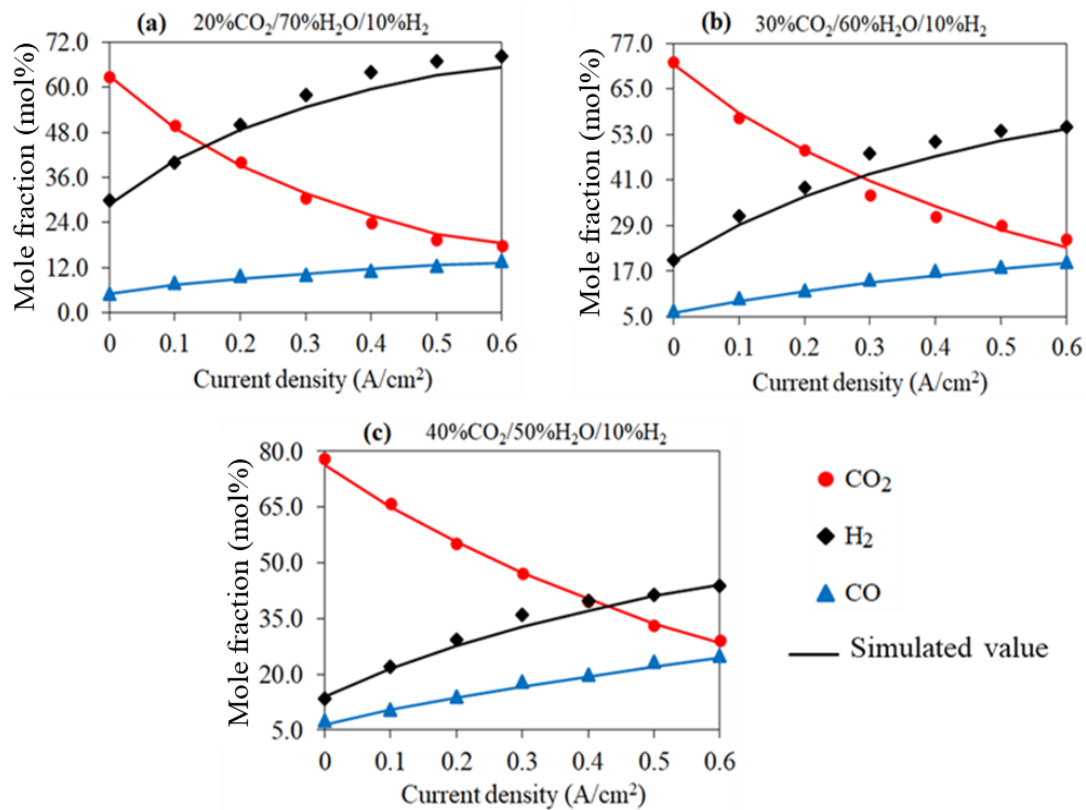
Figure 3.2: Model predictions of outlet syngas composition (solid lines) compared Experimental values (symbols) for (a) Test 1, (b) Test 2 and (c) Test 3

The developed SOEC model gives a fairly good prediction of syngas composition profiles despite some discrepancies (Figure 3.2). The relative error (RE) between model predictions and experimental values were calculated using Equation (3.42). The highest relative errors observed for each test at different current densities are detailed in Table 3.3. The highest relative error of 13.4% was found for H_2 compound at 0.3 A/cm^2 current density of Test 2 (Figure 3.2b).

$$RE(i) = \frac{|V_{exp,i} - V_{sim,i}|}{V_{exp,i}} \times 100 \tag{3.42}$$

Table 3.3: Highest relative errors observed during SOEC performance validation

Current density (A/cm^2)	Relative errors (%)		
	Test 1	Test 2	Test 3
0.0	4.0	7.7	6.8
0.1	8.8	9.0	3.2
0.2	7.1	6.2	5.1
0.3	5.5	13.4	8.9
0.4	7.9	7.5	6.3
0.5	7.2	4.8	5.5
0.6	4.3	8.6	2.6

A possible explanation for these differences could be how syngas composition is obtained. Indeed, the syngas composition is obtained from experiments using gas chromatography (Cinti, et al., 2016) which requires dry samples (hence, H_2O mol% = 0). Although water was removed from the cathode outlet stream using a flash drum block, some H_2O mole fraction (~2.9 mol%) remains in the resulting stream which might affect the outlet syngas composition obtained in this work.

3.4.2. Validation of SOEC degradation

The 1-D pseudo-dynamic model for SOEC structural degradation was validated using data from experiments performed at DTU Energy Conversion (formerly called Risø DTU) in Denmark by Ebbesen et al. (2011) and Sun et al. (2013). Two SOEC stacks, including 10-cell and 2-cell planar stacks, were produced at DTU Energy Conversion. Further descriptions of the SOEC stacks are also given in Section 2.1.1 (Table 2.1). Two experiments were carried out

to investigate the effects of low and high current densities on SOEC degradation and durability under co-electrolysis mode.

Initial experiments were performed using the 10-cell SOEC stack at a current density of 0.5 A/cm^2 for 800 hours after which, the current density was increased to 0.75 A/cm^2 for another 350 hours. To maintain a reactant conversion of 60%, the inlet gas flowrate at the cathode electrode was increased from 360 L/hr at 0.5 A/cm^2 to 540 L/hr at 0.75 A/cm^2. The second experiment was conducted using the 2-cell SOEC stack at a current density of 1.0 A/cm^2 for approximately 1000 hours. Table 3.4 provides characteristics and experimental conditions of both SOEC stacks in which Test 1 and Test 2 represent experiments carried out using the 10-cell and 2-cell planar SOEC stacks, respectively.

Table 3.4: Experimental conditions and SOEC characteristics from DTU Energy Conversion. Data taken from Ebbesen et al. (2011) and Sun et al. (2013)

Parameter	Test 1	Test 2
Cathode feed gas composition: $CO_2/H_2O/H_2$ (%mol)	45/45/10	45/45/10
Cathode flowrate (L/hr)	360/540	25
Cathode thickness (µm)	10	10
Cathode porosity (%)	40	40
Volume Fraction (Ni/YSZ)	40/60	40/60
Ni initial radius (µm)	4.5	4.5
YSZ initial radius (µm)	4	4
YSZ surface area (m^2/g)	0.41	0.41
Anode feed composition: O_2 (%mol)	100	100
Anode flowrate (L/hr)	60	50
Anode thickness (µm)	20	20
Anode porosity (%)	35	35
Volume Fraction (LSM/YSZ)	50/50	50/50
Electrolyte thickness (µm)	12	12
SOEC Operating pressure (bar)	1.0	1.0
SOEC Operating temperature (℃)	850	800

Current density (A/cm^2)	0.5/0.75	1.0
Number of cells	10	2
Cell size (cm^2)	12 × 12	5 × 5
Active cell area (cm^2)	92.16	16

Model validation results for SOEC structural degradation are presented in terms of operating voltage as a function of operating time. The results were obtained by simulating the pseudo-dynamic SOEC model under the conditions presented in Table 3.4. However, not all required data were available from Ebbesen et al. (2011) and Sun et al. (2013). Therefore, the remaining parameters were assumed within realistic ranges based on available literature as summarized in Table 3.5.

Table 3.5: Parameters used for model validation of SOEC structural degradation

Parameter	Value	Reference
CO_2 adsorption constant	2.27	(Stempien et al., 2014)
H_2O adsorption constant	9.25	
CO_2 enthalpy of adsorption (J/mol)	18,828	
H_2O enthalpy of adsorption (J/mol)	13200	
Activation energy for sintering (J/mol)	332,000	(Sehested et al., 2004)
Coordination number of YSZ material	6	(Chen et al., 2009)
Electrolyte pre-exponential factor (S/cm)	360,000	(Menon et al., 2015)
Electrolyte activation energy (J/mol)	80,000	
Ionic radius (Å)	1.01	(Jiang and Wachsman, 1999)
LSM surface diffusion (cm^2/hr)	1.12×10^{-5}	(Farlenkov et al., 2015)
LZO density (g/cm^3)	6.05	(Li et al., 2017)
Weight gain rate for LZO growth (g^2/cm^4.hr)	4.43×10^{-2}	
Activation energy for LZO growth (J/mol)	206,273	
LZO pre-exponential factor (S/cm)	225.49	
LZO activation energy (J/mol)	55,000	

COS density (g/cm^3)	5.255	
Weight gain rate for COS growth: Test 1/Test 2 (g^2/cm^4.hr)	6.84×10^{-10} / 2.40×10^{-09}	(Larrain et al., 2006; Palcut et al., 2012)
Activation energy for COS growth (J/mol)	220,000	
COS pre-exponential factor (S/cm)	320,000	
COS activation energy (J/mol)	86,200	

Figures 3.3a and 3.3b depict model predictions and experimental values for SOEC operating voltage as a function of operating time for Test 1 and Test 2, respectively. The relative errors between model predictions and experimental values were also calculated and they are presented in Table 3.6. Good agreements between experimental data and model predictions were found with relative errors below 1.0%. The results presented in this section demonstrate that the 1-D pseudo-dynamic SOEC model developed in Aspen Plus$^®$ using Fortran$^®$ routines can reasonably predict both SOEC outlet syngas composition and structural degradation at different input conditions. Therefore, the SOEC model is deemed suitable for further parametric analysis.
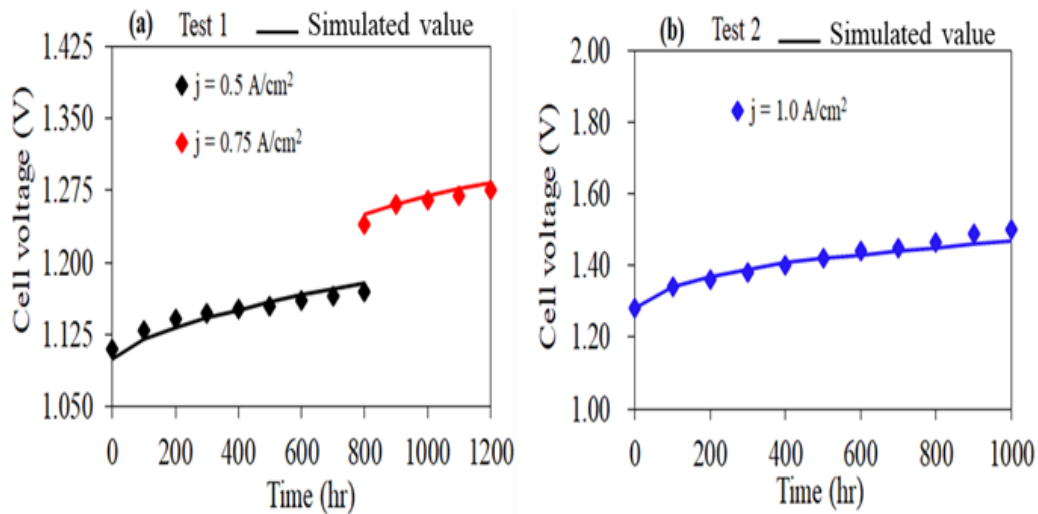
Figure 3.3: Model predictions (solid lines) of SOEC degradation compared to experimental values (symbols) for different current densities

Table 3.6: Comparison of SOEC degradation values between model predictions and experimental data from DTU Energy Conversion

Time (hr)	Data from DTU (V)	Aspen Plus® simulation (V)	Relative error (%)
0	1.11	1.10	0.90
200	1.14	1.13	0.79
400	1.15	1.15	0.17
600	1.16	1.17	0.52
800	1.24	1.25	0.81
1,000	1.26	1.27	0.40
1,200	1.27	1.28	0.63

3.5. Conclusion

This Chapter presented the methodology for the development of a 1-D pseudo-dynamic model of SOEC operating under CO_2 and H_2O co-electrolysis mode. The modelling equations for SOEC equilibrium voltage and structural degradation of a typical SOEC component materials (Ni-YSZ cathode, YSZ electrolyte and LSM-YSZ anode) were described. The proposed model is based on first principles and incorporates electrochemical/chemical reactions, mass balance and particle diffusion/transport.

The pseudo-dynamic model was then implemented in Aspen Plus® using Fortran® routines. Finally, model validation of both SOEC performance (syngas outlet composition) and structural degradation (operating voltage as a function of time) was carried out for different operating conditions including current densities, feed gas compositions and inlet flowrates.

The comparison between model predictions and experimental data, collected from FuelCell Lab (Cinti et al., 2016) and DTU Energy conversion (Ebbesen et al., 2011; Sun et al., 2013), indicated that relative errors for the outlet syngas composition were below 13.5% whereas, that of SOEC degradation were just under 1.0%. The small dissimilarities observed for the outlet syngas composition could be due to the remaining water content (roughly 2.9 mol%) found in the cathode outlet stream. Therefore, the developed pseudo-dynamic model was deemed accurate enough for further parametric analysis on SOEC performance and degradation.

4. Long-term performance analysis of SOEC for syngas production through CO_2/H_2O co-electrolysis[4]

4.1. Introduction

Previous studies on SOEC optimisation and process analysis did not consider the degradation of SOEC component materials. Understanding that cell degradation is one of the most noteworthy issues affecting CO_2/H_2O co-electrolysis, it is important to understand the factors causing the structural damages of SOEC components with time to find effective strategies to reduce SOEC degradation and improve SOEC long-term performance. Therefore, this chapter focuses on SOEC process analysis during long-term operation using the 1-D pseudo-dynamic model previously developed and validated in Aspen Plus® software (Chapter 3).

Section 4.2 presents the assumptions and settings considered to carry out SOEC long-term performance analysis. The effects of operating conditions and structural degradation on SOEC long-term performance are analysed in Sections 4.3 and 4.4. Section 4.5 discusses novel design materials for the optimisation of SOEC long-term performance during CO_2 and H_2O co-electrolysis.

4.2. Assumptions and evaluation criteria for SOEC long-term performance analysis

To carry out SOEC long-term performance analysis, the following assumptions were made:

- SOEC performance analysis was performed for 20,000 hours of operation which corresponds to the minimum desired lifetime of SOEC stacks for commercial applications (Sohal et al., 2012).

- The SOEC performance is expressed in terms of syngas production efficiency and SOEC average degradation rate.

---

[4] Most of this Chapter has been published in Kamkeng, A. D. N. and Wang, M. (2022) Long-term performance prediction of solid oxide electrolysis cell (SOEC) for CO_2/H_2O co-electrolysis considering structural degradation through modelling and simulation. Chemical Engineering Journal, 429, 132158

- Equation (4.1) was used to calculate the average degradation rate (Lang et al., 2019).

$$\Delta U = \frac{U(t) - U(t_0)}{(t - t_0) \times U(t_0)} \times 100\% \qquad (4.1)$$

$$\eta_{syngas} = \frac{HHV_{out}}{\mathcal{P}_{cell} + HHV_{in}} \qquad (4.2)$$

$$\mathcal{P}_{cell} = U(t) \times j \times A_{cell} \qquad (4.3)$$

- Syngas production efficiency is the same as defined as Section 2.4.1 and was calculated using Equations (4.2) and (4.3) wherein SOEC required power and the higher heating values of the inlet gases and produced syngas are accounted for (Becker et al., 2012; Lang et al., 2019). It was assumed that the influence of the steam methane reforming/methanation (Reaction 3.41) is negligible. Hence, the required cell voltage and power are a function of energy demands for the electrochemical reactions (Herz et al., 2018).

- Long-term performance analysis was carried out only for the SOEC unit (Figure 3.1) i.e. the net power requirement of the reactant pre-treatment (for example, net duty of heaters and network of compressors and pumps/valves) was not considered in this section. However, they were included while studying the integrated SOEC-FTS process for gasoline synthesis.

- Given the current maturity of SOEC systems, 10% heat losses were considered during calculations of the syngas production efficiency (Lang et al., 2019).

- The effect of SOEC operating pressure was not studied. This is because previous studies, both experimental (Riedel et al., 2020) and modelling/simulation (Chen et al., 2017), have demonstrated that increasing SOEC operating pressure significantly promotes methane synthesis at high voltages and in the presence of Ni. Since the lowest conversion ratio to methane was found at 1.0 bar during CO_2/H_2O co-electrolysis (Chen et al., 2017), SOEC operating pressure was kept at 1.0 bar throughout the long-term performance analysis.

4.3. Effects of operating conditions on SOEC long-term performance

The effects of operating conditions on SOEC long-term performance were studied following the process analysis concept wherein only the analysed parameter varies while the others remain unchanged (Varrone et al., 2018). The operating conditions analysed include the current

density, temperature, feed gas composition and cathode inlet flowrate. For each operating condition, the studied range is provided in its corresponding section.

4.3.1. Effect of current density on SOEC degradation and syngas efficiency

4.3.1.1. Justification and set-up for this case study

According to Faraday's law of electrolysis, the reactant conversion rate is directly proportional to the current density (Equation 3.40). As a result, the current density is a key parameter for achieving high CO_2/H_2O co-electrolysis rates and syngas production. Furthermore, a good understanding of its effect on SOEC degradation during long-term operation could help to assess which current density provides a high syngas production rate with a minimum SOEC degradation rate.

To study the effects of current density on SOEC long-term performance, the pseudo-dynamic SOEC model was simulated in Aspen Plus® under the following operating conditions:

- Temperature: 800°C, cathode inlet flowrate: 360 L/hr and feed gas composition (in mole%): 45%CO_2/45%H_2O/10%H_2.

- SOEC characteristics and remaining parameters were the same as presented in Tables 3.4 and 3.5.

- The current densities of 0.5, 1.0 and 1.5 A/cm^2 were chosen so as to investigate the effects of low and high current densities on SOEC long-term performance.

4.3.1.2. Results and discussion

The effects of current density on SOEC required voltage and syngas production efficiency are illustrated in Figure 4.1. As previously shown in Figure 3.2 (see Section 3.4.1), the increase in current density leads to higher syngas production due to higher reactant conversion as per Faraday's law (Equation 3.40). However, considering structural degradation of SOEC components, it was observed that the syngas production efficiency decreases faster at higher current densities.

Indeed, at a current density of 0.5 A/cm^2, syngas production efficiency is roughly 48.6% after 20,000 hours of operation. Whereas, at 1.0 and 1.5 A/cm^2, syngas production efficiency decreases from 53.5 to 41.3% and 51.7 to 36.4%, respectively after 20,000 hours of operation. This was due to the increase in SOEC required voltage (thus, higher power utilisation) from

1.24 to 2.05 V at 1.0 A/cm² and 1.33 to 2.53 V at 1.5 A/cm² with an average degradation rate of 3.3 and 4.5 %/1000hrs, respectively.
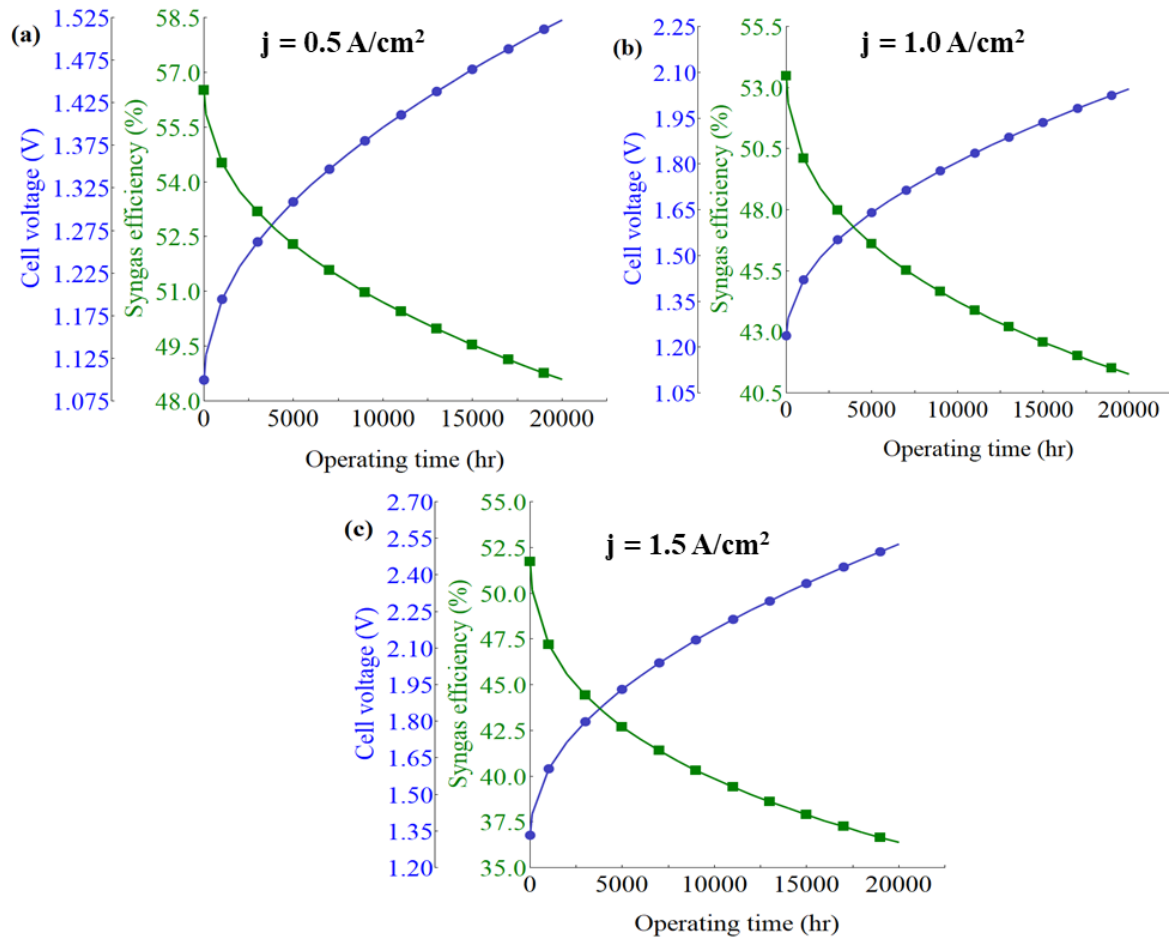
Figure 4.1: SOEC long-term performance for different current densities: (a) j = 0.5 A/cm², (b) j = 1.0 A/cm² and (c) j = 1.5 A/cm²

The results presented above are in good agreement with experimental findings using Ni-YSZ/YSZ/LSM-YSZ SOEC configuration for CO_2/H_2O co-electrolysis at low (Graves et al., 2011) and high (Sun et al., 2013) current densities. In both studies, the analysis of impedance measurements revealed that at higher current densities, long-term SOEC degradation is related to the increase in both polarisation and ohmic resistance indicating the structural deterioration of both electrodes and electrolyte materials. Furthermore, Equation (3.15) for the polarisation voltage and Equations (3.22), (3.26) and (3.31) for the ohmic overpotentials at the cathode, electrolyte and anode are directly proportional to the applied current density. This further explains the increase in the required voltage at higher current density hence, lower syngas efficiency. Therefore, long-term SOEC performance needs to be enhanced at high current densities.

4.3.2. Effect of temperature on SOEC degradation and syngas efficiency

4.3.2.1. Justification and set-up for this case study

Operating temperature plays an important role during feed gas adsorption on electrode surfaces, electrochemical/chemical reactions and mass transfer within SOEC (Yun Zheng et al., 2017). Moreover, high operating temperatures of SOECs compared to other electrolysers offer the possibility to overcome CO_2 thermodynamic stability through direct CO_2 electrolysis or simultaneous CO_2 and H_2O co-electrolysis (Stempien et al., 2013a). However, such high-temperature operations will also affect SOEC performance and material durability. Hence, it is paramount to assess the relationship between the operating temperature and SOEC long-term performance.

To study the effects of operating temperature on SOEC long-term performance, the pseudo-dynamic SOEC model was simulated in Aspen Plus® under the following operating conditions:

- Two operating temperatures were considered: 750 and 850℃ for two current densities including 1.0 and 1.5 A/cm². This set-up was chosen to investigate the effects of lower and higher temperatures at high current densities.

- The feed gas composition and cathode inlet flowrate remained the same as in Section 4.3.1

- SOEC characteristics and remaining parameters were the same as detailed in Tables 3.4 and 3.5.

4.3.2.2. Results and discussion
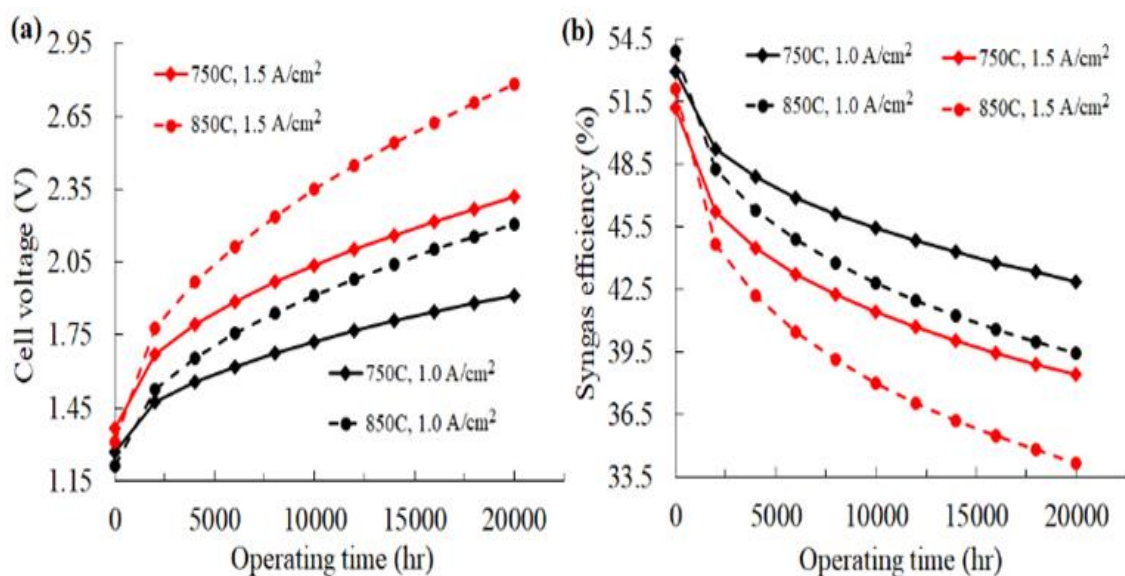
Figure 4.2: Long-term analysis of (a) SOEC required voltage and (b) syngas production efficiency for different operating temperatures at high current densities

Figure 4.2 depicts the evolution of SOEC required voltage (Figure 4.2a) and syngas production efficiency (Figure 4.2b) for different operating temperatures at high current densities. The results indicated that increasing SOEC operating temperature from 750 to 850℃ leads to a decrease in the equilibrium voltage from 1.27 to 1.21 V at 1.0 A/cm^2 and 1.36 to 1.31 V at 1.5 A/cm^2. This was due to the thermodynamics of CO_2 and H_2O co-electrolysis at high operating temperatures as illustrated in Figure 4.3.
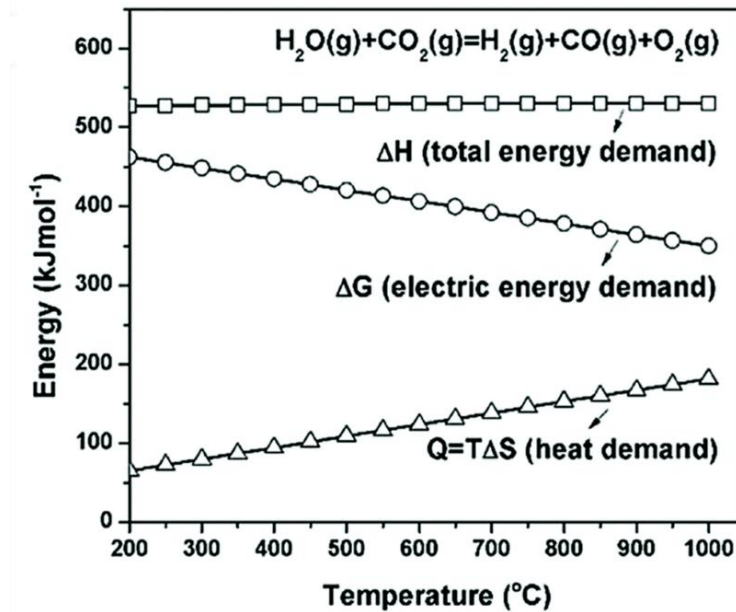
Figure 4.3: Relationship between energy demands of CO_2 and H_2O co-electrolysis reactions (Yun Zheng et al., 2017)

$$\Delta G = \Delta H - (T \cdot \Delta S) \qquad (4.4)$$

To elaborate, the Gibbs free energy change (ΔG), also called electrical energy demand, of the co-electrolysis reductions of CO_2 and H_2O is a function of temperature as shown in Equation (4.4) in which ΔH and $T \cdot \Delta S$ represent respectively the total energy and heat demands (Yun Zheng et al., 2017). Although the total energy demand remains almost constant with increasing temperatures, the increase in heat demand (due to positive ΔS) leads to lower electrical energy demand (Figure 4.3) thus, lower equilibrium voltage. Furthermore, the co-electrolysis reactions are also enhanced at higher SOEC temperatures resulting in increased CO_2 and H_2O conversions (Menon et al., 2015). This would explain why the initial syngas production efficiency also increases from 53.0 to 53.9% at 1.0 A/cm^2 and 51.2 to 52.3% at 1.5 A/cm^2 (Figure 4.2b).

The analysis of Figure 4.2 also revealed that SOEC required voltage and syngas production efficiency respectively increases and decreases faster with increasing operating temperatures

during long-term operation. For example, at the current density of 1.0 A/cm^2, the syngas production efficiency decreases from 54.0 to 39.4% at 850℃ and 53.0 to 43.0% at 750℃ caused by the rapid increase in cell voltage from 1.21 to 2.21 V at 850℃ compared to 1.27 to 1.91 V at 750℃ after 20,000 hours of operation. SOEC average degradation rate was 4.1 %/1000hrs at 850℃ and 1.0 A/cm^2 which was roughly 1.6 times higher than the average degradation rate at 750℃.

Similar trends were observed at 1.5 A/cm^2 current density, with an average degradation rate of 4.3 and 6.1 %/1000hrs at 750 and 850℃, respectively after 20,000 hours of operation. The faster degradation rates observed at higher temperatures are related to the direct dependence of the structural degradation on SOEC operating temperature. As shown by Equations (3.7) and (3.29), an increase in temperature would enhance Ni particle growth at the cathode electrode and the formation of secondary phases on the anode side which would result in higher ohmic and polarisation overpotentials hence, higher required voltage and lower syngas production efficiency.

Though higher operating temperatures would initially lead to higher syngas production efficiency, operating SOECs at lower temperatures seem more beneficial for long-term performance.

4.3.3. Effect of feed gas composition and flowrate on SOEC degradation and syngas efficiency

4.3.3.1. Justification and set-up for this case study

The syngas composition and quality (H_2/CO ratio) are crucial parameters for the synthesis of hydrocarbons via the FTS process because they affect the selectivity and activity of FTS catalysts (Gorimbo et al., 2018). Desired H_2/CO ratios for the FTS process vary between 1.8 to 2.1 (Chen et al., 2015). Another advantage of CO_2 and H_2O co-electrolysis using SOEC systems is its flexibility for achieving the desired syngas quality by adjusting the feed gas composition and inlet flowrate on the cathode side (Chen et al., 2015; Wang et al., 2019).

Therefore, it is necessary to also study the influence of these two parameters on the syngas quality during SOEC long-term operation and how they affect SOEC performance and durability. To investigate the effects of cathode feed gas composition and inlet flowrate on SOEC long-term performance, the pseudo-dynamic SOEC model was simulated in Aspen Plus® under the following operating conditions:

- The effects of feed gas composition were assessed using 360 L/hr flowrate and two scenarios S1 and S2 were considered with 30%CO_2/60%H_2O/10%H_2 and 60%CO_2/30%H_2O/10%H_2 compositions (in mole%), respectively. This set-up was chosen in comparison to the scenario S0: 45%CO_2/45%H_2O/10%H_2 used in the previous Sections 4.31 and 4.32.

- Based on previous results, SOEC temperature and current density of respectively 750°C and 1.0 A/cm^2 were used.

- The effect of inlet flowrate was studied by varying from 290 to 420 L/hr to look into the effects of lower and higher flowrates on SOEC long-term performance

- SOEC characteristics and remaining parameters remained the same as detailed in Tables 3.4 and 3.5.

4.3.3.2. Results and discussion

Table 4.1 and Figure 4.4 and portray the effects of feed gas composition on SOEC voltage, syngas quality and syngas production efficiency during long-term operation. The results showed that lowering CO_2 content in the feed gas from 60 to 30 mol% results in a higher H_2/CO ratio from roughly 0.6 to 2.0. This is caused by the RWGS reaction (Reaction 3.39) also taking place during CO_2 and H_2O co-electrolysis. An analysis of the reaction kinetics revealed that higher H_2O mole fractions favour backwards RWGS reaction. This leads to a strongly positive RWGS reaction rate which produces more H_2 whilst CO is further consumed (Ni, 2012b).

Table 4.1: Results of SOEC simulation for different feed gas compositions

Parameter	S0	S1	S2
$H_2O/CO_2)_{in}$	1.39	2.71	0.74
$H_2/CO)_{out}$	1.07	1.99	0.59
U_{EQ} (V)	1.23	1.12	1.37
$\eta_{syngas})_0$ (%)	52.96	55.43	50.52
$\eta_{syngas})_{20,000}$ (%)	42.89	44.41	41.37
ΔU (%/1000hrs)	2.56	2.82	2.31
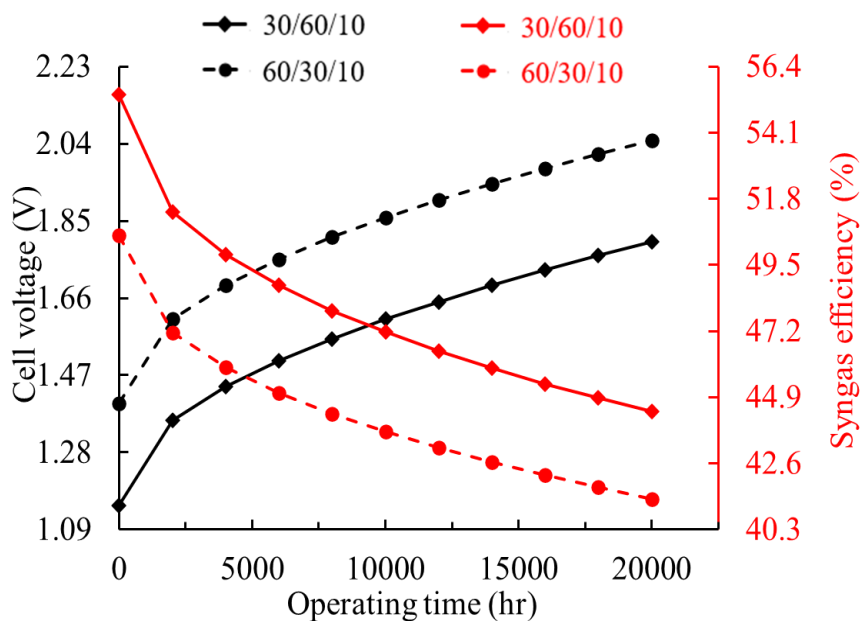
Figure 4.4: Long-term SOEC performance analysis for different feed gas compositions S1: 30/60/10 and S2: 60/30/10

Furthermore, the feed gas with a higher CO_2 content requires more voltage than the one with higher a H_2O mole fraction. To elaborate, SOEC required voltage for scenario S2 increased from 1.4 to 2.1 V whereas, the required voltage remained below 1.8 V for scenario S1 after 20,000 hours of operation. A possible explanation could be the rise in concentration overpotentials due to slower diffusion kinetics of CO_2 molecule compared to that of H_2O (Graves et al., 2011; Ni, 2012b).

As a result, the syngas production efficiency was higher in scenario S1 than S2 (55.4 to 44.4% and 50.5 to 41.4% after 20,000 hours of operation, respectively) due to both higher H_2/CO produced and lower voltage/power requirement. However, it was also found that SOEC average degradation was slightly lower in scenario S2 than S1 (2.3 and 2.8 %/1000hrs, respectively). This small difference could be from the overpotentials arising from Ni sintering which is further enhanced via Ni re-oxidation (Reaction 4.5) in the presence of H_2O (Sehested et al., 2004).

$$H_2O + 2Ni \rightleftharpoons Ni_2OH + 0.5H_2 \tag{4.5}$$
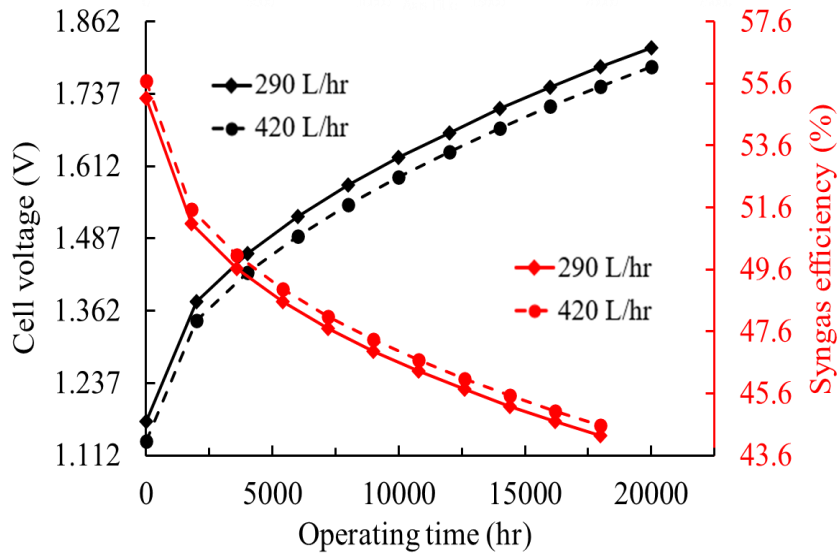
Figure 4.5: Long-term SOEC performance analysis for different cathode inlet flowrates

On the other hand, the increase in the inlet flowrate did not have significant effects on SOEC long-term performance. As illustrated in Figure 4.5, syngas production efficiencies are approximately 44.6 and 44.2% for 420 and 290 L/hr, respectively after 20,000 hours of operation. In both cases, a quite similar average degradation rate of 2.8 %/1000hrs was found. The results simply reflect the higher amount of reactants available for co-electrolysis which led to higher syngas production.

Similar findings were reported by Menon et al. (2015) when analysing the effects of inlet flowrates on SOEC performance under co-electrolysis mode. Since the conversion of reactants is also limited by a given current density (Equation 3.40), the required voltage decreases with higher flowrates due to lower reactant conversion. However, it is important to specify that increasing inlet feed flowrate may also lead to additional costs not only for raw materials but also for waste disposal arising from unconverted reactants.

4.4. Effects of structural degradation on SOEC long-term performance

4.4.1. Justification and set-up for this case study

Process analysis of SOEC long-term performance considering the operating conditions achieved some improvement in SOEC degradation rate with a decrease from 4.47 to 4.04 %/1000hrs at the current density of 1.5 A/cm^2. However, this value is still roughly 4 times higher than the targeted degradation rate of 1.0 %/1000hrs for SOEC commercial applications (Zhu and Lin, 2018; Wang et al., 2019).

Therefore, it is paramount to also study the effects of the structural degradation of SOEC components on SOEC long-term performance so as to understand the factors leading to the degradation of SOEC performance at high current densities. To implement this case study, the pseudo-dynamic SOEC model was simulated in Aspen Plus® under the following operating conditions:

- Temperature: 750℃, cathode inlet flowrate: 360 L/hr, feed gas composition (in mole%): 30% CO_2/60% H_2O/10% H_2 and current density: 1.5 A/cm². This set-up was chosen based on the results obtained in Sections 4.31 to 4.33.

- SOEC characteristics and remaining parameters were the same as detailed in Tables 3.4 and 3.5.

- It was assumed that when analysing one component material, the remaining SOEC materials are unchanged.

- Since the desired syngas quality was achieved from the analysis of operating conditions, SOEC long-term performance is given in this section in terms of overpotentials arising from the degradation of SOEC components.

4.4.2. Effect of cathode structural degradation on SOEC long-term performance

The evolution of Ni particle radius with operating time and the corresponding TPB length and electronic conductivity on the cathode side is portrayed in Figure 4.6a. the TPB length results are given in terms of $L_{TPB}/L_{TPB,0}$ ratio as described by Equation (3.11).

It was observed that Ni particle grows from 4.5 to 4.8 µm in radius after 20,000 hours of operation. According to Equations (3.18) to (3.21), the growth of Ni particle size results in a decrease in Ni-YSZ electronic conductivity due to a lower percolation probability of Ni particles. As a result, Ni-YSZ electronic conductivity decreases from 1,294 to 1,181 S/cm after 20,000 hours of operation.

Similarly, the TPB length also decreases with Ni particle coarsening from 1.00 to 0.89. following Equations (3.8) to (3.11), the decrease in TPB length mostly arises from the reduced number of Ni particles per unit volume. The overall effect of Ni growth on the cathodic overpotential is shown in Figure 4.6b with an increase from 17.9 to 23.0 mV. The average degradation rate resulting from the cathode structural degradation was evaluated at 0.02 %/1000hrs.
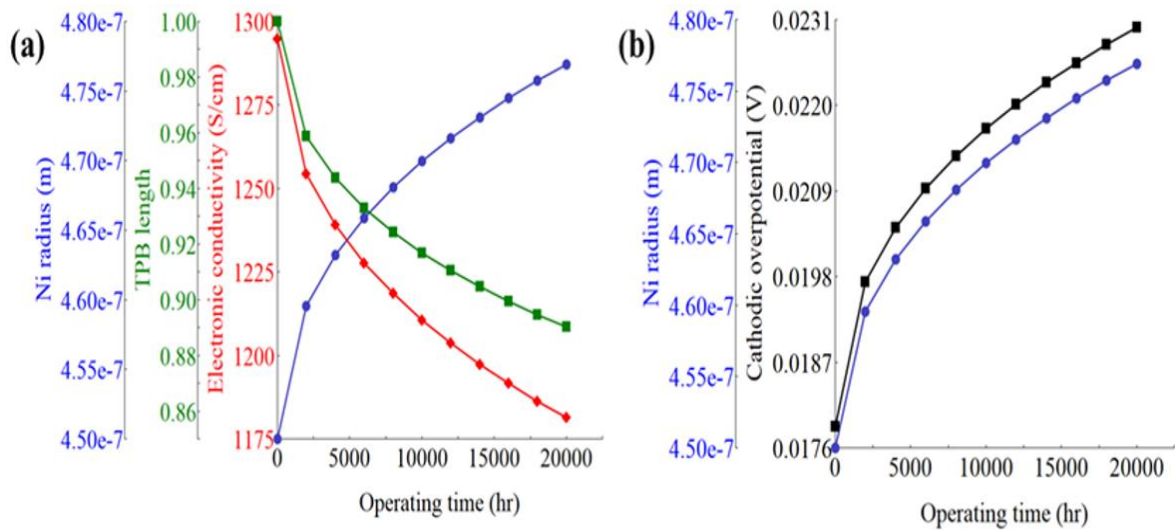
Figure 4.6: Effects of Ni particle coarsening on (a) TPB length and conductivity and (b) overpotential at the cathode electrode

4.4.3. Effect of electrolyte structural degradation on SOEC long-term performance

Figure 4.7 illustrates the evolution of ionic conductivity with operating time and the associated overpotential within the electrolyte. YSZ ionic conductivity significantly decreases the first 500 hours of operation from 0.037 to 0.029 S/cm due to the YSZ phase transition from cubic to tetragonal and remains constant thereafter at roughly 0.029 S/cm. These results are in good agreement with experimental findings reported by Kondoh et al. (1995) in their study of YSZ ionic conductivity using varying Y_2O_3 mol% of 2 to 10% at different temperatures.
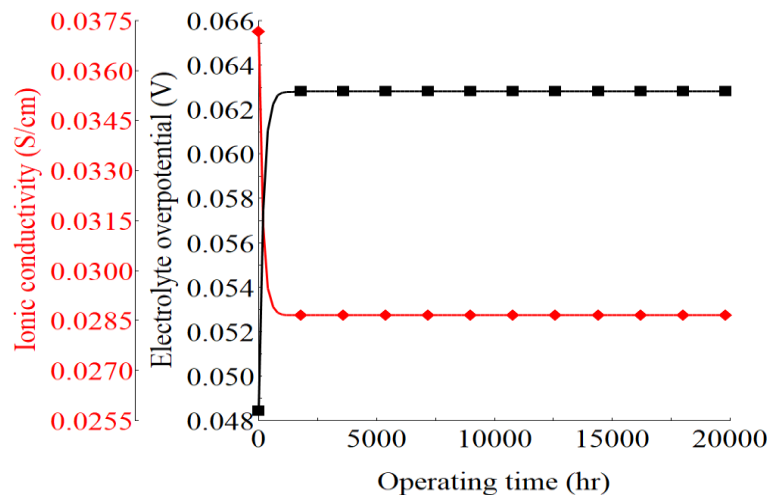
Figure 4.7: Effects of YSZ phase transition on the electrolyte ionic conductivity and overpotential

The corresponding overpotential follows the same trend and decreases according to Ohm's law (Equation 3.26) from 48.4 to 62.8 mV the first 500 hours then remains unchanged. Certainly, SOEC average degradation rate of 5.95 %/1000hrs during the first 500 hours is extremely high.

However, the contribution of electrolyte structural degradation after 20,000 hours of operation to SOEC long-term performance drops to 0.06%/1000hrs since the electrolyte overpotential stays almost constant thereafter.

Furthermore, Kondoh et al. (1995) explained that the loss in ionic conductivity during the first 500 hours is caused by the short-range order-disorder transformation occurring within the YSZ crystal lattice. Since oxygen ions can still diffuse through the electrolyte after the phase transition period, YSZ ionic conductivity remains the same once equilibrium is reached. Therefore, it is sensitive to conclude that the structural degradation of YSZ electrolyte only contributes to the short-term SOEC performance but it is not a source of SOEC degradation regarding long-term performance behaviour.

4.4.4. Effect of anode structural degradation on SOEC long-term performance

The formation of secondary phases and the effect of LSM-YSZ phase coarsening on the TPB length at the anode electrode are shown in Figure 4.8a. The thickness of COS and LZO layers gradually increases with operating time from 0 to 2.3×10^{-3} cm and 0 to 1.4×10^{-4} cm, respectively after 20,000 hours of operation. Both layers have poor conductive properties and their conductivities were evaluated at 1.3×10^{-2} and 3.4×10^{-4} S/cm for COS and LZO layers, respectively. Following Equations (3.31) and (3.32), the increase in poor conductive layers COS and LZO results in a sharp rise in ohmic overpotential at the anode electrode from 0 to 902.7 mV after 20,000 hours of operation as portrayed in Figure 4.8b.
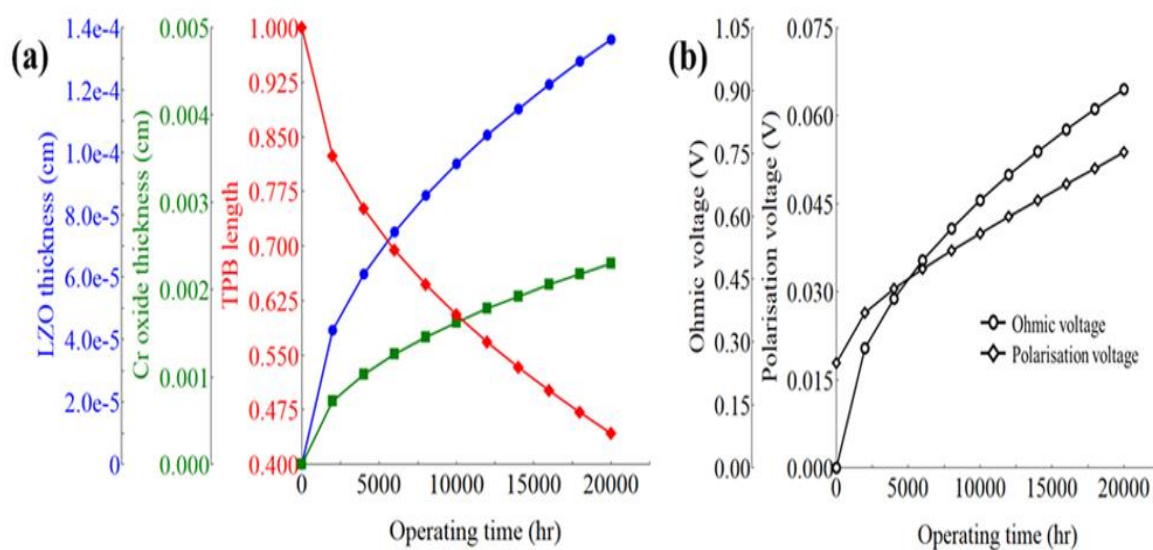
Figure 4.8: Evolution of (a) TPB length and secondary phases with operating time and (b) their corresponding overpotentials at the anode electrode

79

Moreover, LSM phase coarsening at the anode electrode causes a substantial decrease in the TPB length from 1.00 to 0.44. This leads to an increase in the polarisation voltage on the anode side from 17.9 to 53.8 mV after 20,000 hours of operation (Figure 4.8b). Overall, an anodic overpotential of 955.5 mV arises from the formation of secondary phases and LSM-YSZ phase coarsening with an average degradation rate of 3.96%/1000hrs after 20,000 hours of operation. Hence, SOEC long-term degradation essentially results from the delamination of LSM-YSZ anode electrode.

4.5. Optimisation of SOEC long-term performance through material design

4.5.1. Justification and set-up for this case study

The analysis of structural degradation of SOEC components revealed that YSZ electrolyte does not considerably contribute to SOEC degradation during long-term operation. Whereas, LSM-YSZ anode delamination followed by Ni coarsening accounted for 98.5% of SOEC average degradation rate. Since optimisation from the perspective of SOEC operating conditions only reduces the average degradation rate by 9.6% at 1.5 A/cm^2 current density, new strategies are highly needed to improve SOEC durability and lifetime.

Therefore, this section focuses on material design to improve SOEC long-term performance. The considerations for SOEC performance analysis and operating conditions remained the same as described in Section 4.4.1. Throughout this section, the base case refers to as Ni-YSZ/YSZ/LSM-YSZ composition and properties from DTU Energy Conversion (Tables 3.4 and 3.5).

4.5.2. Optimisation of Ni-YSZ cathode

Different techniques can be used to decrease Ni particle coarsening thus limiting the decrease in TPB length and electronic conductivity at the cathode electrode. Following Equations (3.7), the decrease in Ni initial particle size, increase in YSZ surface area and/or decrease in Ni/YSZ weight fraction or volume ratio could reduce Ni agglomeration over time. However, a higher loss in Ni-YSZ electronic conductivity could also arise from decreasing Ni/YSZ volume ratio (Equations 3.17 to 3.21). Moreover, a decrease in Ni initial particle size might affect the cathode porosity leading to changes in Ni-YSZ mechanical strength as well gas transport

requirement (Faes et al., 2009; Zhu et al., 2018). Therefore, this study looked into YSZ surface area to enhance Ni-YSZ composite material.

The specific surface area of YSZ powders can be greatly modified using the pre-calcination method. Jia et al. (2006) studied the effects of pre-calcining temperatures on the YSZ surface area of Ni-YSZ cermet. They reported a YSZ surface area range of 0.48 to 2.43 m^2/g for pre-calcination temperatures between 900 and 1200°C. Applying these findings in this research, sensitivity analysis was carried out in Aspen Plus® for different YSZ surface area values.

Ni agglomeration with operating time for different YSZ surface area values is depicted in Figure 4.9a in which A$_{YSZ}$ of 0.41 m^2/g corresponds to YSZ surface area in the base case. Increasing YSZ surface area considerably reduces the increase in Ni particle radius over time. To be specific, the increase of YSZ surface area from 0.41 to 1.50 m^2/g, limits Ni particle radius to 4.58 µm after 20,000 hours of operation compared to the base case wherein Ni particle size reached approximately 4.80 µm in radius.
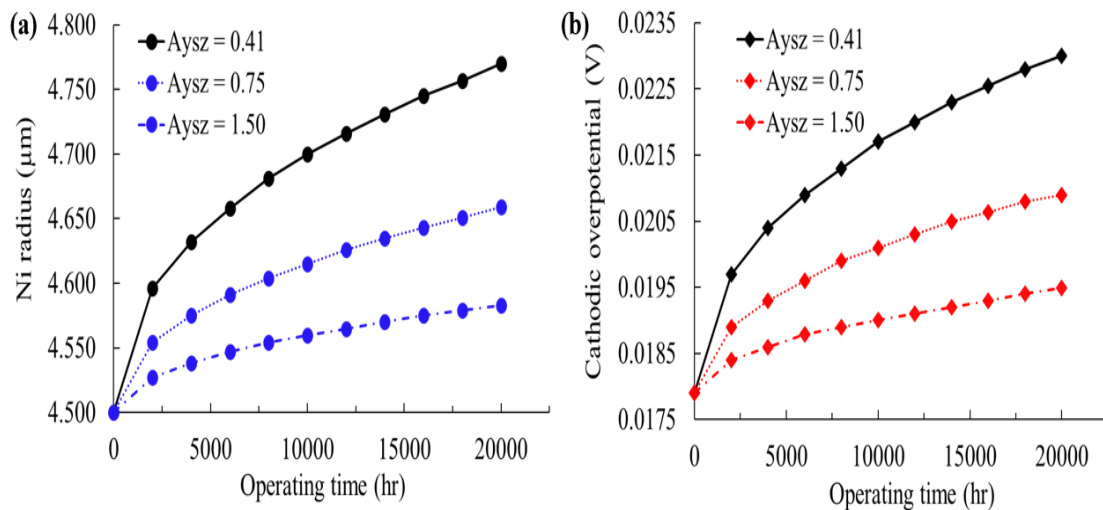
Figure 4.9: Evolution of (a) Ni radius and (b) corresponding overpotential with operating time at the cathode electrode different YSZ surface areas

As a result, the cathodic overpotential using Ni-YSZ with a YSZ surface area of 1.50 m^2/g only increases from 17.9 to 19.5 mV after 20,000 hours of operation (Figure 2.9b). This is because YSZ constitutes the framework for Ni particle dispersion and serves as an inhibitor for Ni agglomeration via sintering at high temperatures (Jia et al., 2006).

4.5.3. Optimisation of LSM-YSZ anode

The overpotential resulting from LSM-YSZ anode delamination is very rapid and unacceptable. The application of anti-oxidant coatings on the interconnect surface on the anode

side has demonstrated promising results for lowering the rate of COS growth (Palcut et al., 2012; Zhu and Lin, 2018). Palcut et al. (2012) reported a decrease in the growth rate of the COS layer from 2.40×10^{-9} (in the base case) to 1.15×10^{-10} $g^2/cm^4.hr$ by applying $La_{0.8}Sr_{0.2}CoO_3$ coating on the surface of Crofer 22 APU interconnect material.

Sensitivity analysis results using the coated Crofer 22 APU interconnect showed that the thickness of the COS layer increases from 0 to 5.0×10^{-4} cm after 20,000 hours of operation which is 4.6 times lower than COS layer growth in the base case (Figure 4.10a). $La_{0.8}Sr_{0.2}CoO_3$ coating acts as an oxygen transport barrier which decreases O_2 partial pressure at the interface between chromium oxide and coating material (Palcut et al., 2012). Lower O_2 partial pressures disfavour Reaction (3.28) hence, reduce the COS growth rate.
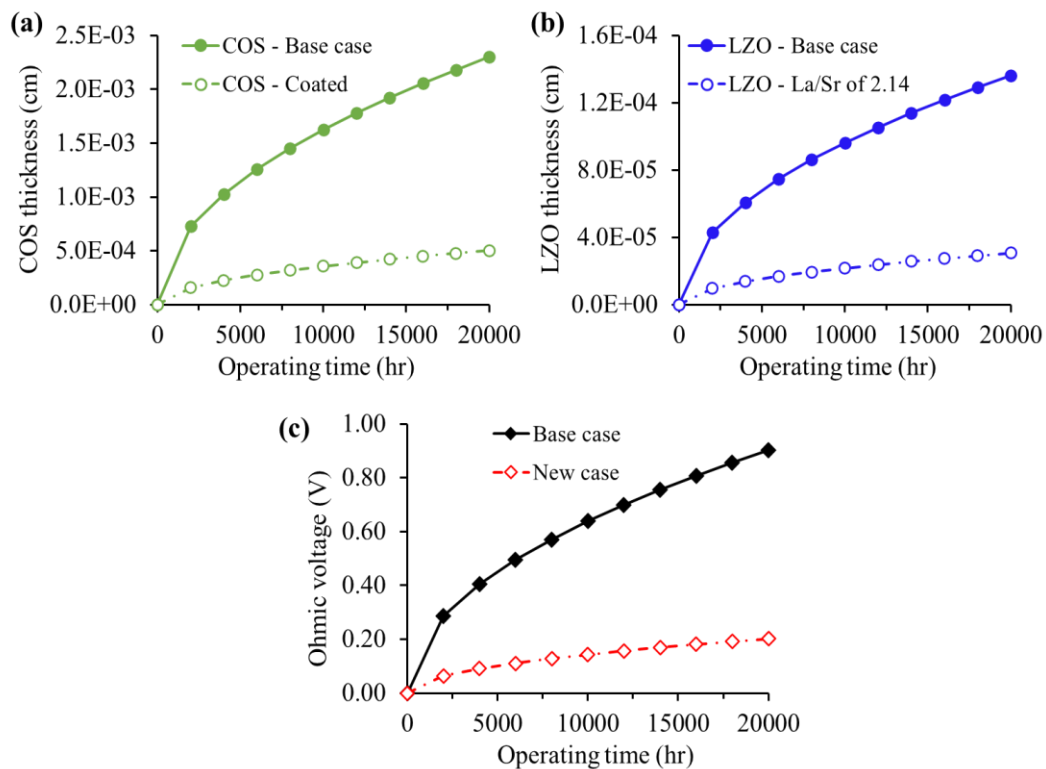
Figure 4.10: Formation of (a) chromium oxide scale (COS) and (b) lanthanum zirconate oxide (LZO) layers and their (c) corresponding ohmic overpotential for the base case and improved LSM-YSZ material

On the other hand, the growth rate of the LZO layer can be suppressed or at least delayed using lower sintering temperatures during LSM-YSZ manufacturing and/or with excess Mn in the LSM phase. Two methods can be used to achieve excess Mn in the LSM phase including doping LSM with Mn or lowering La to Sr ratio in the A-site of LSM (Mitterdorfer and Gauckler, 1998; Yang et al., 2004). The latter was investigated by Yang et al. (2004) using A-site deficient $La_{0.65}Sr_{0.3}MnO_3/YSZ$ for different sintering temperatures (1000 to 1400°C). The

authors reported a LZO growth rate of 2.26×10^{-3} g^2/cm^4.hr for $La_{0.65}Sr_{0.3}MnO_3$/YSZ composite with La/Sr ratio of 2.14 and sintered at 1000℃.

The new LZO growth rate was applied to the SOEC pseudo-dynamic model and the results showed that after 20,000 hours of operation, LZO thickness is only 3.1×10^{-5} cm compared to 1.4×10^{-4} cm found for the base case as illustrated in Figure 4.10b. This is because the formation of the LZO layer is mostly caused by Mn^{2+} diffusion via the LSM surface and $La_{0.65}Sr_{0.3}MnO_3$/YSZ has a lower surface diffusion constant than $(La_{0.75}Sr_{0.25})_{0.95}MnO_3$ for the base case which is respectively 5.76×10^{-11} and 1.12×10^{-5} cm^2/hr (Yang et al., 2004; Farlenkov et al., 2015). As shown in Figure 4.10c, the resulting ohmic overpotential using improved LSM-YSZ material was reduced by 77.6% after 20,000 hours of operation.

As elaborated in Section 3.2.3.3, LSM-YSZ phase coarsening is also due to Mn^{2+} diffusion through the LSM surface. Therefore, applying the surface diffusion constant of $(La_{0.75}Sr_{0.25})_{0.95}MnO_3$ material also slowed down the decrease in TPB length with operating time. After 20,000 hours of operation, the TPB length was still above 0.85 (Figure 4.11a) compared to 0.44 in the base case. Hence, the polarisation overpotential with the improved LSM-YSZ composite was decreased by 56.1% after 20,000 hours of operation as depicted in Figure 4.11b.
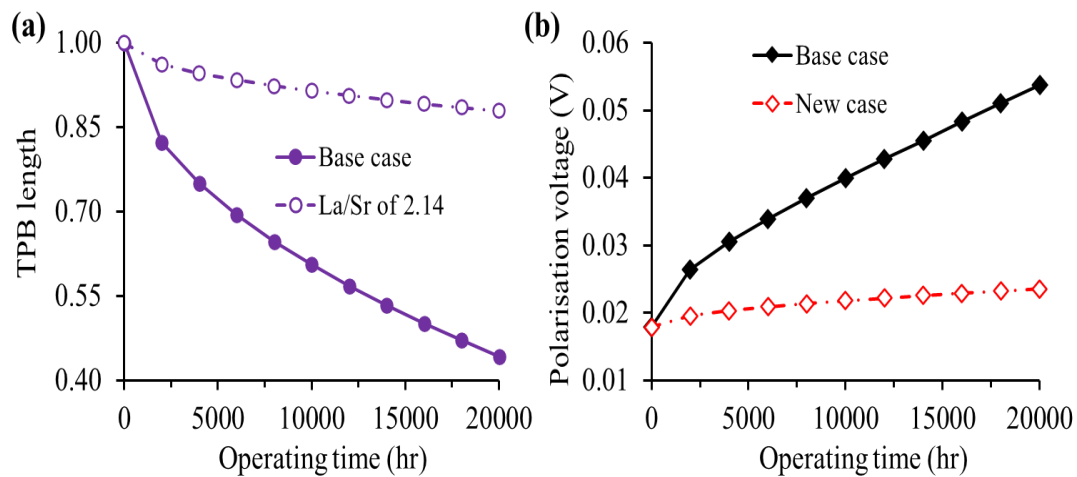
Figure 4.11: Evolution of the (a) TPB length and (b) corresponding polarisation overpotential for the base case and improved LSM-YSZ material

4.5.4. Overall SOEC performance and durability

Figure 4.12 illustrates SOEC syngas production efficiency and performance degradation arising from the structural degradation of Ni-YSZ/YSZ/LSM-YSZ composite materials. The base case using SOEC components from DTU Energy Conversion (labelled as original SOEC)

showed a decrease in syngas production efficiency from 51.7 to 36.4% after 20,000 hours of operation using a cathode inlet flowrate of 360 L/hr, feed gas composition (in mole%) of $45\%CO_2/45\%H_2O/10\%H_2$ at 800℃, 1 bar and 1.5 A/cm^2.

The average degradation rate was evaluated at 4.47%/1000 hours. After optimisation of SOEC operating conditions, adequate syngas quality was achieved with a H_2/CO ratio of 2.0. However, SOEC average degradation rate was only reduced from 4.47 to 4.04 %/1000 hours with 3.96 %/1000hrs due to LSM-YSZ anode delamination, 0.021 %/1000hrs caused by Ni agglomeration at the cathode electrode and 0.06 %/1000hrs arising YSZ electrolyte phase transformation. Material design and optimisation of Ni-YSZ/YSZ/LSM-YSZ component set showed that SOEC required voltage and syngas production efficiency respectively increases from 1.24 to 1.47 V and decreases from 54.1 to 49.9% after 20,000 hours of operation, resulting in an average degradation rate of 0.89%/1000hrs.
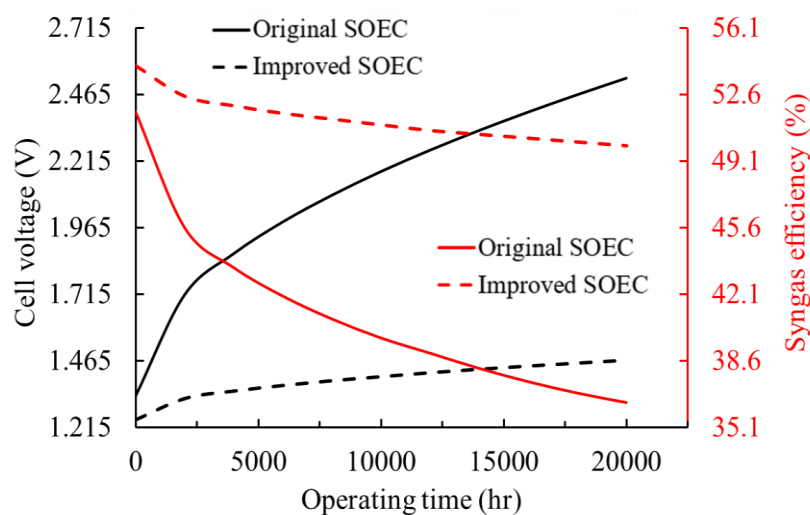
Figure 4.12: SOEC long-term performance for the original and improved Ni-YSZ/YSZ/LSM-YSZ materials

The aforementioned findings demonstrated that operating SOEC systems at adequate cathode feed gas compositions and temperatures are necessary for improving syngas quality and obtaining better degradation rates. Furthermore, the proper choice of Ni-YSZ cathode and LSM-YSZ anode composite materials together with an anti-oxidant coating of interconnect materials are critical for achieving lower SOEC degradation rates.

This study showed that the use of conventional and low-cost SOEC materials can be adequately stable for commercial applications. Though the average degradation rate of improved SOEC materials was found below the target rate for commercialisation (1.0 %/1000hrs), it is paramount to specify that improved Ni-YSZ/YSZ/LSM-YSZ materials used in this research

were experimentally tested for than 1,500 hours. Therefore, experiment-based studies on SOEC long-term degradation are still needed to fully assess the long-term stability and durability of the improved Ni-YSZ/YSZ/LSM-YSZ component set.

4.6. Conclusion

This Chapter analysed SOEC long-term performance using the 1-D pseudo-dynamic model developed and validated in Chapter 3. The effects of operating conditions such as current density, temperature, inlet gas composition and cathode flowrate on syngas production efficiency and SOEC long-term performance were studied. The structural damages of cathode, anode and electrolyte materials as well as their contributions to the degradation of SOEC performance at high current densities were examined. Finally, material designs of SOEC components were investigated for the optimisation of SOEC long-term performance.

Process analysis of SOEC operating conditions indicated that decreasing the operating temperature and increasing H_2O content in the cathode feed gas are beneficial to achieving a lower SOEC degradation rate and can help to improve the syngas quality and production efficiency. However, optimum operation conditions alone are not sufficient to reach adequate SOEC degradation rates for large-scale deployment.

The analysis of SOEC structural degradation revealed that for an average degradation rate of 4.04 %/1000hrs, 3.96 %/1000hrs arises from LSM-YSZ anode delamination whereas, Ni agglomeration at the cathode electrode and YSZ electrolyte phase transformation accounted for 0.021 and 0.06 %/1000hrs, respectively. Furthermore, YSZ electrolyte degradation only affects SOEC electrochemical performance during the first 500 hours of operation and remains stable thereafter.

Increasing YSZ surface area can help to limit Ni agglomeration at the cathode electrode. Moreover, applying anti-oxidant coatings on the interconnect surface on the anode side and varying La/Sr ratio in LSM material slowed down the formation of poor conductive layers and LSM phase coarsening at the anode electrode. As a result, SOEC average degradation rate of the improved Ni-YSZ/YSZ/LSM-YSZ component set was found below 1.0 %/1000hrs which is acceptable for commercial applications.

5. Technical analysis of direct CO_2 conversion into gasoline fuel through the modified CO_2-FTS process

5.1. Introduction

As highlighted in Chapter 2, the yield of liquid hydrocarbons from the direct CO_2-FTS process is much lower than that of the traditional FTS process using syngas. This is due to low CO_2 conversion caused by excessive water production from both RWGS and FTS reactions. Therefore, this chapter focuses on modelling, simulation and improvement of the modified CO_2-FTS process for gasoline fuel synthesis. The development and simulation of a steady-state model based on first principles of the CO_2-FTS process are elaborated in sections 5.2 and 5.3 respectively. Section 5.4 details the CO_2-FTS model validation using experimental data from Wei et al. (2017). Section 5.5 presents the performance analysis of the CO_2-FTS process to gasoline fuel using a single fixed-bed reactor compared to multiple reactors in series and a single reactor with recycle coupled with ex-situ water removal.

5.2. Steady-state model development of CO_2-FTS process

5.2.1. Study of the CO_2-FTS process

CO_2 and H_2 streams enter a fixed-bed reactor for gasoline fuel synthesis via the modified CO_2-FTS process. The general principle of the CO_2-FTS process is detailed in Section 1.1.4.2.

5.2.2. Assumptions for model development

The steady-state model of CO_2-FTS process was developed under the following assumptions:

- CO_2-FTS process operates at steady-state condition. Hence, heat and mass accumulations were not accounted for.

- CO_2-FTS model only focuses on reactant conversion and products from CO_2-FTS reactions based on mass/mole balance and reaction stoichiometry. However, the growth probability of hydrocarbons is specific to the type of reactor and operating conditions (Becker et al., 2012; Hillestad, 2015).

- The type of hydrocarbons considered in this study only depends on the catalyst nature. Furthermore, oxygenated compounds were not favoured during experiments (Wei et al., 2017). Therefore, products that can be obtained from Reaction (1.10) were neglected.

- The lumping technique was used to handle the infinite number of hydrocarbons from CO_2-FTS reactions. It is simply defined as grouping several components into a smaller number of components to represent the whole group (Hillestad, 2015).

5.2.3. Modelling of CO_2-FTS process

Most modelling/simulation, optimisation and TEA studies on the FTS process discussed in Chapter 2 used the Anderson–Schulz–Flory (ASF) theory to predict the distribution of hydrocarbons. The ASF model expresses the distribution of possible hydrocarbons in terms of their mass fractions (W_i) related to the corresponding carbon number i and chain growth probability (Equation 5.1). However, it was observed that the direct CO_2-FTS process to liquid hydrocarbons does not follow the ASF distribution theory. As illustrated in Figure 5.1, significant deviations were observed for C_2, C_3 and C_{8+} components. A possible explanation could be the isomerisation, oligomerisation and aromatisation reactions taking place during the CO_2-FTS process in addition to the polymerisation reaction (Meiri et al., 2015; Wei et al., 2017; Ye et al., 2019).

$$W_i = i \times (1 - \alpha)^2 \times \alpha^{i-1} \tag{5.1}$$
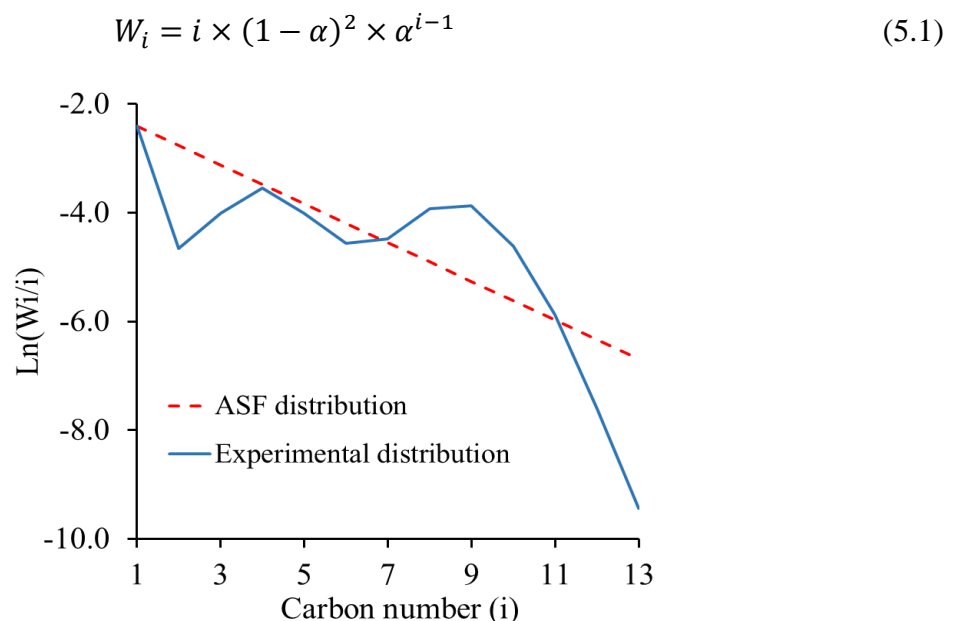
Figure 5.1: Calculated ASF distribution compared to experimental CO_2-FTS product distribution. Experimental data taken from Wei et al. (2017)

Therefore, a modified version of the ASF theory is used to assess CO_2-FTS product distribution based on the one described by Donnelly et al. (1988). The modified ASF distribution considers

87

two chain growth probabilities to evaluate the total product mass fraction for i carbon number as shown in Equation (5.2). Assuming that each term in Equation (5.2) contributes equally at the breakpoint (with carbon number b) in the ASF theory, the fraction f_2 is then calculated using Equation (5.3).

$$W_i = f_1 \times \alpha_1^{i-1} + f_2 \times \alpha_2^{i-1} \tag{5.2}$$

$$f_1 \times \alpha_1^{b-1} = f_2 \times \alpha_2^{b-1} \Rightarrow f_2 = f_1 \times \left(\frac{\alpha_1}{\alpha_2}\right)^{b-1} \tag{5.3}$$

The sum of mass fractions for all carbon numbers is unity (Equation 5.4). However, C_2 and C_3 compounds do not follow the theoretical ASF distribution (Todic et al., 2013; Stempien et al., 2015; Selvatico et al., 2016). Therefore, they are removed in the modified ASF model and calculated separately (Equations 5.5 and 5.6) based on the kinetic values proposed by Todic et al. (2013) and adapted in this study for the CO_2-FTS process.

$$\sum_{i=1}^{\infty} W_i = \sum_{i=1}^{\infty}\left[f_1 \times \alpha_1^{i-1} + f_2 \times \alpha_2^{i-1}\right] = 1 \tag{5.4}$$

$$\alpha_{C_2} = \frac{k_1 P_{CO_2}}{k_1 P_{CO_2} + k_5 P_{H_2} + k_{6E} e^{2c}} \tag{5.5}$$

$$\alpha_{C_3} = \frac{k_1 P_{CO_2}}{k_1 P_{CO_2} + k_5 P_{H_2} + k_{6,0} e^{3c}} \tag{5.6}$$

After removing the mass fractions of C_2 and C_3 hydrocarbons, Equation (5.4) becomes (5.7) for hydrocarbons with carbon number $i = 1$ and $i \geq 4$. Considering the geometric series (Equation 5.8) and substituting f_2 into Equations (5.7) and (5.8), the fraction f_1 can be evaluated using Equation (5.9). Note that in Equation (12), the term $[f_1 \cdot \alpha_1(1 + \alpha_1) + f_2 \cdot \alpha_2(1 + \alpha_2)]$ represents the sum of mass fraction W_2 and W_3, calculated using Equation (5.2). A fitting parameter (λ) was used to account for the aromatisation of light HCs (Stempien et al., 2015; Wei et al., 2017).

$$\sum_{i=1,4}^{\infty} W_i = \sum_{i=1}^{\infty}\left[f_1 \times \alpha_1^{i-1} + f_2 \times \alpha_2^{i-1}\right] - [f_1 \cdot \alpha_1(1 + \alpha_1) + f_2 \cdot \alpha_2(1 + \alpha_2)] = 1 - W_2 - W_3 \tag{5.7}$$

$$\sum_{i=1}^{\infty}\left[f_1 \times \alpha_1^{i-1} + f_2 \times \alpha_2^{i-1}\right] = f_1[1/(1 - \alpha_1)] + f_2[1/(1 - \alpha_2)] \tag{5.8}$$

$$f_1 = \lambda \frac{1 - W_2 - W_3}{[1/(1-\alpha_1)] + \alpha_1 \cdot (1+\alpha_1) + [(1/(1-\alpha_2)) - \alpha_2 \cdot (1+\alpha_2)](\alpha_1/\alpha_2)^{b-1}} \tag{5.9}$$

Nevertheless, even the modified ASF distribution model does not consider any difference among components with the same carbon number. Hence, distinctions within the same carbon

cuts were taken into consideration based on the catalyst characteristics. In this study, Na-Fe$_3$O$_4$/HZSM-5 catalyst was considered leading to five types of hydrocarbons including n-paraffins, isoparaffins, olefins, naphthenes and aromatics (Wei et al., 2017). Since hydrocarbon distributions are based on their selectivity in C-mole %, the mass fraction obtained from the modified ASF theory is converted into their corresponding selectivity (S_i) using Equations (5.10) to (5.12). Selectivities are then distributed to each hydrocarbon type for a given carbon number based on catalyst features as provided by Wei et al. (2017). Data for the repartition of hydrocarbon types is given in Appendix A.1.

$$x_i = \frac{W_i}{M_i} \times \overline{M} \tag{5.10}$$

$$\frac{1}{\overline{M}} = \sum_{i=1}^{n} \frac{W_i}{M_i} \tag{5.11}$$

$$S_i = \frac{x_i \times i}{\sum_{i=1}^{n} x_i \times i} = \frac{\dot{n}_{HC_i} \times i}{\sum_{i=1}^{n} \dot{n}_{HC_i} \times i} \tag{5.12}$$

The CO$_2$-FTS reactor accomplishes several reactions including the RWGS reaction for CO$_2$ conversion followed by FTS reactions using produced CO (Table 5.1). The molar extent of each FTS reaction is calculated based on the stoichiometry and carbon mole balance as follows (Hillestad, 2015):

$$\frac{\dot{n}_{CO_{in}}}{i} \times X_{CO_i} = \dot{n}_{HC_i} \tag{5.13}$$

Table 5.1: CO$_2$-FTS carbon range, selected components and chemical reactions

Carbon range	Product category	Model i	Component	Chemical reaction
$i = 1$	CO	1	CO	$CO_2 + H_2 \rightarrow CO + H_2O$
	Methane		Methane	$CO + 3H_2 \rightarrow CH_4 + H_2O$
$2 \leq i \leq 4$	Light HCs	3 and 4	Propane	$3CO + 7H_2 \rightarrow C_3H_8 + 3H_2O$
			Propene	$3CO + 6H_2 \rightarrow C_3H_6 + 3H_2O$
			i-Butane	$4CO + 9H_2 \rightarrow i\text{-}C_4H_{10} + 4H_2O$
$5 \leq i \leq 11$	Gasoline	8	n-Octane	$8CO + 17H_2 \rightarrow n\text{-}C_8H_{18} + 8H_2O$
			i-Octane	$8CO + 17H_2 \rightarrow i\text{-}C_8H_{18} + 8H_2O$
			Octene	$8CO + 16H_2 \rightarrow C_8H_{16} + 8H_2O$
			Cyclo-Octane	$8CO + 16H_2 \rightarrow c\text{-}C_8H_{16} + 8H_2O$
			Xylene	$8CO + 13H_2 \rightarrow C_8H_{10} + 8H_2O$

| $i \geq 12$ | Wax | 20 | Icosane | $20CO + 41H_2 \rightarrow C_{20}H_{42} + 20H_2O$ |

Equation (5.13) is re-arranged as (5.14) and applied to all FTS reactions taking place to evaluate the sum as given by Equation (5.15). Where, $\sum_{i=1}^{n} i \times \dot{n}_{HC_i}$ represents the total molar extent of produced hydrocarbons and $\sum_{i=1}^{n} X_{CO_i}$ is the total CO conversion. Therefore, Equation (5.15) is re-written as Equation (5.16).

$$i \times \dot{n}_{HC_i} = X_{CO_i} \times \dot{n}_{CO_{in}} \tag{5.14}$$

$$\sum_{i=1}^{n} i \times \dot{n}_{HC_i} = \dot{n}_{CO_{in}} \times \sum_{i=1}^{n} X_{CO_i} \tag{5.15}$$

$$\dot{N}_{HC} = X_{CO} \times \dot{n}_{CO_{in}} \tag{5.16}$$

The same principle is applied to the RWGS reaction to assess $\dot{n}_{CO_{in}}$ as shown by Equation (5.17). Equations (5.16) and (5.17) are combined to obtain Equation (5.18) which is then applied to Equation (5.12) to calculate the molar extent of each FTS reaction as shown by Equation (5.19).

$$\dot{n}_{CO_{in}} = \dot{n}_{CO_{out}} \big)_{RWGS} = X_{CO_2} \times \dot{n}_{CO_{2in}} \tag{5.17}$$

$$\dot{N}_{HC} = X_{CO} \times X_{CO_2} \times \dot{n}_{CO_{2in}} \tag{5.18}$$

$$\dot{n}_{HC_i} = \frac{S_i}{i} \times \dot{N}_{HC} \tag{5.19}$$

5.3. CO₂-FTS model implementation

The implementation of CO₂-FTS model was carried out in Aspen Plus® software using Peng-Robinson as the property method. The Peng-Robinson physical property is widely used for refinery and gas applications to estimate the thermodynamic properties of hydrocarbons. It was chosen based on the Aspen Physical Property System guide and previous modelling/simulation studies on the FTS process (Dimitriou et al., 2015; Stempien et al., 2015; Fernández-Torres et al., 2022).

Figure 5.2 illustrates the CO₂-FTS process flowsheet developed in this work. It was assumed that H₂ and CO₂ are both available at standard conditions. H₂ and CO₂ streams are initially compressed to the desired pressure using a 4-stage compressor with intercooling. The compressed gases are then mixed and heated to the reactor operating temperature. Afterwards, the resulting stream (HT-FEED) is sent to the CO₂-FTS reactor. In reality, the CO₂-FTS reactor

is a fixed-bed reactor as per experiments carried out at the Dalian National Laboratory for Clean Energy in China (Gao et al., 2017; Wei et al., 2017, 2018). In this study, the CO_2-FTS reactor is represented as a stoichiometry reactor block (CO_2-FTR) and Fortran® routines were used to assess the distribution of hydrocarbons. Table 5.2 recapitulates the equations implemented in Aspen Plus®.
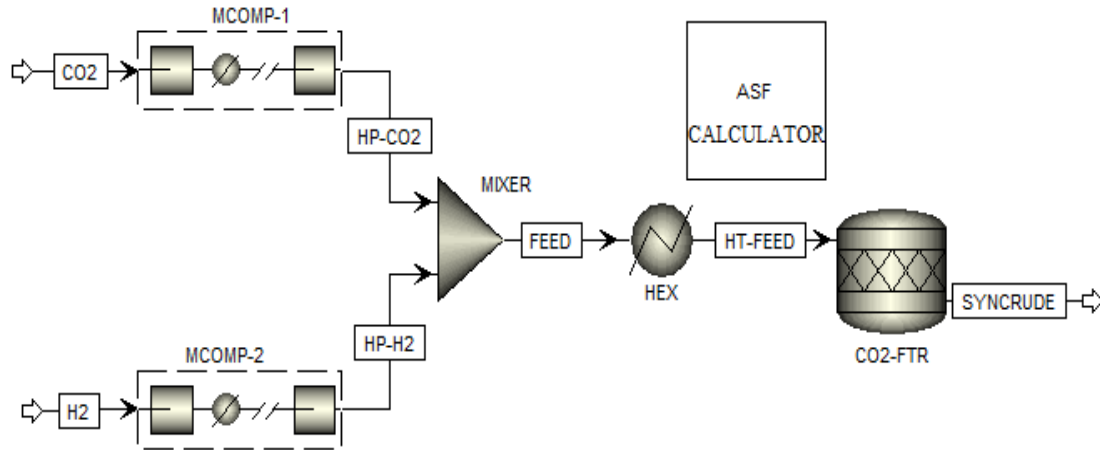
Figure 5.2: Flowsheet of CO_2-FTS process in Aspen Plus

Table 5.2: Summary of CO_2-FTS mathematical modelling

Parameter	Equation
Growth probability of C_2 component	Equation (5.5)
Growth probability of C_3 component	Equation (5.6)
Product fraction related to α_1	Equation (5.9)
Product fraction related to α_2	Equation (5.3)
Mass fraction for carbon number i	Equation (5.2)
Average molar mass of hydrocarbons	Equation (5.11)
Mole fraction of component i	Equation (5.10)
Selectivity of component i	Equation (5.12)
Total molar extent of total hydrocarbons	Equation (5.18)
Molar extent of component i	Equation (5.19)

The modified ASF distribution model was first calculated in a separate spreadsheet for every carbon number ranging from 1 to 50. In order to handle the wide range of possible components in the model, lumping of components was performed as summarised in Table 5.1. For each carbon range, a specific carbon number and corresponding hydrocarbons were chosen to

represent the product category. Appendices A.2 and A.3 provide details of initial ASF calculations and lumping of components respectively. Then considering Table 5.2, Fortran® routines evaluate the molar extent of each chemical reaction accomplished by the stoichiometry reactor block.

5.4. CO₂-FTS model validation

The CO_2-FTS model was validated using data from experiments conducted at the Dalian National Laboratory for Clean Energy in China (Wei et al., 2017). Details on the experimental CO_2-FTS reactor are elaborated in Section 2.3.1 (Table 2.7). Six sets of experiments were carried out to assess the hydrocarbon selectivities for different H_2/CO_2 feed ratios. Data using H_2/CO_2 ratios of 1.0 and 3.0 were selected for the model validation. This is because they achieved more than 70% selectivity towards gasoline-range hydrocarbons.

The input process conditions and parameters used for the CO_2-FTS model validation are given in Table 5.3. Not all required data were available from Wei et al. (2017). Thus, some parameters were assumed based on available literature as detailed in Table 5.3. The validation results are provided in terms of hydrocarbons and CO selectivities (in C-mole%) for different H_2/CO_2 ratios. Figures 5.3a and 5.3b show good agreement between experimental data and model predictions for both H_2/CO_2 feed ratios.

Table 5.3: Input parameters for CO_2-FTS model validation

Parameter		Value		Reference
Reactor temperature (℃)		320		(Wei et al., 2017)
Reactor pressure (bar)		30		
H_2/CO_2 ratio (mol basis)		3.0	1.0	
Inlet H_2 and CO_2 temperature (℃)		25		
Inlet H_2 and CO_2 pressure (bar)		1		
Inlet feed flowrate		4.0 L/hr		
CO_2 conversion		0.34	0.22	
Hydrocarbon chain growth probability	α_1	0.75		(Donnelly et al., 1988)
	α_2	0.82		
Carbon number at break point		7		
Kinetic constants	k_1	1.66×10^{-2}		(Todic et al., 2013)
	k_5	6.99×10^{-4}		
	$k_{6,0}$	2.02×10^{-2}		

	k$_{6E}$	7.62×10^{-5}	
Constant c		-0.26	
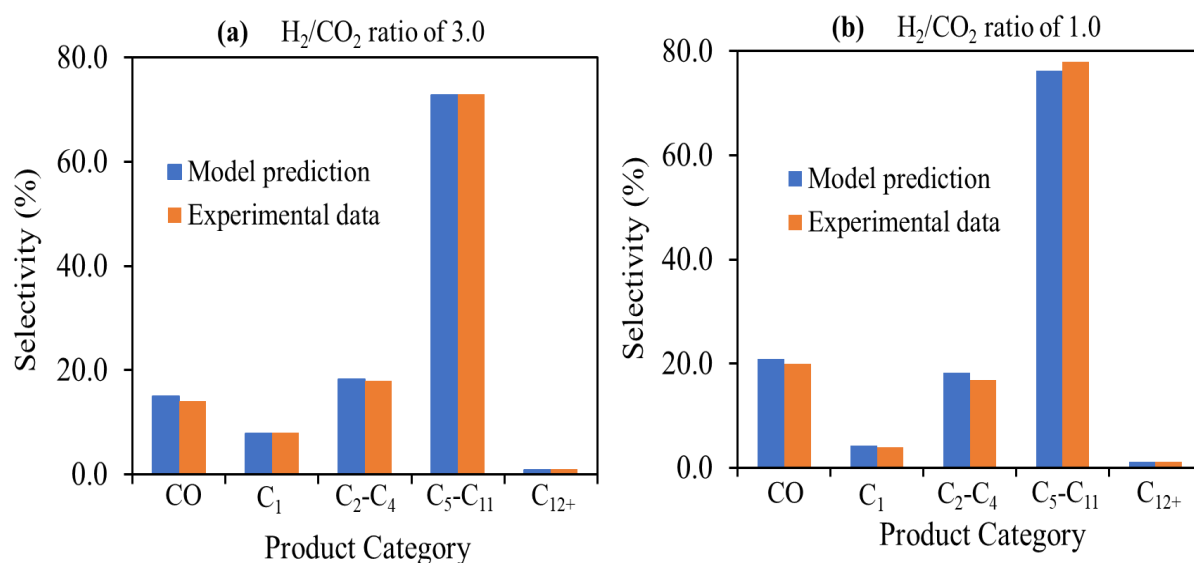
Figure 5.3: Model predictions and experimental values of CO_2-FTS product selectivities for different H_2/CO_2 feed ratios

The relative errors between model predictions and experimental values for each product category were also calculated and they are elaborated in Table 5.4. For H_2/CO_2 ratios of 1.0 and 3.0, relative errors were found below 9.0% and 7.0% respectively. Therefore, the CO_2-FTS model developed in Aspen Plus® using Fortran® routines can reasonably predict the gasoline-range hydrocarbons (C_5-C_{11}) and can be used for further performance analysis.

Table 5.4: Relative errors between model predictions and experimental values CO_2-FTS product selectivities

Product category	Relative errors (%)	
	H_2/CO_2 of 3.0	H_2/CO_2 of 1.0
CO	6.65	4.50
CH$_4$	1.38	7.00
C$_2$-C$_4$	1.60	8.93
C$_5$-C$_{11}$	0.16	2.18
C$_{12+}$	6.97	6.67

5.5. Performance analysis of CO_2-FTS process for gasoline fuel synthesis

5.5.1. Assumptions and evaluation criteria for CO_2-FTS performance analysis

In this section, the CO_2-FTS model developed and validated was used to carry out the performance analysis of the CO_2-FTS process to gasoline fuel. CO_2-FTS performance analysis was performed under the following assumptions:

- Although the CO_2-FTS model validation was performed at a laboratory-scale, process analysis was carried out on an industrial-scale under the assumptions that both CO_2-FTS reactor and Na-Fe_3O_4/HZSM-5 catalyst behave the same way at lab-scale and industrial-scale.

- The amount of reactants fed into the CO_2-FTS plant is based on the plant scale. CO_2 and H_2 inlet flowrates were assumed to be 110.02 and 15.12 ton/hr respectively. These values were chosen to achieve a commercial CO_2-FTS plant capacity of 4,500 bbl/day (Fernández-Torres et al., 2022).

- CO_2-FTS process performance is given in terms of CO_2 conversion, gasoline yield, energy consumption and process efficiency.

- CO_2-FTS process efficiency and gasoline yield were calculated using Equations (5.20) and (5.21) respectively. The CO_2-FTS process efficiency considers the high heating values (HHV) of gasoline fuel and feed gases as well as the required energy of each operation units (Becker et al., 2012; Cinti et al., 2016).

$$\eta_{CO_2-FTS} = \frac{HHV_{gasoline}}{HHV_{in} + \mathcal{P}_{CO_2-FTS}} \tag{5.20}$$

$$Y_{gasoline} = X_{CO_2} \times S_{gasoline} \tag{5.21}$$

$$X_{CO_2} = \frac{\dot{n}_{CO_2{in}} - \dot{n}_{CO_2{out}}}{\dot{n}_{CO_2{in}}} \tag{5.22}$$

- Except for the preliminary CO_2-FTS process which has a fixed CO_2 conversion as specified by Wei et al. (2017), CO_2 conversion in the remaining case studies was assessed using Equation (5.22).

- Considering the current maturity of FTS reactors, 5% heat losses were assumed during calculations of the CO_2-FTS process efficiency (Saeidi et al., 2015).

5.5.2. CO_2-FTS process performance using a single reactor

5.5.2.1. Justification for this case study

CO_2-FTS process using a single reactor features an open-loop configuration without the recirculation or upgrade of unconverted reactants, water removal and/or reactor design. It is referred to as preliminary plant or base case and the obtained results were used as a foundation for performance comparison between the preliminary and optimised plants. The study of the preliminary CO_2-FTS plant was necessary to evaluate the single performance of each operation unit, especially the CO_2-FTS reactor block.

5.5.2.2. Process simulation of CO_2-FTS process to gasoline fuel using a single reactor

The process simulation of the preliminary CO_2-FTS plant for gasoline fuel synthesis is displayed in Figure 5.4a. In this preliminary process plant, the syncrude stream leaving the CO_2-FTS reactor is first cooled down to 40℃ based on the temperature performance of industrial coolers (Meiri et al., 2017).
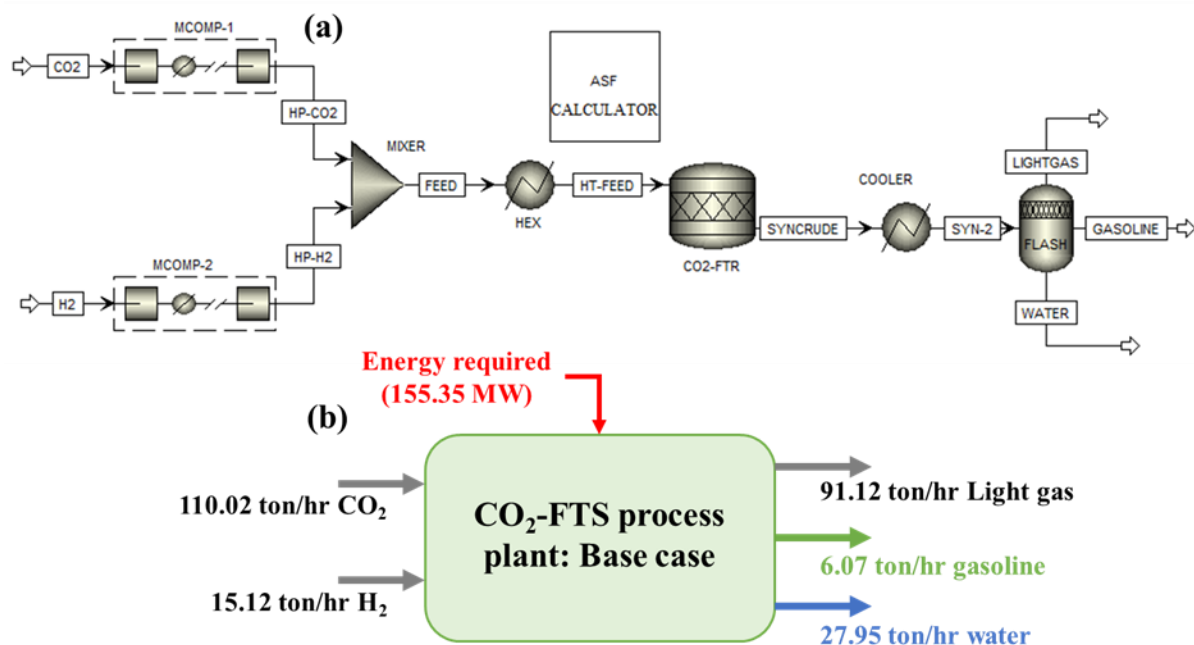
Figure 5.4: (a) CO_2-FTS preliminary process simulation and (b) overall material mass balance

The resulting stream (SYN-2) is then separated into three streams using a three-phase outlet flash drum: light gas stream (containing unconverted feed gases and light hydrocarbons), gasoline stream (mostly C_5-C_{11} hydrocarbons) and water stream. The remaining operating

conditions of the CO_2-FTS process to gasoline were the same as presented in Table 5.3 for the H_2/CO_2 ratio of 3.0.

5.5.2.3. Performance analysis of CO_2-FTS process to gasoline fuel using multiple reactors in series

The overall material balance of the preliminary CO_2-FTS plant is presented in Figure 5.4b. The characteristics of the produced gasoline as well as the process performance were verified and the results are presented in Table 5.5. The gasoline fuel has a density of 767.1 kg/m^3 and a research octane number (RON) of 94.6 which is between the current gasoline RON grade range of 80 to 110 (Stratas Advisors, 2021). The preliminary CO_2-FTS process plant led to roughly 6.1 ton/hr of gasoline fuel, 28.0 ton/hr of water and 91.1 ton/hr of light gas. The total energy required was evaluated at 155.4 MW which resulted in a CO_2-FTS process efficiency of approximately 39.0%.

Table 5.5: Performance summary of the CO_2-FTS preliminary process design

Parameter		Value
Gasoline fuel features	Mass flowrate (ton/hr)	6.07
	Density (kg/m^3)	767.13
	RON	94.56
	HHV (MW)	75.88
Energy consumption (MW)	Feed compressors	70.79
	Feed heater	10.86
	Reactor cooling jacket	22.53
	Syncrude cooler	43.20
	Flash drum	0.57
	Heat loss (5%)	7.40
Conversion (%)	CO_2	34.00
	CO	85.35
Gasoline yield (%)		24.78
CO_2-FTS process efficiency (%)		38.96

The CO_2-FTS process achieved a gasoline selectivity of 72.9% with methane selectivity below 8.0% which agrees with the experimental results when using Na-Fe_3O_4/HZSM-5 catalyst for direct CO_2 conversion into gasoline fuel (Wei et al., 2017). Furthermore, the direct CO_2-FTS process resulted in roughly 1.0% selectivity towards C_{12+} hydrocarbons (Figure 5.3) based on

Na-Fe$_3$O$_4$/HZSM-5 catalyst characteristics. Therefore, a distillation column was not required for the syncrude upgrade to liquid fuels. However, the gasoline yield was only 24.8% due to low CO$_2$ conversion (approximately 34.0%). The results also indicated that the light gas stream (Figure 5.4) contains respectively 72.4 ton/hr and 10.4 ton/hr of CO$_2$ and H$_2$ mass flowrate representing more than 90% of the total light gas flowrate. It will be shown in the next sections that the light gases can be re-used to optimise the CO$_2$-FTS process performance.

5.5.3. CO$_2$-FTS process performance using multiple reactors in series

5.5.3.1. Justification for this case study

Water formation during direct CO$_2$ conversion into liquid fuels significantly decreases the driving force of the RWGS reaction, hence inhibiting CO$_2$ conversion. Continuous and selective water removal is therefore essential to achieve a higher RWGS reaction rate and CO$_2$ conversion (Guo et al., 2018; Saeidi et al., 2021). Since the improvement of liquid fuel yield has become more challenging from the catalyst design perspective (Guo et al., 2018), new strategies are indispensable to enhance CO$_2$ conversion and liquid fuel yield. As a result, this study looked into multiple CO$_2$-FTS reactors in series with interstage cooling for ex-situ water removal to assess the effects of the multi-stage reactor system on CO$_2$ conversion, gasoline yield, energy consumption and process efficiency.

5.5.3.2. Process simulation of CO$_2$-FTS process to gasoline fuel using multiple reactors in series

Simulation and performance analysis of the CO$_2$-FTS process using a multi-stage reactor system were also performed in Aspen Plus® software. Figures 5.5a and 5.5b depict the configuration concept of the CO$_2$-FTS process using multiple reactors in series and process simulation of a 2-stage CO$_2$-FTS reactor system in Aspen Plus® respectively. A single CO$_2$-FTS reactor unit includes a heat exchanger, fixed-bed reactor (modelled as a stoichiometry reactor block), cooler and three-outlet flash drum. The aforementioned operation units operate as described in Sections 5.3 and 5.5.2.
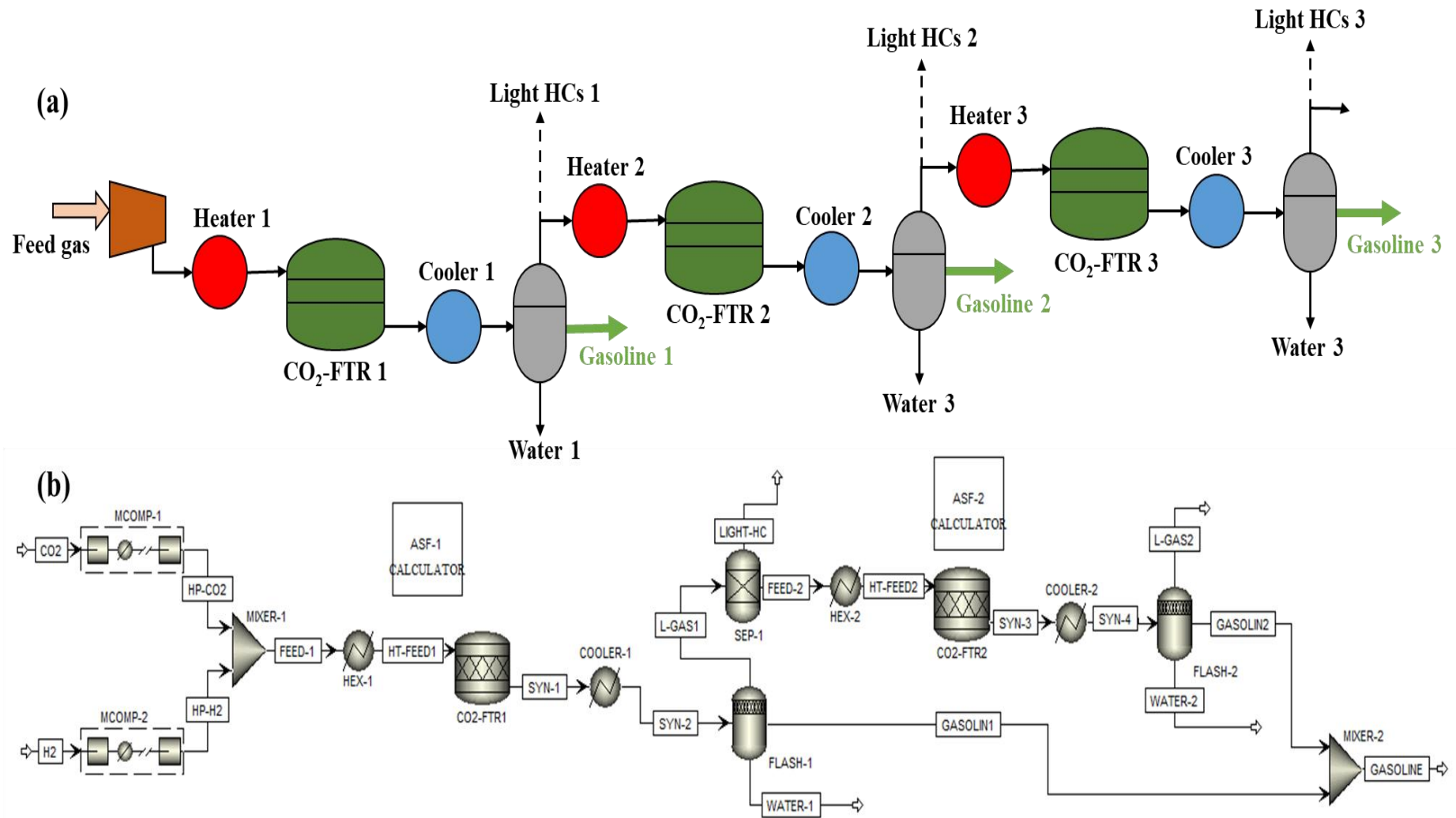
Figure 5.5: (a) Configuration concept and (b) process simulation of CO_2-FTS to gasoline using multiple reactors in series

For a multi-stage reactor system, the light gas stream (L-GAS1) exiting the flash drum (FLASH-1) first goes through a separation stage wherein light hydrocarbons (C_1-C_4) are removed from the next feed stream. It is important to specify the recovered light hydrocarbons could also be used for further plant optimisation such as electricity generation through combustion. However, this is beyond the scope of this study and good discussions are available elsewhere (Selvatico et al., 2016; Fernández-Torres et al., 2022).

The second feed stream (FEED-2), mostly containing unconverted CO_2, H_2 and CO, is then sent to the next CO_2-FTS reactor unit. Up to three reactors in series were studied. Each CO_2-FTS reactor accomplishes the chemical reactions elaborated in Table 5.1 and Fortran® routines assess the molar extent of each reaction. Finally, a mixer is used to combine all gasoline streams leaving the flash drums.

5.5.3.3. Performance analysis of CO_2-FTS process to gasoline fuel using multiple reactors in series

The results provided in this section were obtained under the operating conditions presented in Table 5.3 for the H_2/CO_2 ratio of 3.0, using CO_2 and H_2 inlet flowrates of 110.02 and 15.12 ton/hr, respectively. Moreover, each CO_2-FTS reactor unit operates under the same conditions. Table 5.6 summarises the CO_2-FTS process performance using a 1-stage (preliminary CO_2-FTS plant) compared to a 2-stage and 3-stage reactor in series. The results showed that using a 2-stage CO_2-FTS reactor system increases CO_2 conversion from 34.0 to 56.6%. This led to a gasoline yield of 41.6% which was 1.7 times higher than that of the CO_2-FTS process in a single reactor. Furthermore, the 3-stage CO_2-FTS reactor system achieved 52.5% gasoline yield with a considerable increase in CO_2 conversion from 34.0 to 71.5% and up to 96.2% CO conversion.

Table 5.6: Performance summary of the CO_2-FTS process using multiple reactors in series

Parameter		1 reactor (base case)	2 reactors in series	3 reactors in series
Gasoline fuel features	Mass flowrate (ton/hr)	6.07	11.33	16.74
	Density (kg/m^3)	767.13	766.15	765.77
	HHV (MW)	75.88	141.63	209.25
	Feed compressors	70.79	70.79	70.79
	Feed heaters	10.86	28.74	40.66
	Reactor cooling jackets	22.53	41.97	55.41

Energy consumption (MW)	Syncrude coolers	43.20	73.87	94.35
	Flash drums	0.57	1.05	1.38
	Heat losses (5%)	7.40	10.82	13.13
Conversion (%)	CO_2	34.00	56.63	71.54
	CO	85.35	92.94	96.18
Gasoline yield (%)		24.78	41.55	52.48
CO_2-FTS process efficiency (%)		38.96	53.12	66.41

These results are in good agreement with experimental findings using 2-stage (Guo et al., 2018) and 3-stage (Landau et al., 2014) fixed-bed reactors for direct CO_2 conversion into C_{5+} hydrocarbons. The authors explained that water removal accelerates the formation of active carbide phases which are crucial for CO_2-FTS activity. Since RWGS reaction rates and modified ASF hydrocarbon distribution are quite similar in each CO_2-FTS reactor, the more CO_2-FTS reactors are set in series, the higher overall CO_2 conversion is achieved.

The analysis of CO_2-FTS energy consumption revealed that increasing the number of reactor units results in higher energy requirements for the overall process plant. Indeed, the 2-stage and 3-stage CO_2-FTS reactor systems respectively consumed 227.2 MW and 275.7 MW of energy which were 46.4% and 77.6% higher than the energy requirement of a single CO_2-FTS reactor unit. In both cases, syncrude coolers showed the highest energy consumption with a cumulative value of 168.2 MW. This corresponded to 32.5% (Figure 5.6a) and 34.2% (Figure 5.6b) of energy usage for the 2-stage and 3-stage CO_2-FTS reactor systems, respectively.
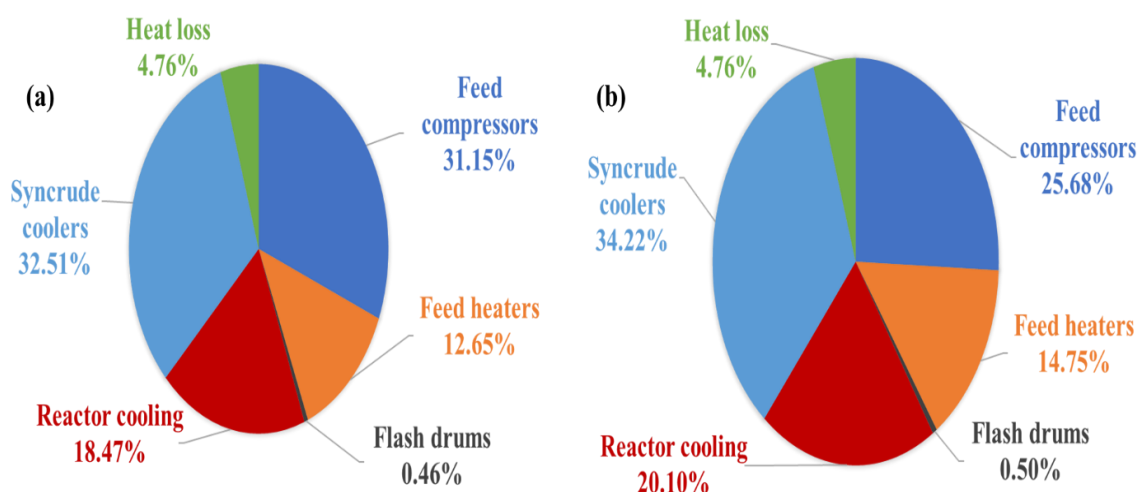
Figure 5.6: Energy repartition of (a) two-stage and (b) three-stage CO_2-FTS process to gasoline

The feed gas compressors had the second-highest share of energy consumption (31.2% and 25.7% of energy required in the 2-stage and 3-stage CO_2-FTS reactor systems respectively).

For the same inlet flowrates, Fernández-Torres et al. (2022) reported an energy consumption of 10.1 MW for the feed gas compression which is 85.8% lower than the one observed in this work. This is simply because their study assumed that the feed gases are available to the CO_2-FTS plant at 25 bar. Hence, lower energy was required to compress the inlet gases to the reactor's desired pressure. Under similar assumptions, the feed gas compressors in this study would only need 6.2% and 4.8% of the total energy required in the 2-stage and 3-stage CO_2-FTS reactor systems respectively.

On the other hand, multiple CO_2-FTS reactors in series also led to higher gasoline production rates. For example, the 2-stage CO_2-FTS reactor system achieved a gasoline production rate of 11.3 ton/hr leading to 53.1% process efficiency. Besides, the 3-stage CO_2-FTS reactor system reached 16.7 ton/hr gasoline production rate resulting in a process efficiency of 66.4% which is nearly twice that of the single CO_2-FTS reactor unit. Therefore, it is sensitive to conclude that multi-stage reactors coupled with periodical water removal can help to achieve high CO_2 conversion thus, higher gasoline yield and process efficiency.

5.5.4. CO_2-FTS process performance using a single reactor with recycle

5.5.4.1. Justification for this case study

The natural alternative to multiple reactors in series is water removal followed by material recirculation so that unconverted feedstock can be re-used within the single CO_2-FTS reactor itself. This technique aims to enhance the overall process efficiency while limiting the net material consumption (Cinti et al., 2016). Since increasing the number of reactors showed noticeable effects on the CO_2-FTS process performance for gasoline synthesis, it is paramount to also understand the effects of material recycling (hence, recycle ratio) using a single CO_2-FTS reactor on CO_2 conversion, gasoline yield, energy consumption and process efficiency.

5.5.4.2. Process simulation of CO_2-FTS process to gasoline fuel using a single reactor with recycle

The configuration concept and flowsheet diagram of the CO_2-FTS process to gasoline using a single reactor with recycle developed in Aspen Plus® software is illustrated in Figure 5.7. The top exit stream (L-GAS2) of the separator is first split into two flows (RECYCLE and L-GAS3 streams). Given the high cost of hydrogen, it is assumed that the L-GAS3 stream will be sent to an upgrade section so that excess/unreacted H_2 can be recovered for on or off-site purposes which could allow the plant to be more efficient. Although the H_2 recovery section is outside of the scope of this research, the HHV of H_2 was considered in the process efficiency

calculation (Equation 5.20). Good discussions on H_2 recovery during FTS process can be found in Selvatico et al. (2016).
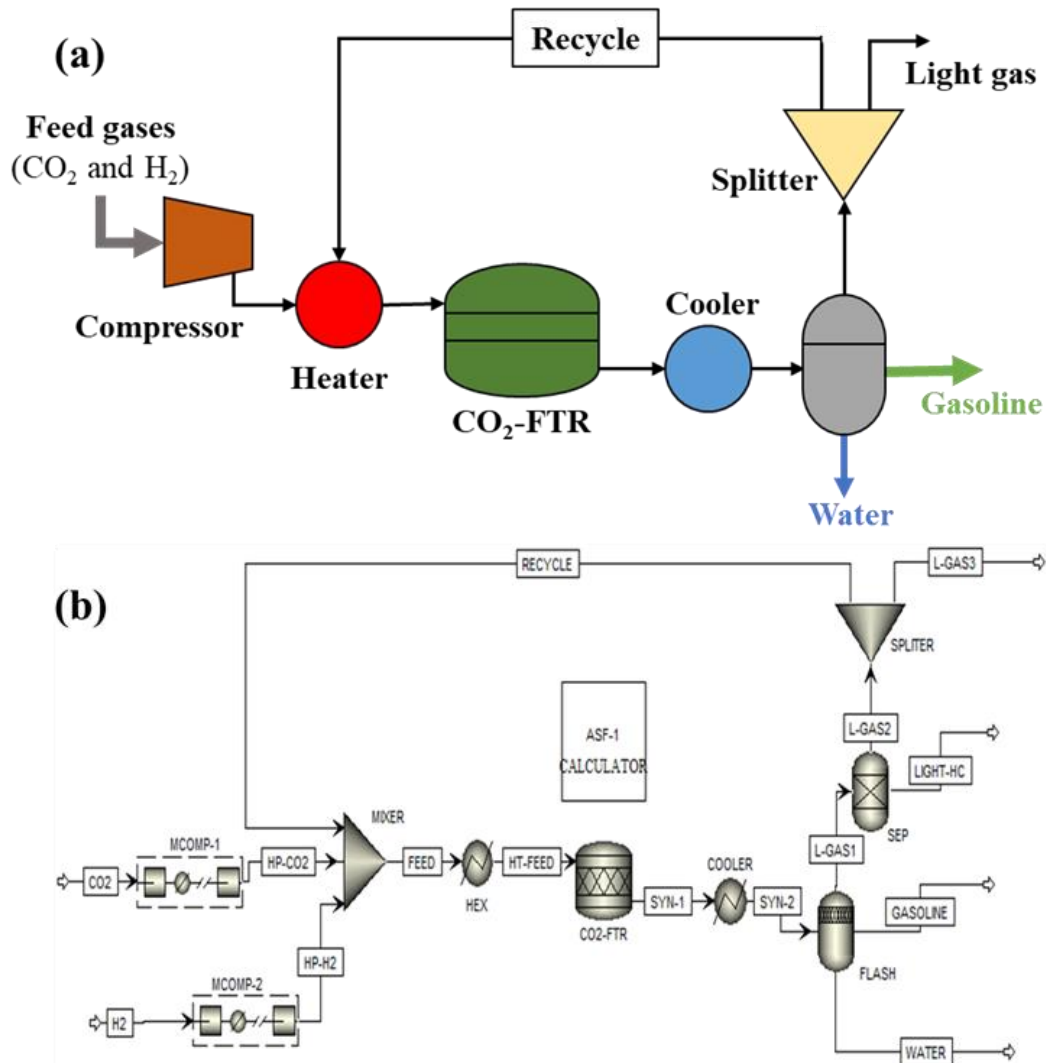
Figure 5.7: (a) Configuration concept and (b) process simulation of CO_2-FTS to gasoline using a single reactor with recycle

The RECYCLE stream (mostly containing H_2, CO and CO_2) is then sent to the feed mixer where it is combined with high-pressure CO_2 and H_2 feed streams. The remaining steps of the CO_2-FTS process to gasoline are as described in sections 5.5.2 and 5.5.3 for a single CO_2-FTS reactor unit. The recycle ratio (split fraction in the SPLITTER block) was initially set to 0.5. The sensitivity analysis tool was then used in Aspen Plus® to assess the effects of the recycle ratio on CO_2 conversion and gasoline production.

5.5.4.3. Performance analysis of CO_2-FTS process to gasoline fuel using a single with recycle

The results provided in this section were obtained under the operating conditions presented in Table 5.3 for the H_2/CO_2 ratio of 3.0 using CO_2 and H_2 inlet flowrates of 110.02 and 15.12 ton/hr respectively. The recycle ratio varied from 0.0 to 0.9 given that not all unconverted reactants can be recycled back to the reactor. Indeed, for recycle ratios above 0.9, the sensitivity analysis results showed errors. This is because the system was no longer in mass balance due to CO_2 accumulation and its equilibrium conversion limitations (Grim et al., 2020).

Figure 5.8 illustrates the effects of the recycle ratio on CO_2 conversion and gasoline yield. Although CO_2 conversion per pass through the reactor was set to 0.34 as per input data (Table 5.3), the results showed a considerable increase in CO_2 conversion of the configured plant (therefore, gasoline yield) with the recycle ratio. CO_2 conversion of the configured plant was calculated using Equation (5.21) and based on CO_2 molar flowrate in the inlet and L-GAS3 streams. Recirculating 90% of unconverted reactants achieved 83.9% CO_2 conversion which corresponded to roughly 61.2% gasoline yield.
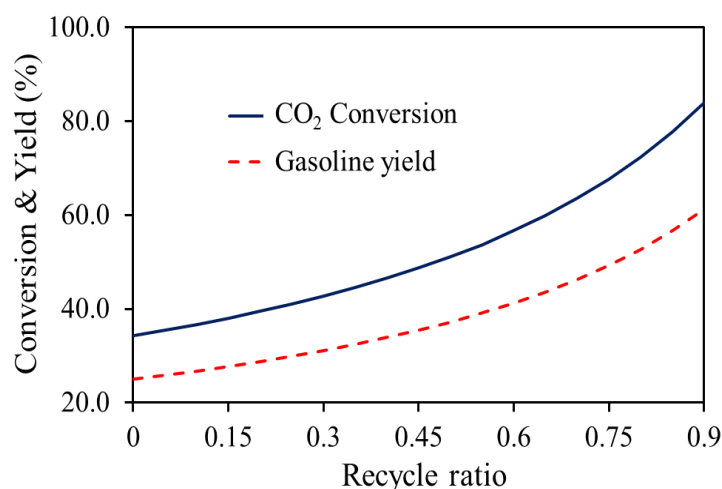
Figure 5.8: Effects of the recycle ratio on CO_2 conversion and gasoline yield during CO_2-FTS process

The performance summary of the CO_2-FTS process to gasoline using a single reactor (preliminary plant) compared to a single reactor with a recycle ratio of 0.9 (recycle system) is detailed in Table 5.7. It was found that the recycle system requires approximately 2.1 times more energy than the preliminary plant. The highest energy consumption of 112.4 MW was from the cooler located next to the CO_2-FTS reactor. This is simply due to the higher production rate observed in the recycle system. As a matter of fact, the gasoline production rate in the recycle system was close to 20.0 ton/hr (with a CO_2-FTS process efficiency of 69.6%) which

is more than 3 times that of the preliminary plant. Hence, water removal followed by reactant recirculation can effectively improve both CO_2 conversion and CO_2-FTS process efficiency.

Table 5.7: Performance summary of the CO_2-FTS process using single reactor compared to single reactor with recycle

Parameter		Preliminary plant	Recycle system
Gasoline fuel features	Mass flowrate (ton/hr)	6.07	19.97
	Density (kg/m^3)	767.13	765.34
	HHV (MW)	75.88	249.63
Energy consumption (MW)	Feed compressors	70.79	70.79
	Feed heaters	10.86	51.56
	Reactor cooling jackets	22.53	66.84
	Syncrude coolers	43.20	112.42
	Flash drums	0.57	2.28
	Heat losses (5%)	7.40	15.19
Conversion (%)	CO_2	71.54	83.94
	CO	85.35	98.33
Gasoline yield (%)		24.78	61.18
CO_2-FTS process efficiency (%)		38.96	69.64

5.5.5. CO_2-FTS process performance comparison between a single reactor with recycle and multiple reactors in series

The configured CO_2-FTS plants elaborated above, a single reactor with recycle and multiple reactors in series, have demonstrated the essential feature of enhancing CO_2 conversion and gasoline yield through ex-situ water removal from the system. A performance comparison between the two configuration systems (Table 5.8) indicated that the single reactor with recycle (recycle ratio of 0.9) has a higher gasoline production rate than the three-stage reactors in series (20.0 and 16.7 ton/hr, respectively). Although the recycle system required roughly 1.2 times more energy than the three-stage reactors in series, it achieved a higher process efficiency of 69.6% due to increased gasoline production. A possible explanation could be the higher CO_2 conversion observed in the recycle system which also led to a higher gasoline yield.

Table 5.8: CO_2-FTS process performance comparison between three reactors in series and single reactor with recycle

Parameter		Three reactors in series	Single reactor with recycle ratio of 0.9
Gasoline fuel features	Mass flowrate (ton/hr)	16.74	19.97
	Density (kg/m^3)	765.77	765.34
	HHV (MW)	209.25	249.63
Energy requirement (MW)	Feed compressors	70.79	70.79
	Feed heaters	40.66	51.56
	Reactor cooling jackets	55.41	66.84
	Syncrude coolers	94.35	112.42
	Flash drums	1.38	2.28
	Heat losses (5%)	13.13	15.19
Conversion (%)	CO_2	71.54	83.94
	CO	96.18	98.33
Gasoline yield (%)		52.48	61.18
CO_2-FTS process efficiency (%)		66.41	69.64

However, it was previously demonstrated that the more CO_2-FTS reactors are set in series, the higher CO_2 conversion is achieved whereas, a lower recycle ratio would result in lower CO_2 conversion. Therefore, the two configuration systems were also compared at the same CO_2 conversion to identify which one would provide the best performance. The three reactors in series achieved a CO_2 conversion of 71.5% hence, a recycle ratio of 0.8 was chosen (based on Figure 5.8) to maintain the same CO_2 conversion in the recycle system.

Figure 5.9 depicts the overall mass balance and energy consumption of direct CO_2-FTS processes to gasoline fuel using multiple reactors in series (Figure 5.9a) and a single reactor with recycle (Figure 5.9b) for the same CO_2 conversion of 71.5%. It can be seen that the gasoline production rate for both CO_2-FTS process plants is quite similar (16.74 and 16.94 ton/hr for the 3-stage reactor in series and single reactor with recycle respectively).
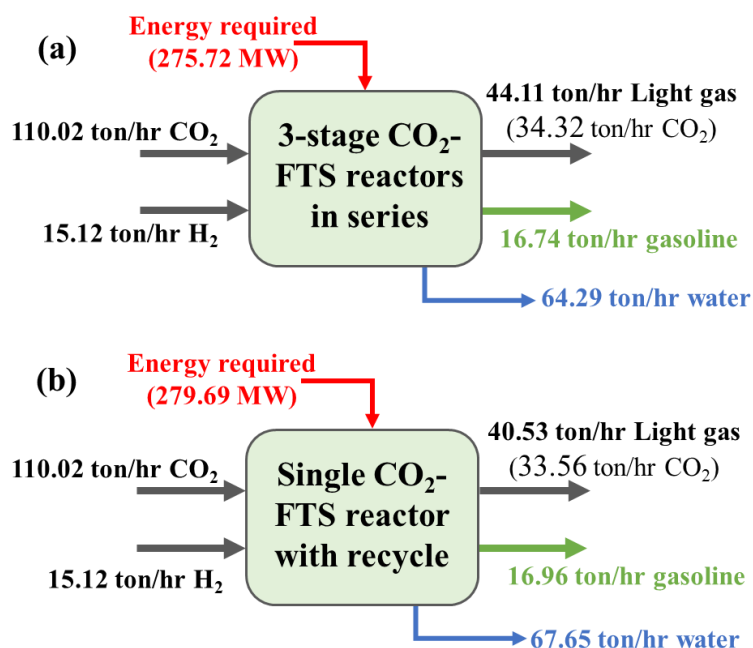
Figure 5.9: Overall material mass balance and required energy of CO_2-FTS process using (a) three reactors in series and (b) single reactor with recycle for 71.5% CO_2 conversion

Although the recycle system had a slightly higher energy requirement than the 3-stage reactor in series (279.69 and 275.72 MW, respectively), similar CO_2-FTS process efficiency of roughly 66.4% was found for both systems. Hence, in terms of CO_2 conversion and process efficiency, both configuration plants can effectively improve the CO_2-FTS process performance with more than 52% gasoline yield. In industrial applications, this could reduce the operating costs for the disposal of by-products and/or management of unconverted reactants.

5.6. Conclusion

In this Chapter, a steady-state CO_2-FTS model was developed and validated in Aspen Plus® using Fortran® routines. The model is based on first principles and a modified ASF distribution to predict gasoline range hydrocarbons (C_5-C_{11}). Model validation was performed for two sets of data with H_2/CO_2 feed ratios of 1.0 and 3.0. Good agreements were found between model predictions and experimental data with relative errors below 9.0%. Data for model validation were obtained from (Wei et al., 2017). Two CO_2-FTS process configurations for ex-situ water removal (including a three-stage reactor in series and a single reactor with recycle) were considered and their process performances were analysed and compared in terms of CO_2 conversion, gasoline yield, energy consumption and process efficiency.

Both CO_2-FTS process plants showed significant improvements in CO_2 conversion (from 34 to above 70%) and gasoline yield (from 25 to over 52%) through ex-situ water removal from

the system. A comparative analysis between the two direct CO_2-FTS process plants indicated that the single reactor with recycle (recycle ratio of 0.9) has a higher gasoline yield (around 61.0%) and gasoline production rate (roughly 20.0 ton/hr) than the 3-stage reactor in series due to higher CO_2 conversion (about 84.0%).

Although the 3-stage reactor in series showed a lower energy requirement than the single reactor with recycle (275.7 and 319.1 MW, respectively), it achieved a lower process efficiency of 66.4% due to lower gasoline production rates. However, the performance analysis at the same CO_2 conversion of 71.5% revealed that both process configurations have a similar process efficiency of around 66.4%. Therefore, under the investigated conditions, both CO_2-FTS process plants can successfully achieve higher gasoline yield and process efficiency.

6. Comparative analysis between direct CO$_2$-FTS and integrated SOEC-FTS processes for gasoline fuel synthesis

6.1. Introduction

In the Power-to-fuels concept, CO$_2$ can be recycled and re-used for the synthesis of useful fuels so that net-zero CO$_2$ emissions can be achieved (Rosa, 2017; de Vasconcelos et al., 2019). It was demonstrated in Chapter 5 that CO$_2$ can be directly converted into gasoline fuel in a one-step process through the modified CO$_2$-FTS route. However, the traditional FTS process uses syngas as a feedstock for the synthesis of liquid fuels. In the perspective of making this process more environmentally friendly, syngas must be produced from sustainable processes such as CO$_2$/H$_2$O co-electrolysis in SOECs using renewable electricity. Despite considerable progress in both technologies, a systematic comparison between the two CO$_2$-to-gasoline processes remains scarce.

As a result, this Chapter aims to compare the traditional FTS process integrated with SOEC and the direct CO$_2$-FTS process for gasoline fuel synthesis. Section 6.2 focuses on the simulation of the FTS process integrated with SOEC for syngas production. The performance of the integrated SOEC-FTS process to gasoline fuel is analysed in Section 6.3. Finally, Section 6.4 elaborates the comparative analysis between integrated SOEC-FTS and direct CO$_2$-FTS processes to gasoline fuel.

6.2. Process simulation of integrated SOEC-FTS process for gasoline fuel synthesis

6.2.1. Modelling/simulation assumptions and considerations

The integrated SOEC-FTS process to gasoline fuel was simulated with the following assumptions:

- Both SOEC and FTS processes operate at steady-state conditions i.e. the accumulation of mass and/or heat was not considered.

- SOEC-FTS process simulation was performed in Aspen Plus® software using Peng-Robinson as the property method.

- The component materials of the SOEC unit are the same as the improved material designed and elaborated in Chapter 4. Therefore, a constant degradation rate of 0.89 %/1000hrs was assumed for the SOEC unit.

- Inlet gases and water at the cathode and anode electrodes were assumed to be available at standard conditions. Hence, a pre-treatment step was required to bring the reactants to the desired SOEC operating conditions.

- It was assumed that FTS product distribution follows the modified ASF distribution model developed and validated for $Na-Fe_3O_4$/HZSM-5 catalyst using FBR in Chapter 5. This is because $Na-Fe_3O_4$/HZSM-5 catalyst was developed for both CO_2 reduction to CO and CO hydrogenation to hydrocarbons via the RWGS reaction and FTS process respectively (Wei et al., 2017).

6.2.2. SOEC-FTS process simulation

Figure 6.1 shows the flowsheet of the integrated SOEC-FTS process to gasoline fuel developed in this study. The integrated system consists of four stages including feed gas pre-treatment, SOEC unit (green block), syngas pre-treatment and FTS unit (red block).

H_2O inlet stream is first heated to generate steam which is then mixed with the FEED-1 stream obtained from the mixture of CO_2 and H_2 streams. The resulting stream (FEED-2) is further heated to SOEC operating temperature before entering the SOEC unit. All inlet streams were available at a standard pressure of 1.0 bar which is the desired SOEC operating pressure as explained in Section 4.2. Therefore, the compression of feed streams was not required. The heated FEED-3 stream then enters the SOEC unit which operates as elaborated in Section 3.3. At the anode electrode, the sweep air (ANOD-IN) stream was also heated to SOEC operating temperature prior to mixing with the O_2-OUT stream leaving the separator block (ELEC-SEP).

Between SOEC and FTS sections, some auxiliary operation units (including a cooler and condenser) were necessary for water removal from syngas. The removal of unconverted water and/or water produced from the RWGS Reaction (3.39) is required for various reasons, for instance, the presence of water in the inlet stream decreases the compressor work and high water content leads to degradation of FTS catalysts thus, lowers the process efficiency (Cinti et al., 2016).
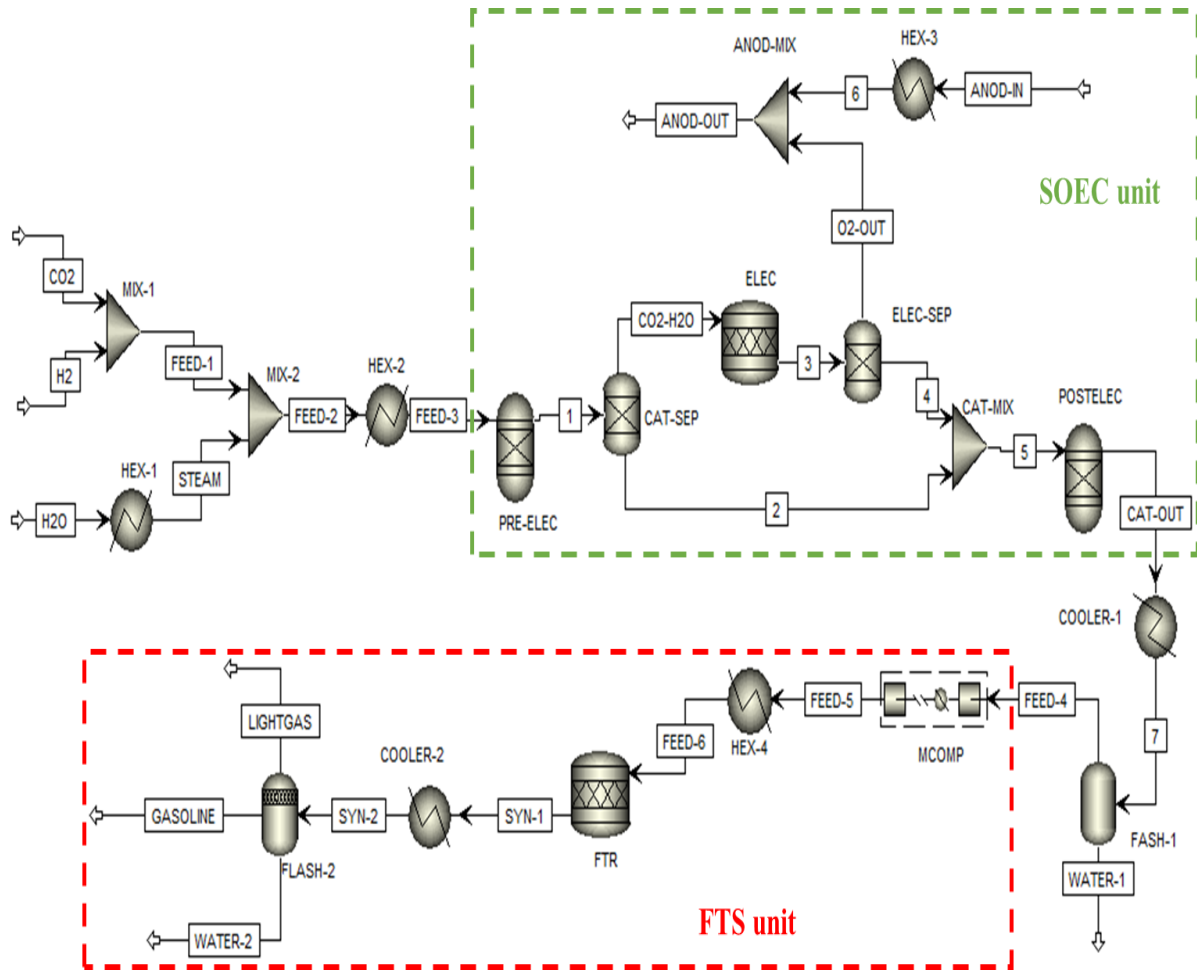
Figure 6.1: Flowsheet of integrated SOEC-FTS process to gasoline fuel in Aspen Plus®

Therefore, the produced syngas (CAT-OUT stream) exiting the SOEC unit is first cooled down then water is condensed out using a two-phase outlet flash block (FLASH-1). The resulting dry syngas stream (FEED-4) is then sent to the FTS unit for gasoline fuel synthesis. The FTS unit is somewhat similar to the CO_2-FTS unit described in Section 5.3. The main differences are the inlet gas composition and the calculation of the total molar extent of produced hydrocarbons.

$$\dot{N}_{HC} = X_{CO} \times \left(\left(X_{CO_2} \times \dot{n}_{CO_{2in}} \right) + \dot{n}_{CO} \right) \tag{6.1}$$

Unlike the CO_2-FTS unit, the feed stream (FEED-4) contains H_2, CO and unconverted CO_2. Equation (6.1), instead of Equation (5.18), was used to evaluate the total molar extent of produced hydrocarbons. Equation (6.1) accounts for the CO compound present in the inlet stream and is based on the stoichiometry and carbon mole balance of the RWGS and FTS reactions detailed in Table 5.1. Similar to the CO_2-FTR block (Figure 5.2), the FTR block

(Figure 6.1) accomplishes all chemical reactions elaborated in Table 5.1 and Fortran® routines assess the molar extent of each reaction. The remaining steps of gasoline fuel synthesis are the same as described in Section 5.5.2.

6.3. Performance analysis of integrated SOEC-FTS process for gasoline fuel synthesis

6.3.1. Assumptions, set-up and evaluation criteria for SOEC-FTS performance analysis

Performance analysis of the integrated SOEC-FTS process was carried out based on the following considerations:

- SOEC model was validated in Section 3.4. The FTS process follows the modified ASF distribution model which was validated in Section 5.4. Hence, the integrated SOEC-FTS process was deemed accurate enough for performance analysis.

- SOEC-FTS performance analysis is given in terms of gasoline production rate, required energy and SOEC, FTS and overall SOEC-FTS efficiencies.

- The efficiency parameters are based on HHV values and were calculated using Equations (6.2) to (6.5). Heat losses to SOEC and FTS sections remained the same as discussed in Chapters 4 and 5 respectively. It is paramount to distinguish between syngas production efficiency and SOEC efficiency. The syngas production efficiency (η_{syngas}) assessed in Chapter 4 using Equation (4.2) considers only H₂ and CO mole fractions in the produced syngas whereas, the SOEC efficiency analysed in this Chapter (Equation 6.2) takes into consideration the production rate of syngas leaving the SOEC unit.

$$\eta_{SOEC} = \frac{HHV_{cat,out}}{HHV_{cat,in} + \mathcal{P}_{SOEC} + P_{Aux,SOEC}} \qquad (6.2)$$

$$\mathcal{P}_{SOEC} = U \times j \times A_{tot} \qquad (6.3)$$

$$\eta_{FTS} = \frac{HHV_{gasoline}}{HHV_{syngas} + \mathcal{P}_{FTS}} \qquad (6.4)$$

$$\eta_{tot} = \frac{HHV_{gasoline}}{HHV_{cat,in} + \mathcal{P}_{SOEC} + \mathcal{P}_{FTS} + \mathcal{P}_{Aux}} \qquad (6.5)$$

- Table 6.1 recapitulates the input parameters of the integrated SOEC-FTS process to gasoline fuel. SOEC temperature, pressure, current density and inlet feed composition were set based on process analysis carried out in Chapter 4. FTS operating conditions were chosen based on Na-Fe_3O_4/HZSM-5 catalyst features as elaborated by Wei et al. (2017).

Table 6.1: Input parameters for the integrated SOEC-FTS process to gasoline fuel

Parameter		Value
SOEC section	Cathode feed composition: CO_2/H_2O/H_2 (%mol)	30/60/10
	Cathode inlet flowrate (ton/hr)	242.14
	Anode feed composition: N_2/O_2 (%mol)	79/21
	Anode flowrate (ton/hr)	134.29
	Inlet feed pressure (bar)	1.0
	Inlet feed temperature (℃)	25
	Operating pressure (bar)	1.0
	Operating temperature (℃)	750
	Current density (A/cm^2)	1.5
	Cell size (cm^2)	12×12
	Active cell area (cm^2)	92.16
FTS section	Operating pressure (bar)	30
	Operating temperature (℃)	320
	CO_2 conversion	0.34
	α, α_1 and α_2 hydrocarbon growth probabilities	0.7, 0.75 and 0.82
	Cooling temperature (℃)	40

- CO_2 inlet flowrate was assumed to be 132.03 ton/hr. This value was chosen based on parametric studies on large-scale syngas production using SOEC systems and to satisfy a FTS commercial capacity of 5,000 bbl/day (O'Brien et al., 2009; Al-kalbani et al., 2016; Banerjee et al., 2018). Therefore, successful scale-up of SOEC rigs was also assumed. A design specification was then used to achieve a cathode inlet composition of 30%CO_2/60%H_2O/10%H_2 (in mole%) by varying H_2O and H_2 inlet flowrates.

- The molar composition of the sweep air at the anode electrode was assumed to be 21% O_2 and 79% N_2. Its inlet flowrate was also obtained using a design specification to achieve an O_2 mole fraction of 0.5 in the ANOD-OUT stream (Figure 6.1)

- SOEC remaining characteristics were the same as detailed in Table 3.4. However, the number of cells was adjusted following Faraday's law (Equation 3.40) to maintain a reactant conversion of 60% as per experimental data from DTU Energy Conversion (Ebbesen et al., 2011; Sun et al., 2013).

6.3.2. Performance analysis of SOEC-FTS process

The results presented in this section were obtained under the operating conditions detailed in Table 6.1. The overall material balance and required energy of the SOEC-FTS process to gasoline fuel are displayed in Figure 6.2. After water removal, 131.9 ton/hr of syngas is fed to the FTS unit. The integrated SOEC-FTS plant requires a total energy of 929.5 MW to produce 24.4 and 54.7 ton/hr of gasoline fuel and light gas respectively. Table 6.2 details the breakdown of energy requirement for the integrated SOEC-FTS process.
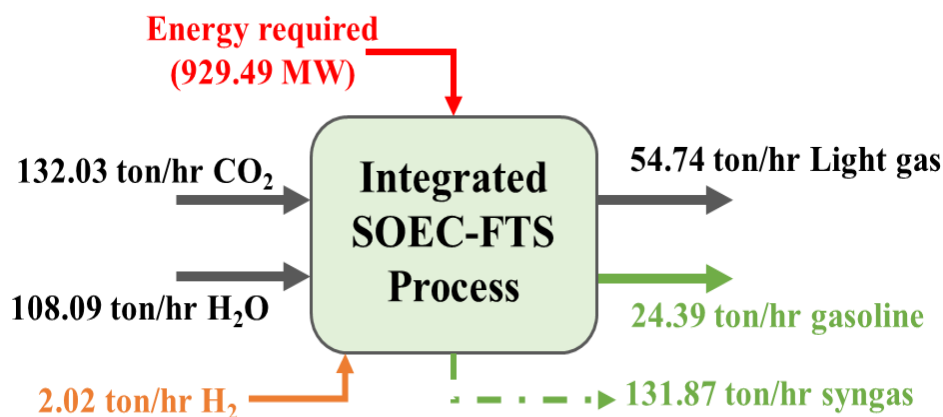
Figure 6.2: Overall material mass balance and energy requirement of the integrated SOEC-FTS process to gasoline fuel

Table 6.2: Performance summary of the integrated SOECFTS process to gasoline fuel

Parameter		Value
Syngas features	Mass flowrate (ton/hr)	131.87
	HHV (MW)	509.24
Gasoline fuel features	Mass flowrate (ton/hr)	24.39
	Density (kg/m³)	765.29
	HHV (MW)	304.88
	Cathode heaters	156.26

Energy required in SOEC section (MW)	Anode heater	29.09
	SOEC required power	382.19
	Syngas cooler	90.31
	Heat losses (10%)	65.79
Energy required in FTS section (MW)	Syngas compressor	58.63
	Syngas heater	6.51
	Reactor cooling jacket	77.81
	Syncrude cooler	49.13
	Flash drums	3.97
	Heat loss (5%)	9.80
Efficiencies (%)	SOEC	70.37
	FTS	42.63
	SOEC-FTS	32.81

The analysis of the energy requirement for the SOEC-FTS process indicated that the SOEC section requires roughly 3.5 times more energy than the FTS section. This is due to the power consumption of 382.2 MW by the SOEC unit which corresponds to 41.3% of the total energy requirement (Figure 6.3). The heating and cooling systems also contribute significantly to the energy demand with a cumulative share of 35.8%.
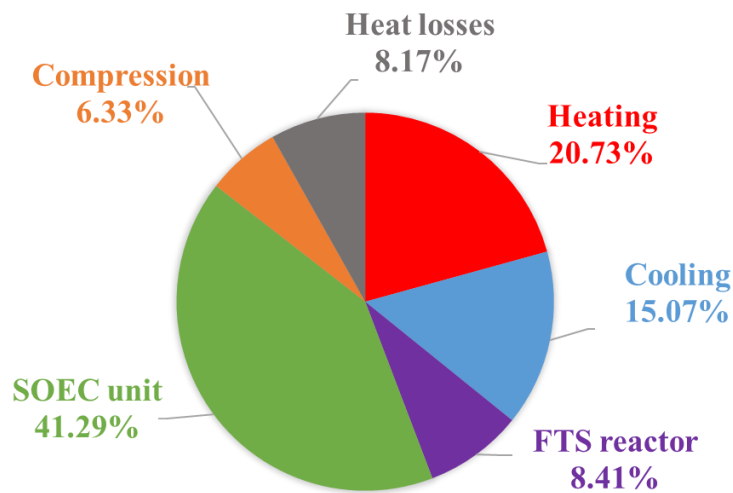
Figure 6.3: Energy repartition of integrated SOEC-FTS process to gasoline fuel

The high power consumption in the SOEC unit results from the high required number of cells. As explained above, the number of cells in the SOEC unit was adjusted to achieve a reactant conversion of 60% for a cathode feed flowrate of 242.1 ton/hr. This led to a required 2.09×10^6 cells for a current density of 1.5 A/cm^2. Although this value is much higher than that of the world's largest SOEC module with 1.08×10^5 cells (Dicke, 2021), it is between the range values

of cells required (0.87 to 3.49×10^6) for large-scale implementation of SOEC plants (O'Brien et al., 2009; Hauch et al., 2020).

Table 6.2 also details the efficiencies calculated according to the definition aforementioned. SOEC, FTS and total efficiencies were evaluated at 70.4%, 42.6% and 32.8% respectively. Among these values, SOEC efficiency is lower than the ones found in previous studies on the SOEC-FTS process as shown in Table 6.3. However, the results from literature data do not account for SOEC degradation. When the fixed degradation rate of 0.89 %/1000hrs was not considered, the required SOEC power became 303.8 MW leading to 79.9% SOEC efficiency which was almost comparable to the literature data. Furthermore, Wang et al. (2019) reported a decrease in SOEC efficiency from 83.6 to 65.0% when assuming a constant degradation rate of 1.40 %/1000hrs. Therefore, accounting for SOEC rate of degradation gives a much better approximation of the efficiency.

Table 6.3: Comparison of SOEC efficiency between this research and literature data

SOEC efficiency (%)	Reference
70.4	This study
80.9	(Becker et al., 2012)
79.0	(Cinti et al., 2016)
80.3	(Herz et al., 2018)
83.6	(Wang et al., 2019)

6.3.3. Performance analysis of SOEC-FTS process with material recirculation

6.3.3.1. Justification for this case study

The integrated SOEC-FTS process gasoline fuel achieved a total efficiency of 32.8% (36.2% without considering SOEC degradation) as presented in Table 6.2. It was demonstrated in Section 5.5.4 that light gas recirculation is of upmost importance to improve the overall process efficiency. Moreover, the light gas stream leaving the FTS section (Figure 6.1) contains high mole fractions of unconverted reactants (42.8%, 18.2% and 25.7% of CO_2, CO and H_2 respectively). Hence, material recirculation was carried out to assess its influence on the performance of the integrated SOEC-FTS process.

6.3.3.2. Process simulation of integrated SOEC-FTS system with material recirculation

The flowsheet diagram of the integrated SOEC-FTS process to gasoline with material recirculation developed in Aspen Plus® software is illustrated in Figure 6.4. The concept of material recycle was the same as discussed in Section 5.5.4. Unconverted reactants are first removed from the light gas stream (L-GAS1) using a separator block (FTS-SEP). The resulting stream is then split into two flows and the RECYCLE stream is mixed with the compressed syngas (FEED-5). Finally, the FEED-7 stream is heated and sent to the FTR block.

Figure 6.4: Process simulation of SOEC-FTS process to gasoline with material recirculation

6.3.3.3. Performance analysis integrated SOEC-FTS system with recycle

The results provided in this section were obtained under the operating conditions presented in Table 6.1 with a recycle ratio of 0.7. For recycle ratios higher than 0.7, Aspen Plus® results showed errors due to deficit in H_2 and excess of CO_2 and CO compounds. Thus, 0.7 was chosen as the adequate recycle ratio. The performance summary of the integrated SOEC-FTS process

to gasoline using a single FTS reactor (open-loop system) compared to the FTS reactor with a recycle (recycle system) is detailed in Table 6.4.

As observed in Table 6.4, the production rate, energy required and efficiency in the SOEC section remained the same. This is simply because no changes were made to the SOEC operating conditions and characteristics. On the other hand, the FTS section showed an increase in power consumption from 205.8 MW in the open-loop system to 255.6 MW in the recycle system. This was because of the increase in inlet flowrates to the heater of the FTS section (from 131.9 to 170.2 ton/hr).

Table 6.4: Performance summary of the SOEC-FTS process to gasoline fuel for an open-loop and recycle to FTS section

Parameter		Open-loop	Recycle
Syngas features	Mass flowrate (ton/hr)	131.87	131.87
	HHV (MW)	509.24	509.24
Gasoline fuel features	Mass flowrate (ton/hr)	24.39	35.21
	Density (kg/m^3)	765.29	765.18
	HHV (MW)	304.88	427.63
Energy required in SOEC section (MW)	Cathode heaters	156.26	156.26
	Anode heater	29.09	29.09
	SOEC required power	382.19	382.19
	Syngas cooler	90.31	90.31
	Heat losses (10%)	65.79	65.79
Energy required in FTS section (MW)	Syngas compressor	58.63	58.63
	Syngas heater	6.51	13.12
	Reactor cooling jacket	77.81	98.69
	Syncrude cooler	49.13	69.05
	Flash drums	3.97	3.97
	Heat loss (5%)	9.80	12.17
Efficiencies (%)	SOEC	70.37	70.37
	FTS	42.63	57.54
	SOEC-FTS	32.81	44.95

The increase in inlet feed flowrate also lead to higher production of gasoline fuel which reached 35.2 ton/hr because of the increased amount of reactants available for both RWGS and FTS reactions. As a result, the process efficiency in the FTS section also increased by approximately

35.0%. Since the energy consumption remained the same in the SOEC section, a higher overall SOEC-FTS efficiency of 44.9% (49.3% without SOEC degradation rate) was achieved due to the increase in the gasoline production rate.

6.4. Performance comparison between CO_2-FTS and SOEC-FTS processes for gasoline fuel synthesis

6.4.1. Considerations and set-up for this case study

The comparison of different system performances should be carried out either for a similar production capacity and/or under similar operating conditions (Wang et al., 2019). Therefore, the three CO_2-to-gasoline processes (integrated SOEC-FTS with recycle to the FTS section, and direct CO_2-FTS using reactors in series and using a single reactor with recycle) were compared for a gasoline production rate of 25.0 ton/hr. This scale corresponds to a representative size to assess the prospects of the green CO_2-to-gasoline process at industrial-scale (Fernández-Torres et al., 2022).

To carry out this comparative analysis, the following implementations were made in Aspen Plus® software:

- For the three CO_2-to-gasoline processes, a design specification was used to achieve a 25.0 ton/hr mass flowrate in the GASOLINE stream of Figures 5.5, 5.7 and 6.4 by varying the inlet CO_2 flowrate.

- For the two direct CO_2-FTS processes, another design specification was implemented to maintain a H_2/CO_2 ratio of 3.0 in FEED-1 and FEED streams of Figures 5.5 and 5.7, respectively by adjusting the H_2 inlet flowrate. Previous design specifications performed in the SOEC-FTS process remained the same.

- The recycle ratios of integrated SOEC-FTS and direct CO_2-FTS processes were respectively 0.7 and 0.9 based on previous results obtained in their corresponding sections.

- CO_2-FTS and FTS reactor operated at 320℃, 30 bar and using Na-Fe_3O_4/HZSM-5 catalyst. The remaining conditions were the same as shown in Tables 5.3 and 6.1.

- The remaining operating conditions in the SOEC section were the same as presented in Table 6.1.

6.4.2. Comparison of material flows, CO_2 conversion and gasoline yield

Figure 6.5 portrays the overall material balance of the three CO_2-to-gasoline processes considered in this research. It showed that to produce 25.0 ton/hr of gasoline, the integrated SOEC-FTS process with recycle to the FTS section requires the lowest inlet CO_2 flowrate of 107.4 ton/hr. Whereas, the single CO_2-FTS reactor with recycle and 3-stage CO_2-FTS reactors in series need respectively 137.5 and 164.3 ton/hr of CO_2 to achieve the same production rate. Similarly, the 3-stage CO_2-FTS reactor in series requires roughly 1.2 times more H_2 input than the single CO_2-FTS reactor with recycle to satisfy the design specification on H_2/CO_2 ratio in the FEED stream.
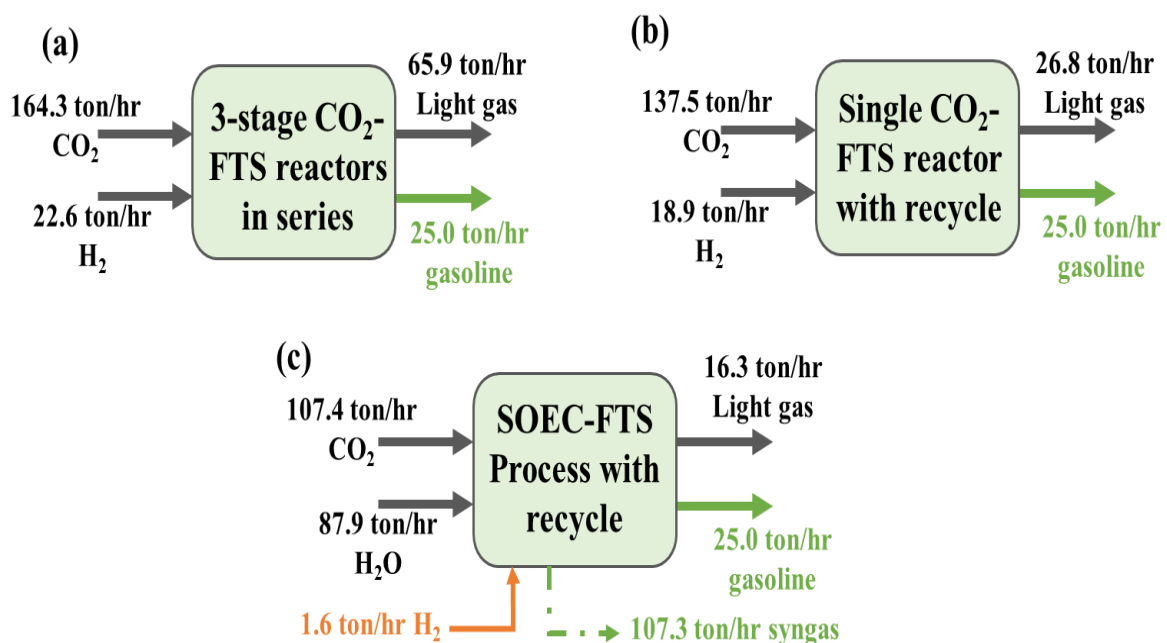
Figure 6.5: Overall material mass balance of the different CO_2-to-gasoline processes

The low inlet requirement by the SOEC-FTS system simply reflects the ability of SOECs to efficiently produce syngas together with the FTS process maturity using syngas which is fully implemented and commercialised on a global scale (Jarvis et al., 2018). On the other hand, the lower need for feed gases in the single CO_2-FTS reactor with recycle compared to the 3-stage CO_2-FTS reactors in series agrees with the principle of material recirculation which aims not only to improve the system efficiency but also to reduce the net consumption of reactants (Cinti, Baldinelli, et al., 2016; Herz et al., 2018).

Figure 6.6 displays the CO_2 conversion and gasoline yield obtained for the three CO_2-to-gasoline processes. CO_2 conversion and gasoline yield were calculated using Equations (5.21) and (5.20), respectively. All three processes achieved high CO_2 conversion and gasoline yield

above 70.0% and 50.0%, respectively. However, the highest CO_2 conversion and gasoline yield were observed for the integrated SOEC-FTS at approximately 87.6% and 64.0%, respectively. A possible explanation could be that in the integrated SOEC-FTS system, CO_2 is converted in both SOEC and FTS sections through electrochemical and RWGS, respectively.
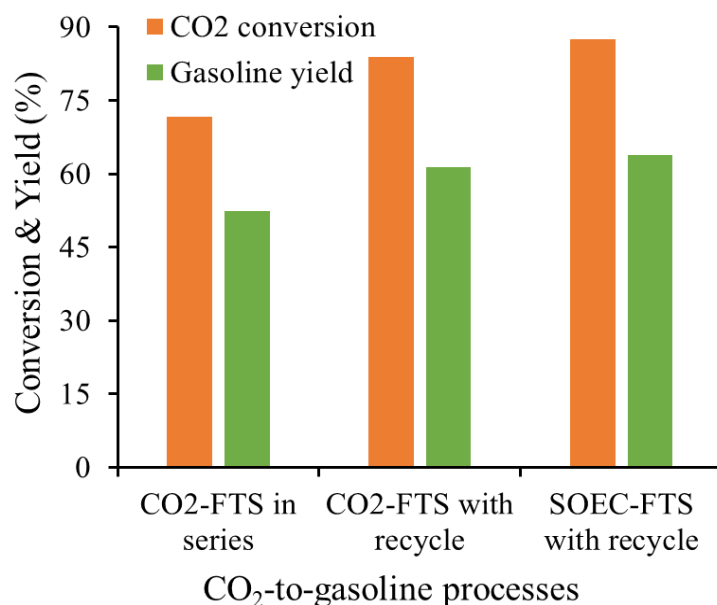
Figure 6.6: Comparison of CO_2 conversion and gasoline yield among the different CO_2-to-gasoline processes

6.4.3. Comparison of energy requirement

The total energy requirement of the different CO_2-to-gasoline processes was also analysed and their results are illustrated in Figure 6.7. Despite its low reactant requirement, the integrated SOEC-FTS process requires much more energy compared to the direct CO_2-FTS processes. To elaborate, the SOEC-FTS process consumed a total of 802.5 MW of energy to synthesise 25.0 ton/hr of gasoline (green bars in Figure 6.7). This corresponded to roughly 2.0 and 2.2 times more power consumption found for the 3-stage CO_2-FTS reactors in series and single CO_2-FTS reactor with recycle, respectively to achieve the same gasoline production rate.

The high power consumption in the SOEC-FTS process is essentially due to the energy demand in the SOEC section which was 3.0 times higher than that of the FTS section. In the comparative analysis above-mentioned, it was assumed that hydrogen for the direct CO_2-FTS processes was available under standard conditions to the plant. Therefore, the energy required for hydrogen production was not considered.
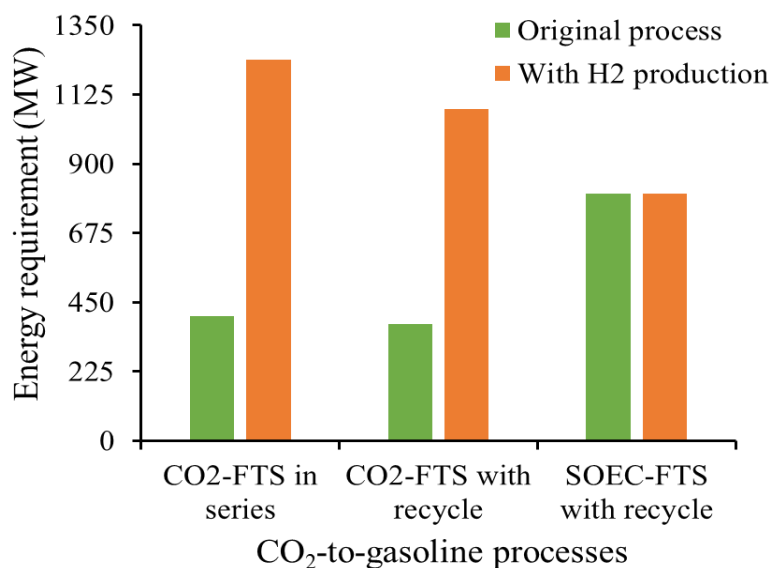
Figure 6.7: Comparison of energy requirement among the different CO_2-to-gasoline processes

Green H_2 production via water electrolysis using renewable electricity can be carried out using various types of electrolysers. Recent studies on electrolysers for green H_2 production demonstrated that low-temperature electrolysers (such as alkaline, AEM and PEM) have a power consumption rate of 0.055 MWh/kg of H_2. Whereas, SOEC systems showed an electric consumption rate of 0.037 MWh/kg of H_2 (Al-kalbani et al., 2016; Cavaliere et al., 2021).

Assuming that green H_2 is produced from water electrolysis using SOEC, the 3-stage CO_2-FTS reactors in series would need 835.5 MW of electricity to achieve a H_2 production rate of 22.6 ton/hr. Likewise, the single CO_2-FTS reactor with recycle would require 698.9 MW of electricity to produce 18.9 ton/hr of H_2. Taking these into consideration, the total energy requirement of the 3-stage CO_2-FTS reactors in series and single CO_2-FTS reactor with recycle were evaluated at 1,239.6 and 1,076.7 MW, respectively as portrayed in Figure 6.7 (orange bars).

6.4.4. Comparison of system efficiency

The overall system efficiency of the three CO_2-to-gasoline processes was also calculated according to the definitions given in their corresponding sections. Figure 6.8 shows the comparison of system efficiency among the CO_2-to-gasoline processes. Since the direct CO_2-FTS processes required the lowest energy consumption for a similar gasoline production rate, they naturally achieved the highest process efficiencies of 67.5% and 73.2% for the 3-stage CO_2-FTS reactors in series and single CO_2-FTS reactor with recycle, respectively (green bars in Figure 6.8). On the other hand, the integrated SOEC-FTS process efficiency reached 43.6%.

Furthermore, Wang et al. (2019) explained that the more chemical reactions and process steps are involved, the larger exergy destructions occur, hence resulting in lower overall process efficiencies. This would further justify the lowest system efficiency observed in the integrated SOEC-FTS process and the highest process efficiency achieved in the single CO_2-FTS reactor with recycle. The latter has the simplest process design.
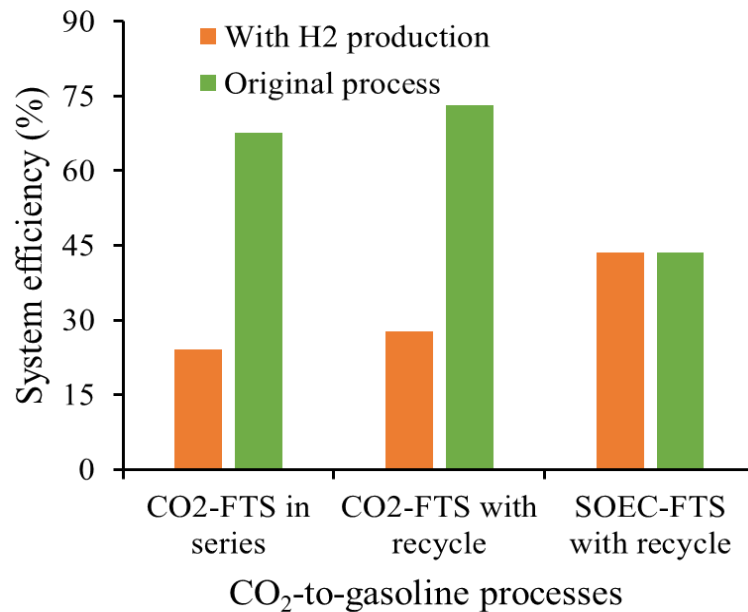
Figure 6.8: Comparison of system efficiency among the different CO_2-to-gasoline processes

Similarly, when considering the energy requirement for H_2 production in the direct CO_2-FTS processes, the overall process efficiency decreased from 67.5 to 25.2% and 73.2 to 29.0% for the 3-stage CO_2-FTS reactors in series and single CO_2-FTS reactor with recycle, respectively (orange bars in Figure 6.8). It is therefore sensitive to conclude that the successful implementation of the direct CO_2-FTS process into gasoline fuel highly depends on the availability and/or source of hydrogen.

6.5. Conclusion

In this Chapter, an integrated SOEC-FTS process for gasoline fuel synthesis was simulated in Aspen Plus® software. Performance analysis was then carried out for two configurations including an open-loop system and recycle system with material recirculation to the FTS section. Finally, a comparative analysis (in terms of reactant flowrates, CO_2 conversion, gasoline yield, energy requirement and overall system efficiency) was performed for three

CO_2-to-gasoline processes (integrated SOEC-FTS with recycle to the FTS section, and direct CO_2-FTS using reactors in series and using a single reactor with recycle).

The analysis of energy requirements showed that the SOEC section consumes 3 to 3.5 times more energy than the FTS section due to the high number of cells required. It was also observed that SOEC efficiency was quite lower than that of previous studies. This was simply because of the SOEC degradation rate considerations. The integrated SOEC-FTS process with recycle achieved a higher gasoline production rate than the open-loop system (35.2 and 24.4 ton/hr, respectively). This led to an overall process efficiency of 44.9% or 49.3% without considering SOEC degradation rate.

The comparative analysis among CO_2-to-gasoline processes indicated that the integrated SOEC-FTS process portrayed the highest CO_2 conversion and gasoline yield but achieved the lowest process efficiency of 43.6% for a gasoline production rate of 25.0 ton/hr. However, when considering the energy requirement for H_2 production, the process efficiency of the 3-stage CO_2-FTS reactors in series and single CO_2-FTS reactor with recycle considerably decreased by 62.7% and 60.4%, respectively. Therefore, commercial applications of direct CO_2-FTS process into gasoline fuel highly depend on the availability and/or source of hydrogen.

7. Conclusion and recommendations for future work

7.1. Conclusion

Power-to-fuels technologies have the potential to achieve CO_2 reductions targets through CO_2-neutral fuels. This research investigated CO_2 conversion into gasoline fuel through the CO_2-FTS process and FTS process integrated with SOEC for syngas synthesis. A critical review on CO_2/H_2O co-electrolysis to syngas using SOEC and liquid fuel synthesis via FTS and direct CO_2-FTS processes was carried out. The review assessed previous studies on SOEC, FTS and CO_2-FTS processes in different aspects including experimental lab, pilot and commercial rigs, modelling/simulation, optimisation and TEA. The extensive literature review revealed the following technical challenges and research gaps that needed to be addressed:

- Though SOEC degradation is still of concern for commercial deployment, no modelling studies were found integrating structural degradation of SOEC component materials during CO_2/H_2O co-electrolysis.

- Compared to the traditional FTS using syngas which showed 86.3% liquid fuel yield, the direct CO_2-FTS process only achieved a liquid fuel yield of 29.0% due to low CO_2 conversion arising from excessive water production from RWGS and FTS reactions.

- Existing modelling studies on direct CO_2-FTS process to liquid fuels are based on experimental data with up to 78% selectivity towards $C_1–C_4$ hydrocarbons which seriously compromises the accuracy of reported results.

Based on these findings, this research was divided into different tasks with a full scope including modelling, simulation, validation, optimisation and performance analysis of SOEC, CO_2-FTS and SOEC-FTS processes for syngas and gasoline fuel synthesis. The key conclusions for each process are given in the following sections.

7.1.1. Syngas production from CO_2/H_2O co-electrolysis using SOEC

A 1-D pseudo-dynamic model of SOEC operating under CO_2 and H_2O co-electrolysis mode was developed and implemented in Aspen Plus® using Fortran® routines. The model is based on first principles and incorporates electrochemical/chemical reactions, mass balance and particle diffusion/transport. In comparison to previous studies, the structural degradation of a

typical SOEC component materials (Ni-YSZ cathode, YSZ electrolyte and LSM-YSZ anode) was also accounted for. Furthermore, model validation was performed for both SOEC performance (syngas outlet composition) and degradation (operating voltage as a function of time) for different operating conditions including current densities, feed gas compositions and inlet flowrates.

The effects of operating conditions such as current density, temperature, inlet gas composition and cathode flowrate on syngas production efficiency and SOEC long-term performance were studied. The structural damages of cathode, anode and electrolyte materials as well as their contributions to the degradation of SOEC performance at high current densities were examined. Finally, material designs of SOEC components were investigated for the optimisation of SOEC long-term performance.

Long-term performance analysis revealed that SOEC degradation mostly arises from LSM-YSZ anode delamination with an average degradation rate of 3.96 %/1000hrs whereas, YSZ electrolyte degradation only affects SOEC electrochemical performance during the first 500 hours of operation and remains stable thereafter. Increasing the YSZ surface area at the cathode electrode as well as applying an anti-oxidant coating on the interconnect surface on the anode side and adjusting La/Sr ratio in LSM material can effectively decrease SOEC average degradation rate from 4.04 to 0.89%/1000hrs which is acceptable for commercial applications.

7.1.2. Gasoline fuel synthesis via the modified CO_2-FTS process

A CO_2-FTS model was developed and validated in Aspen Plus® using Fortran® routines. The model is based on first principles and a modified ASF distribution to predict gasoline range hydrocarbons (C_5-C_{11}). In comparison to previous studies, model validation was performed for two sets of data with H_2/CO_2 feed ratios of 1.0 and 3.0 with relative errors below 9.0%. Experimental data for model validation were obtained from Wei et al. (2017). Two process configurations for ex-situ water removal (including a three-stage reactor in series and a single reactor with recycle) were considered for performance analysis on CO_2 conversion, gasoline yield, energy requirement and process efficiency.

Both CO_2-FTS process plant configurations showed significant improvements in CO_2 conversion and up to 61.0% gasoline yield through ex-situ water removal from the system. A comparative analysis between the two direct CO_2-FTS process plants indicated that the single reactor with recycle (recycle ratio of 0.9) has a higher gasoline yield and gasoline production rate than the 3-stage reactor in series due to higher CO_2 conversion (about 84.0%). Although

the 3-stage reactor in series showed a lower energy requirement of 275.7 MW than the single reactor with recycle (319.1 MW), higher process efficiency was observed for the single reactor with recycle system due to higher gasoline production rates. However, the performance analysis at the same CO_2 conversion of 71.5% revealed that both process configurations have a similar process efficiency of roughly 66.4%. Therefore, under the investigated conditions, both CO_2-FTS process plants can successfully achieve higher gasoline yield and process efficiency.

7.1.3. Comparison between direct CO_2-FTS and integrated SOEC-FTS for gasoline fuel synthesis

An integrated SOEC-FTS process for gasoline fuel synthesis was simulated in Aspen Plus® software. Two configuration plants (an open-loop system and recycle system with material recirculation to the FTS section) were considered to carry out performance analysis and comparison. Finally, a comparative analysis (in terms of reactant flowrates, CO_2 conversion, gasoline yield, energy requirement and overall process efficiency) was performed between integrated SOEC-FTS with recycle to the FTS section and direct CO_2-FTS process using reactors in series and a single reactor with recycle.

It was found that the SOEC section consumes about 3 times more energy than the FTS section due to the high number of cells required. Moreover, SOEC efficiency was quite lower than that of previous studies arising from SOEC degradation rate considerations. The integrated SOEC-FTS process with recycle achieved a higher gasoline production rate than the open-loop system (35.2 and 24.4 ton/hr, respectively) leading to an overall process efficiency of 44.9% or 49.3% without considering SOEC degradation rate.

For a gasoline production rate of 25.0 ton/hr, the comparative analysis among CO_2-to-gasoline processes showed that the integrated SOEC-FTS process achieved the highest CO_2 conversion and gasoline yield but the lowest process efficiency of 43.6%. However, the process efficiency of the 3-stage CO_2-FTS reactors in series and single CO_2-FTS reactor with recycle considerably decreased from 67.5 to 25.2% and 73.2 to 29.0%, respectively when considering the energy requirement for H_2 production using SOECs. Therefore, commercial applications of direct CO_2-FTS process into gasoline fuel highly depend on H_2 availability and/or source.

From the aforementioned findings, it can be concluded that the aim and objectives of this research (as elaborated in Chapter 1 – Section 1.3) have been achieved.

7.2. Recommendations for future work

The following research areas are recommended for future work in the study of direct CO_2-FTS and integrated SOEC-FTS processes for the synthesis of gasoline fuel (or liquid fuels in general):

- CO_2-FTS model development was based on a modified ASF theory to predict gasoline range hydrocarbons as per experimental data from Wei et al. (2017). Although model predictions can describe the distribution of hydrocarbons fairly well, the ASF law does not provide further insights into CO_2-FTS reaction kinetics. Therefore, both experiment and modelling-based studies on the CO_2-FTS process to liquid fuels (or specifically to gasoline fuel) will be required to provide a deeper understanding of CO_2-FTS elementary reaction steps and the evolution of adsorption species and intermediates. Such studies could be based for example, on the Langmuir-Hinshelwood-Hougen-Watson (LHHW) mechanism model which has been successfully used in the traditional FTS process (Todic et al., 2013; Selvatico et al., 2016).

- In this research, SOEC degradation modelling and improvement through material design is limited to SOEC main components. Moreover, improved SOEC component materials have been tested during experiments for less than 1,500 hours. Hence, it will be interesting to investigate other sources of SOEC degradation such as degradation of sealing materials and mechanical failure (Yun Zheng et al., 2017) as well as to carry out SOEC experiments with the improved Ni-YSZ/YSZ/LSM-YSZ materials during long-term operation.

- Performance analysis of CO_2-FTS process using multiple reactors in series and single reactor with recycle showed promising results on liquid fuel yield and process efficiency for industrial applications. Furthermore, improved SOEC materials achieved an acceptable degradation rate for commercial deployments. An economic analysis should be carried out to fully assess the competitiveness of improved SOEC and CO_2-FTS processes compared to existing electrolysers and traditional FTS process, respectively. Moreover, further optimisation techniques such as heat integration will be also needed for energy management and efficiency.

- Power-to-fuels concept includes renewable electricity generation and storage, CO_2 capture, H_2 or syngas synthesis via H_2O electrolysis or CO_2/H_2O co-electrolysis and liquid fuel synthesis in the same place (Vázquez et al., 2018). However, this research focused on syngas and gasoline fuel synthesis from CO_2 and H_2O or H_2. Future studies should look into the

complete Power-to-fuels process so as to improve the entire system and assess how different sections interact and influence each other and the overall system efficiency.

- In this study, performance analysis and comparison of CO_2-to-gasoline processes were carried out at a commercial-scale under the assumptions of successful scale-up of catalysts and operation units from laboratory to commercial-scale. Therefore, model scale-up studies of CO_2-to-gasoline processes are required to provide further insights into plant operations and foresee any development at industrial-scale.

References

Abdullah, B., Abd Ghani, N. and Vo, D. N. (2017), Recent Advances in Dry Reforming of Methane over Ni-Based Catalysts. *Journal of Cleaner Production*, 162: 170–185.

Adeleke, A. A., Liu, X., Lu, X., Moyo, M. and Hildebrandt, D. (2020), Cobalt Hybrid Catalysts in Fischer-Tropsch Synthesis. *Reviews in Chemical Engineering*, 36(4): 437–457.

Agersted, K., Chen, M., Blennow, P. and Küngas, R. (2016), Long-Term Operation of a Solid Oxide Cell Stack for Co- Electrolysis of Steam and CO_2, 1–12, in: *12th European SOFC & SOE Forum [A0804] European Fuel Cell Forum*.

Al-kalbani, H., Xuan, J., García, S. and Wang, H. (2016), Comparative Energetic Assessment of Methanol Production from CO_2: Chemical versus Electrochemical Process. *Applied Energy*, 165: 1–13.

Al-Malah, I. (2016), *Aspen Plus®: Chemical Engineering Applications*. Hoboken, NJ, USA: John Wiley & Sons, Inc.

Alper, E. and Orhan, O. Y. (2017), CO_2 Utilization: Developments in Conversion Processes. *Petroleum*, 3: 109–126.

Ananyev, M. V., Farlenkov, A. S., Eremin, V. A. and Kurumchin, E. Kh (2018), Degradation Kinetics of LSM–YSZ Cathode Materials for SOFC. *International Journal of Hydrogen Energy*, 43: 951–959.

Aresta, M., Dibenedetto, A. and Angelini, A. (2014), Catalysis for the Valorization of Exhaust Carbon: From CO_2 to Chemicals, Materials, and Fuels. Technological Use of CO_2. *Chemical Reviews*, 114(3): 1709–1742.

Aresta, M., Dibenedetto, A. and Quaranta, E. (2016), State of the Art and Perspectives in Catalytic Processes for CO_2 Conversion into Chemicals and Fuels: The Distinctive Contribution of Chemical Catalysis and Biotechnology. *Journal of Catalysis*, 343: 2–45.

AspenTech (2022), Aspen Plus®: The Leading Process Simulation Software in the Chemical Industry. available at https://www.aspentech.com/en/products/engineering/aspen-plus [15 March 2022].

Azdarpour, A., Asadullah, M., Mohammadian, E., Hamidi, H., Junin, R. and Karaei, M.

(2015), A Review on Carbon Dioxide Mineral Carbonation through PH-Swing Process. *Chemical Engineering Journal*, 279: 615–630.

Banerjee, A., Wang, Y., Diercks, J. and Deutschmann, O. (2018), Hierarchical Modeling of Solid Oxide Cells and Stacks Producing Syngas via H_2O/CO_2 Co-Electrolysis for Industrial Applications. *Applied Energy*, 230: 996–1013.

Becker, W.L., Braun, R.J., Penev, M. and Melaina, M. (2012), Production of Fischer–Tropsch Liquid Fuels from High Temperature Solid Oxide Co-Electrolysis Units. *Energy*, 47(1): 99–115.

Bernadet, L., Laurencin, J., Roux, G., Montinaro, D., Mauvy, F. and Reytier, M. (2017), Effects of Pressure on High Temperature Steam and Carbon Dioxide Co-Electrolysis. *Electrochimica Acta*, 253: 114–127.

Boehm, R., Yang, H. and Yan, J. (2015), *Handbook of Clean Energy Systems – Volume 5: Energy Storage*. Chichester: Wiley.

Bogaerts, A., Snoeckx, R., Trenchev, G. and Wang, W. (2018), Modeling for a Better Understanding of Plasma-Based CO_2 Conversion, , in: *Plasma Chemistry and Gas Conversion*.

Botes, F G. (2009), Influences of Water and Syngas Partial Pressure on the Kinetics of a Commercial Alumina-Supported Cobalt Fischer - Tropsch Catalyst. *Industrial & Engineering Chemistry Research*, 48(4): 1859–1865.

Buttler, A., Koltun, R., Wolf, R. and Spliethoff, H. (2015), A Detailed Techno-Economic Analysis of Heat Integration in High Temperature Electrolysis for Efficient Hydrogen Production. *International Journal of Hydrogen Energy*, 40: 38–50.

Cano, L. A., Garcia Blanco, A. A., Lener, G., Marchetti, S. G. and Sapag, K. (2017), Effect of the Support and Promoters in Fischer-Tropsch Synthesis Using Supported Fe Catalysts. *Catalysis Today*, 282: 204–213.

Carbon Brief (2021), Global CO_2 Emissions Have Been Flat for a Decade, New Data Reveals. available at https://www.carbonbrief.org/global-co2-emissions-have-been-flat-for-a-decade-new-data-reveals [12 March 2022].

Cavaliere, P., Perrone, A. and Silvello, A. (2021), Water Electrolysis for the Production of Hydrogen to Be Employed in the Ironmaking and Steelmaking Industry. *Metals*, 11(11):

1816.

Chandra, V., Vogels, D., Peters, E. A.J.F. and Kuipers, J. A.M. (2021), A Multi-Scale Model for the Fischer-Tropsch Synthesis in a Wall-Cooled Packed Bed Reactor. *Chemical Engineering Journal*, 410: 128245.

Chatzichristodoulou, C., Chen, M., Hendriksen, P.V., Jacobsen, T. and Mogensen, M.B. (2016), Understanding Degradation of Solid Oxide Electrolysis Cells through Modeling of Electrochemical Potential Profiles. *Electrochimica Acta*, 189: 265–282.

Chen, B., Xu, H. and Ni, M. (2017), Modelling of SOEC-FT Reactor: Pressure Effects on Methanation Process. *Applied Energy*, 185: 814–824.

Chen, D., Lin, Z., Zhu, H. and Kee, R. J. (2009), Percolation Theory to Predict Effective Properties of Solid Oxide Fuel-Cell Composite Electrodes. *Journal of Power Sources*, 191: 240–252.

Chen, M., Høgh, J. V.T., Nielsen, J. U., Bentzen, J. J., Ebbesen, S. D. and Hendriksen, P. V. (2013), High Temperature Co-Electrolysis of Steam and CO_2 in an SOC Stack: Performance and Durability. *Fuel Cells*, 13(4): 638–645.

Chen, W., Kimpel, T. F., Song, Y., Chiang, F., Zijlstra, B., Pestman, R., Wang, P. and Hensen, E. J.M. (2018), Influence of Carbon Deposits on the Cobalt-Catalyzed Fischer-Tropsch Reaction: Evidence of a Two-Site Reaction Model. *ACS Catalysis*, 8: 1580–1590.

Chen, X., Guan, C., Xiao, G., Du, X. and W., Jian Qi. (2015), Syngas Production by High Temperature Steam/CO_2 Coelectrolysis Using Solid Oxide Electrolysis Cells. *Faraday Discussions*, 182: 341–351.

Cheng, K., Ordomsky, V. V., Legras, B., Virginie, M., Paul, S., Wang, Y. and Khodakov, A. (2015), Sodium-Promoted Iron Catalysts Prepared on Different Supports for High Temperature Fischer-Tropsch Synthesis. *Applied Catalysis A: General*, 502: 204–214.

Cheng, Y., Lin, J., Xu, K., Wang, H., Yao, X., Pei, Y., Yan, S., Qiao, M. and Zong, B. (2016), Fischer-Tropsch Synthesis to Lower Olefins over Potassium-Promoted Reduced Graphene Oxide Supported Iron Catalysts. *ACS Catalysis*, 6(1): 389–399.

Choi, Y., Jang, Y., Park, H., Kim, W., Lee, Y., Choi, S. and Lee, J. (2017), Carbon Dioxide Fischer-Tropsch Synthesis: A New Path to Carbon-Neutral Fuels. *Applied Catalysis B:*

Environmental, 202: 605–610.

Cinti, G., Baldinelli, A., Di M., A. and Desideri, U. (2016), Integration of Solid Oxide Electrolyzer and Fischer-Tropsch: A Sustainable Pathway for Synthetic Fuel. *Applied Energy*, 162: 308–320.

Cinti, G., Discepoli, G., Bidini, G., Lazini, A. and Santarelli, M. (2016), Co-electrolysis of Water and CO_2 in a Solid Oxide Electrolyzer (SOE) Stack. *International Journal of Energy Research*, 40: 207–215.

Clemmer, R.. and Corbin, S. F. (2009), The Influence of Pore and Ni Morphology on the Electrical Conductivity of Porous Ni/YSZ Composite Anodes for Use in Solid Oxide Fuel Cell Applications. *Solid State Ionics*, 180: 721–730.

CORDIS (2019), Efficient Co-Electrolyser for Efficient Renewable Energy Storage - ECo. available at https://cordis.europa.eu/project/id/699892 [6 March 2022].

Crank, J. (1975), *The Mathematics of Diffusion*. London: Oxford University Press.

CSIRO (2021), *CSIRO Solid Oxide Electrolysis: Liquid Fuels R&D Project*. available at https://arena.gov.au/assets/2021/10/csiro-solid-oxide-electrolysis-summary-report.pdf

Cuéllar-Franca, R. M. and Azapagic, A. (2015), Carbon Capture, Storage and Utilisation Technologies: A Critical Analysis and Comparison of Their Life Cycle Environmental Impacts. *Journal of CO_2 Utilization*, 9: 82–102.

Díaz, J.o, de la Osa, A., Sánchez, P., Romero, A. and Valverde, J. (2014), Influence of CO_2 Co-Feeding on Fischer–Tropsch Fuels Production over Carbon Nanofibers Supported Cobalt Catalyst. *Catalysis Communications*, 44: 57–61.

Dicke, L. (2021), Successful Test Operation of the World's Largest High-Temperature Electrolysis Module. : 1–2. available at https://www.sunfire.de/en/news/detail/successful-test-operation-of-the-worlds-largest-high-temperature-electrolysis-module [1 April 2022].

Diethelm, S., Herle, J. Van, Montinaro, D. and Bucheli, O. (2013), Electrolysis and Co-Electrolysis Performance of SOE Short Stacks. *Fuel Cells*, 13(4): 631–637.

Dimitriou, I., García-Gutiérrez, P., Elder, R. H., Cuéllar-Franca, . M., Azapagic, A. and Allen, R. (2015), Carbon Dioxide Utilisation for Production of Transport Fuels: Process

and Economic Analysis. *Energy and Environmental Science*, 8(6): 1775–1789.

Ding, F., Zhang, A., Liu, M., Zuo, Y., Li, K., Guo, X. and Song, C. (2014), CO_2 Hydrogenation to Hydrocarbons over Iron-Based Catalyst: Effects of Physicochemical Properties of Al2O3 Supports. *Industrial and Engineering Chemistry Research*, 53: 17563–17569.

Donnelly, T. J., Yates, I. C. and Satterfield, C. N. (1988), Analysis and Prediction of Product Distributions of the Fischer-Tropsch Synthesis. *Energy and Fuels*, 2(6): 734–739.

Ebbesen, S. D., Høgh, J., Nielsen, K. A., Nielsen, J. and Mogensen, M. (2011), Durable SOC Stacks for Production of Hydrogen and Synthesis Gas by High Temperature Electrolysis. *International Journal of Hydrogen Energy*, 36(13): 7363–7373.

Edwards, D. (2012), Scaling up Step by Step. *Biofuels International*: 44–46.

Ermolaev, V. S., Gryaznov, K. O., Mitberg, E. B., Mordkovich, V. Z. and Tretyakov, V. F. (2015), Laboratory and Pilot Plant Fixed-Bed Reactors for Fischer-Tropsch Synthesis: Mathematical Modeling and Experimental Investigation. *Chemical Engineering Science*, 138: 1–8.

Faes, A., Hessler-Wyser, A., Presvytes, D., Vayenas, C. G. and Vanherle, J. (2009), Nickel-Zirconia Anode Degradation and Triple Phase Boundary Quantification from Microstructural Analysis. *Fuel Cells*, 9(6): 841–851.

Farlenkov, A. S., Ananyev, M. V., Eremin, V. A., Porotnikova, N. M. and Kurumchin, E. K.H. (2015), Particle Coarsening Influence on Oxygen Reduction in LSM-YSZ Composite Materials. *Fuel Cells*, 15(1): 131–139.

Farzad, S., Rashidi, A., Haghtalab, Ali. and Mandegari, M.(2014), Study of Effective Parameters in the Fischer Tropsch Synthesis Using Monolithic CNT Supported Cobalt Catalysts. *Fuel*, 132: 27–35.

Fernández-Torres, M. J., Dednam, W. and Caballero, J. A. (2022), Economic and Environmental Assessment of Directly Converting CO_2 into a Gasoline Fuel. *Energy Conversion and Management*, 252: 115115.

Fu, Q., Mabilat, C., Zahid, M., Brisse, A. and Gautier, L. (2010), Syngas Production via High-Temperature Steam/CO_2 Co-Electrolysis: An Economic Assessment. *Energy and Environmental Science*, 3(10): 1382–1397.

Galvis, H. M. Torres, B., Johannes H., Khare, C. B., Ruitenbeek, M., Dugulan, A. and De Jong, K. P. (2012), Supported Iron Nanoparticles as Catalysts for Sustainable Production of Lower Olefins. *Science*, 335: 835–838.

Gao, P., Li, S., Bu, Xianni, D., Shanshan, L., Ziyu, W., Hui, Z., Liangshu, Q., Minghuang, Y., Chengguang, C., Jun, W., Wei and Sun, Y. (2017), Direct Conversion of CO_2 into Liquid Fuels with High Selectivity over a Bifunctional Catalyst. *Nature Chemistry*, 9(10): 1019–1024.

Global CCS Institute (2019), Global Status of CCS. *SpringerReference*. available at https://www.globalccsinstitute.com/resources/global-status-report/ [16 January 2022].

Gorimbo, J., Muleja, A., Liu, X. and Hildebrandt, D. (2018), Fischer–Tropsch Synthesis: Product Distribution, Operating Conditions, Iron Catalyst Deactivation and Catalyst Speciation. *International Journal of Industrial Chemistry*, 9(4): 317–333.

Graves, C., Ebbesen, S. D. and Mogensen, M. (2011), Co-Electrolysis of CO_2 and H_2O in Solid Oxide Cells: Performance and Durability. *Solid State Ionics*, 192(1): 398–403.

Graves, C., Ebbesen, S. D., Jensen, S. H., Simonsen, S. and Mogensen, M. (2015), Eliminating Degradation in Solid Oxide Electrochemical Cells by Reversible Operation. *Nature Materials*, 14(2): 239–244.

Grim, R. Gary, H., Zhe, G. Michael T., Ferrell, J. R., Tao, L. and Schaidle, J. A. (2020), Transforming the Carbon Economy: Challenges and Opportunities in the Convergence of Low-Cost Electricity and Reductive CO_2 Utilization. *Energy & Environmental Science*: 472–494.

GSTC (2022), Syngas Applications - Synthetic Fuels. available at https://globalsyngas.org/syngas-technology/syngas-applications/synthetic-fuels/ [28 January 2022].

Guettel, R. and Turek, T. (2009), Comparison of Different Reactor Types for Low Temperature Fischer–Tropsch Synthesis: A Simulation Study. *Chemical Engineering Science*, 64: 955–964.

Guo, ., Cui, Y., Zhang, P., Peng, X., Yoneyama, Y., Yang, G. and Tsubaki, N. (2018), Enhanced Liquid Fuel Production from CO_2 Hydrogenation: Catalytic Performance of Bimetallic Catalysts over a Two-Stage Reactor System. *ChemistrySelect*, 3(48): 13705–

13711.

Hansen, J. (2015), Solid Oxide Electrolysis - a Key Enabling Technology for Sustainable Energy Scenarios. *Faraday Discussions*, 182: 9–48.

Hattori, M., Takeda, Y., Sakaki, Y., Nakanishi, A., Ohara, S., Mukai, K., Lee, J. and Fukui, T. (2004), Effect of Aging on Conductivity of Yttria Stabilized Zirconia. *Journal of Power Sources*, 126(1–2): 23–27.

Hauch, A., Küngas, R., Blennow, P., Hansen, A. B., Hansen, J. B., Mathiesen, B. V. and Mogensen, M. B. (2020), Recent Advances in Solid Oxide Cell Technology for Electrolysis. *Science*, 370(6513): 186.

Hawkes, G, O'Brien, J, Stoots, C, Herring, S and Jones, R (2006), Three Dimensional CFD Model of a Planar Solid Oxide Electrolysis Cell for Co-Electrolysis of Steam and Carbon Dioxide, 911874, in: *Fuel Cell Seminar*. Honolulu.

Hawkins, A. S, McTernan, P., Lian, H., Kelly, R. and Adams, M. (2013), Biological Conversion of Carbon Dioxide and Hydrogen into Liquid Fuels and Industrial Chemicals. *Current Opinion in Biotechnology*, 24(3): 376–384.

He, Z., Cui, M., Qian, Q., Zhang, J., Liu, H. and Han, B. (2019), Synthesis of Liquid Fuel via Direct Hydrogenation of CO_2. *Proceedings of the National Academy of Sciences of the United States of America*, 116(26): 12654–12659.

Herz, Gregor, Reichelt, Erik and Jahn, Matthias (2018), Techno-Economic Analysis of a Co-Electrolysis-Based Synthesis Process for the Production of Hydrocarbons. *Applied Energy*, 215: 309–320.

Heuberger, Clara F., Staffell, Iain, Shah, Nilay and Mac Dowell, Niall (2016), Quantifying the Value of CCS for the Future Electricity System. *Energy and Environmental Science*, 9(8): 2497–2510.

Hillestad, M. (2015), Modeling the Fischer-Tropsch Product Distribution and Model Implementation. *Chemical Product and Process Modeling*, 10(3): 147–159.

Hooshyar, N., Vervloet, D., Kapteijn, F., Hamersma, P. J., Mudde, R. F. and van Ommen, J. R. (2012), Intensifying the Fischer-Tropsch Synthesis by Reactor Structuring – A Model Study. *Chemical Engineering Journal*, 207–208: 865–870.

135

Horáček, . (2020), Fischer–Tropsch Synthesis, the Effect of Promoters, Catalyst Support, and Reaction Conditions Selection. *Monatshefte für Chemie - Chemical Monthly*, 151(5): 649–675.

Hwang, S., Zhang, C., Han, S., Park, H., Kim, Y., Yang, ., Jun, K. and Kim, S. (2020), Mesoporous Carbon as an Effective Support for Fe Catalyst for CO_2 Hydrogenation to Liquid Hydrocarbons. *Journal of CO_2 Utilization*, 37: 65–73.

IEA (2011), Technology Roadmap: Carbon Capture and Storage in Industrial Applications. *Encyclopedia of Production and Manufacturing Management*: 781–782. available at http://www.ccsassociation.org/index.php/download_file/view/274/98 [28 December 2021].

IPCC (2018), Special Report - Global Warming of 1.5 ^{o}C. : 300. available at https://www.ipcc.ch/sr15 [5 November 2021].

Jacobs, G., Das, T. K., Li, J., Luo, Mingshe., Patterson, P. M. and Davis, B. H. (2007), Fischer-Tropsch Synthesis: Influence of Support on the Impact of Co-Fed Water for Cobalt-Based Catalysts. *Studies in Surface Science and Catalysis*, 163: 217–253.

Janssen, P. J.D., Lambreva, M. D., Plumeré, N., Bartolucci, C., Antonacci, A., Buonasera, K., Frese, R. N., Scognamiglio, V. and Rea, G. (2014), Photosynthesis at the Forefront of a Sustainable Life. *Frontiers in Chemistry*, 2: 36.

Jantarang, S., Lovell, E. C., Tan, T., Scott, J. and Amal, R. (2018), Role of Support in Photothermal Carbon Dioxide Hydrogenation Catalysed by Ni/CexTiyO$_2$. *Progress in Natural Science: Materials International*, 28: 168–177.

Jarvis, S. M. and Samsatli, Sh. (2018), Technologies and Infrastructures Underpinning Future CO_2 Value Chains: A Comprehensive Review and Comparative Analysis. *Renewable and Sustainable Energy Reviews*, 85: 46–68.

Jia, Li, Lu, Zhe, Miao, Jipeng, Liu, Zhiguo, Li, Guoqing and Su, Wenhui (2006), Effects of Pre-Calcined YSZ Powders at Different Temperatures on Ni-YSZ Anodes for SOFC. *Journal of Alloys and Compounds*, 414: 152–157.

Jiang, F., Liu, B., Geng, S., Xu, Y. and Liu, X. (2018), Hydrogenation of CO_2 into Hydrocarbons: Enhanced Catalytic Activity over Fe-Based Fischer-Tropsch Catalysts. *Catalysis Science and Technology*, 8: 4097–4107.

Jiang, N. and Wachsman, E. (1999), Structural Stability and Conductivity of Phase-Stabilized Cubic Bismuth Oxides. *Journal of the American Ceramic Society*, 82(11): 3057–3064.

Kathiraser, Y., Oemar, U., Saw, E., Li, Z. and Kawi, S. (2015), Kinetic and Mechanistic Aspects for CO_2 Reforming of Methane over Ni Based Catalysts. *Chemical Engineering Journal*, 278: 62–78.

Keane, M., Mahapatra, M. K., Verma, A. and Singh, P. (2012), LSM-YSZ Interactions and Anode Delamination in Solid Oxide Electrolysis Cells. *International Journal of Hydrogen Energy*, 37: 16776–16785.

Khan, M., Butolia, P., Jo, H., Irshad, M., Han, D., Nam, K. and Kim, J. (2020), Selective Conversion of Carbon Dioxide into Liquid Hydrocarbons and Long-Chain α-Olefins over Fe-Amorphous AlO XBifunctional Catalysts. *ACS Catalysis*, 10: 10325–10338.

Khangale, P. R., Meijboom, R. and Jalama, K. (2020), CO_2 Hydrogenation to Liquid Hydrocarbons via Modified Fischer–Tropsch over Alumina-Supported Cobalt Catalysts: Effect of Operating Temperature, Pressure and Potassium Loading. *Journal of CO_2 Utilization*, 41: 101268.

Khesa, N. and Mulopo, J. (2021), Performance Evaluation, Optimization and Exergy Analysis of a High Temperature Co-Electrolysis Power to Gas Process Using Aspen Plus®-a Model Based Study. *Energy Science and Engineering*, 9(11): 1950–1960.

Khozema, Ali Ahmed, Mardiana, Idayu Ahmad and Yusri, Yusup (2020), Issues, Impacts, and Mitigations of Carbon Dioxide Emissions in the Building Sector. *Sustainability*, 12: 7427.

Kim-Lohsoontorn, P. and Bae, J. (2011), Electrochemical Performance of Solid Oxide Electrolysis Cell Electrodes under High-Temperature Coelectrolysis of Steam and Carbon Dioxide. *Journal of Power Sources*, 196: 7161–7168.

de Klerk, A. (2011), *Fischer-Tropsch Refining*. Weinheim: Wiley-VCH.

Kondoh, J., Kawashima, T., Kikuchi, S., Tomii, Y. and Ito, Y. (1995), Effect of Aging on Yltria-Stabilized Zirconia. *Journal of The Electrochemical Society*, 145(5): 1527–1536.

Kotisaari, M., Thomann, O., Montinaro, D. and Kiviaho, J. (2017), Evaluation of a SOE Stack for Hydrogen and Syngas Production: A Performance and Durability Analysis. *Fuel Cells*, 17(4): 571–580.

Kulkarni, A. P., Hos, T., Landau, M. V., Fini, D., Giddey, S. and Herskowitz, M. (2021), Techno-Economic Analysis of a Sustainable Process for Converting CO2and H2O to Feedstock for Fuels and Chemicals. *Sustainable Energy and Fuels*, 5: 486–500.

Landau, M. V., Vidruk, R. and Herskowitz, M. (2014), Sustainable Production of Green Feed from Carbon Dioxide and Hydrogen. *ChemSusChem*, 7(3): 785–794.

Lang, M., Bohn, C., Couturier, K., Sun, X., McPhail, S. J., Malkow, T., Pilenga, A., Fu, Q. and Liu, Q. (2019), Electrochemical Quality Assurance of Solid Oxide Electrolyser (SOEC) Stacks. *Journal of The Electrochemical Society*, 166: F1180–F1189.

Larrain, D., Van herle, J. and Favrat, D. (2006), Simulation of SOFC Stack and Repeat Elements Including Interconnect Degradation and Anode Reoxidation Risk. *Journal of Power Sources*, 161(1): 392–403.

Lei, Linfeng, Bai, Lu, Lindbråthen, Arne, Pan, Fengjiao, Zhang, Xiangping and He, Xuezhong (2020), Carbon Membranes for CO_2 Removal: Status and Perspectives from Materials to Processes. *Chemical Engineering Journal*, 401: 126084.

Leung, D. Y.C., Caramanna, G. and Maroto-Valer, M. M. (2014), An Overview of Current Status of Carbon Dioxide Capture and Storage Technologies. *Renewable and Sustainable Energy Reviews*, 39: 426–443.

Li, B., Fan, X., Zhou, K. and Wang, T. J. (2017), Effect of Oxide Growth on the Stress Development in Double-Ceramic-Layer Thermal Barrier Coatings. *Ceramics International*, 43(17): 14763–14774.

Li, Qingshan, Zheng, Yifeng, Sun, Yuanna, Li, Tingshuai, Xu, Cheng, Wang, Weiguo and Chan, Siew Hwa (2019), Understanding the Occurrence of the Individual CO_2 Electrolysis during H_2O-CO_2 Co-Electrolysis in Classic Planar Ni-YSZ/YSZ/LSM-YSZ Solid Oxide Cells. *Electrochimica Acta*, 318: 440–448.

Li, W., Wang, H., Jiang, X., Zhu, J., Liu, Z., Guo, X. and Song, C. (2018), A Short Review of Recent Advances in CO_2 Hydrogenation to Hydrocarbons over Heterogeneous Catalysts. *RSC Advances*, 8(14): 7651–7669.

Li, W., Wang, H., Shi, Y. and Cai, N. (2013), Performance and Methane Production Characteristics of H2O–CO2 Co-Electrolysis in Solid Oxide Electrolysis Cells. *International Journal of Hydrogen Energy*, 38(25): 11104–11109.

Li, X., Chen, Y., Liu, S., Zhao, N., Jiang, X., Su, M. and Li, Z. (2021), Enhanced Gasoline Selectivity through Fischer-Tropsch Synthesis on a Bifunctional Catalyst: Effects of Active Sites Proximity and Reaction Temperature. *Chemical Engineering Journal*, 416: 129180.

Li, Y., Wang, T., Wu, C., Li, H., Qin, X. and Tsubaki, N. (2010), Gasoline-Range Hydrocarbon Synthesis over $Co/SiO_2/HZSM-5$ Catalyst with CO_2-Containing Syngas. *Fuel Processing Technology*, 91: 388–393.

Liu, W., Hu, J. and Wang, Y. (2009), Fischer-Tropsch Synthesis on Ceramic Monolith-Structured Catalysts. *Catalysis Today*, 140: 142–148.

Liu, Y. L., Thydén, K., Chen, M. and Hagen, A. (2012), Microstructure Degradation of LSM-YSZ Cathode in SOFCs Operated at Various Conditions. *Solid State Ionics*, 206: 97–103.

Liu, Yanyong, Hanaoka, Toshiaki, Miyazawa, Tomohisa, Murata, Kazuhisa, Okabe, Kiyomi and Sakanishi, Kinya (2009), Fischer–Tropsch Synthesis in Slurry-Phase Reactors over Mn- and Zr-Modified Co/SiO_2 Catalysts. *Fuel Processing Technology*, 90(7–8): 901–908.

Liu, Yi, Chen, Jian Feng, Bao, Jun and Zhang, Yi (2015), Manganese-Modified Fe_3O_4 Microsphere Catalyst with Effective Active Phase of Forming Light Olefins from Syngas. *ACS Catalysis*, 5(6): 3905–3909.

Lovley, D. and Nevin, K. (2013), Electrobiocommodities: Powering Microbial Production of Fuels and Commodity Chemicals from Carbon Dioxide with Electricity. *Current Opinion in Biotechnology*, 24(3): 385–390.

Luo, Y., Shi, Y., Li, W. and Cai, N. (2014), Comprehensive Modeling of Tubular Solid Oxide Electrolysis Cell for Co-Electrolysis of Steam and Carbon Dioxide. *Energy*, 70: 420–434.

Luo, Y., Shi, Y., Li, W. and Cai, N. (2015), Dynamic Electro-Thermal Modeling of Co-Electrolysis of Steam and Carbon Dioxide in a Tubular Solid Oxide Electrolysis Cell. *Energy*, 89: 637–647.

Ma, W., Jacobs, G., Sparks, D. E, Gnanamani, M., Ramana, V., Pendyala, R., Yen, C., Klettlinger, J., Tomsik, T. and Davis, B. (2011), Fischer – Tropsch Synthesis : Support

and Cobalt Cluster Size Effects on Kinetics over Co/Al2O3 and Co/SiO2 Catalysts. *Fuel*, 90: 756–765.

Ma, W., Jacobs, G., Sparks, D. E, Spicer, R. L, Davis, B., Klettlinger, J. and Yen, C. (2014), Fischer–Tropsch Synthesis: Kinetics and Water Effect Study over 25%Co/Al2O3 Catalysts. *Catalysis Today*, 228: 158–166.

Malik, K., Singh, S., Basu, S. and Verma, A. (2017), Electrochemical Reduction of CO_2 for Synthesis of Green Fuel. *Wiley Interdisciplinary Reviews: Energy and Environment*, 6: e244.

Mandal, S., Maity, S., Gupta, Pavan K., Mahato, Abhishek, Bhanja, Piyali and Sahu, Gajanan (2018), Synthesis of Middle Distillate through Low Temperature Fischer-Tropsch (LTFT) Reaction over Mesoporous SDA Supported Cobalt Catalysts Using Syngas Equivalent to Coal Gasification. *Applied Catalysis A: General*, 557: 55–63.

Marchese, M., Giglio, E., Santarelli, M. and Lanzini, A. (2020), Energy Performance of Power-to-Liquid Applications Integrating Biogas Upgrading, Reverse Water Gas Shift, Solid Oxide Electrolysis and Fischer-Tropsch Technologies. *Energy Conversion and Management: X*, 6: 100041.

Martinelli, M., Gnanamani, M., LeViness, S., Jacobs, G. and Shafer, W. D. (2020), An Overview of Fischer-Tropsch Synthesis: XtL Processes, Catalysts and Reactors. *Applied Catalysis A: General*, 608: 117740.

Meiri, N., Dinburg, Y., Amoyal, M., Koukouliev, V., Nehemya, R., Landau, Miron V. and Herskowitz, M. (2015), Novel Process and Catalytic Materials for Converting CO_2 and H_2 Containing Mixtures to Liquid Fuels and Chemicals. *Faraday Discussions*, 183: 197–215.

Meiri, N., Radus, R. and Herskowitz, M. (2017), Simulation of Novel Process of CO_2 Conversion to Liquid Fuels. *Journal of CO_2 Utilization*, 17: 284–289.

Menon, V., Fu, Q., Janardhanan, V.. and Deutschmann, O. (2015), A Model-Based Understanding of Solid-Oxide Electrolysis Cells (SOECs) for Syngas Production by H_2O/CO_2 Co-Electrolysis. *Journal of Power Sources*, 274: 768–781.

Mierczynski, P., Dawid, B., Maniukiewicz, W., Mosinska, Ma., Zakrzewski, M., Ciesielski, R., Kedziora, A., Dubkov, S., Gromov, D., Rogowski, J., Witonska, I., Szynkowska, M.

I. and Maniecki, T. (2018), Fischer–Tropsch Synthesis over Various Fe/Al$_2$O$_3$–Cr$_2$O$_3$ Catalysts. *Reaction Kinetics, Mechanisms and Catalysis*, 124: 545–561.

Mikayilov, J., Mukhtarov, S. and Mammadov, J. (2020), Gasoline Demand Elasticities at the Backdrop of Lower Oil Prices: Fuel-Subsidizing Country Case. *Energies*, 13: 6752.

Mikkelsen, M., Jørgensen, M. and Krebs, F. C. (2010), The Teraton Challenge. A Review of Fixation and Transformation of Carbon Dioxide. *Energy and Environmental Science*, 3(1): 43–81.

Mirzaei, A. A., Vahid, S. and Feyzi, M. (2009), Fischer-Tropsch Synthesis over Iron Manganese Catalysts: Effect of Preparation and Operating Conditions on Catalyst Performance. *Advances in Physical Chemistry*, 2009: 1–12.

Mitterdorfer, A. and Gauckler, L. J. (1998), La$_2$Zr$_2$O$_7$ Formation and Oxygen Reduction Kinetics of the La$_{0.85}$Sr$_{0.15}$MnyO$_3$, O2(g)|YSZ System. *Solid State Ionics*, 111: 185–218.

Moazami, N., Wyszynski, Miroslaw L., Mahmoudi, H., Tsolakis, A., Zou, Z., Panahifar, P. and Rahbar, K. (2015), Modelling of a Fixed Bed Reactor for Fischer–Tropsch Synthesis of Simulated N2-Rich Syngas over Co/SiO2: Hydrocarbon Production. *Fuel*, 154: 140–151.

Moçoteguy, P. and Brisse, A. (2013), A Review and Comprehensive Analysis of Degradation Mechanisms of Solid Oxide Electrolysis Cells. *International Journal of Hydrogen Energy*, 38(36): 15887–15902.

Myrstad, Rune, Eri, Sigrid, Pfeifer, Peter, Rytter, Erling and Holmen, Anders (2009), Fischer-Tropsch Synthesis in a Microstructured Reactor. *Catalysis Today*, 147S: S301–S304.

Naims, H. (2016), Economics of Carbon Dioxide Capture and Utilization—a Supply and Demand Perspective. *Environmental Science and Pollution Research*, 23(22): 22226–22241.

Najari, S., Gróf, G. and Saeidi, S. (2019), Enhancement of Hydrogenation of CO2 to Hydrocarbons via In-Situ Water Removal. *International Journal of Hydrogen Energy*, 44: 24759–24781.

Navasa, M., Graves, C., Chatzichristodoulou, C., Løye S., Theis, S., Bengt and Lund F. (2018), A Three Dimensional Multiphysics Model of a Solid Oxide Electrochemical

Cell: A Tool for Understanding Degradation. *International Journal of Hydrogen Energy*, 43(27): 11913–11931.

Nerat, M. and Juričić, Đ. (2018), Modelling of Anode Delamination in Solid Oxide Electrolysis Cell and Analysis of Its Effects on Electrochemical Performance. *International Journal of Hydrogen Energy*, 43: 8179–8189.

Ni, M. (2012a), An Electrochemical Model for Syngas Production by Co-Electrolysis of H_2O and CO_2. *Journal of Power Sources*, 202: 209–216.

Ni, M. (2012b), 2D Thermal Modeling of a Solid Oxide Electrolyzer Cell (SOEC) for Syngas Production by H_2O/CO_2 Co-Electrolysis. *International Journal of Hydrogen Energy*, 37(8): 6389–6399.

Norhasyima, R.S. and Mahlia, T.M.I. (2018), Advances in CO_2 Utilization Technology: A Patent Landscape Review. *Journal of CO_2 Utilization*, 26: 323–335.

O'Brien, J.E., McKellar, M.G., Stoots, C.M., Herring, J.S. and Hawkes, G.L. (2009), Parametric Study of Large-Scale Production of Syngas via High-Temperature Co-Electrolysis. *International Journal of Hydrogen Energy*, 34(9): 4216–4226.

Olajire, A. A. (2013), A Review of Mineral Carbonation Technology in Sequestration of CO_2. *Journal of Petroleum Science and Engineering*, 109: 364–392.

OPEC (2017), *World Oil Outlook 2040*. Vienna. available at https://www.opec.org/opec_web/flipbook/WOO2017/WOO2017/assets/common/downloads/WOO 2017.pdf

Overland, I. (2016), Energy: The Missing Link in Globalization. *Energy Research & Social Science*, 14: 122–130.

Owen, R. E., O'Byrne, Justin P., Mattia, D., Plucinski, P., Pascu, S. I. and Jones, M. D. (2013), Cobalt Catalysts for the Conversion of CO_2 to Light Hydrocarbons at Atmospheric Pressure. *Chemical Communications*, 49: 11683–11685.

Palcut, M., Mikkelsen, L., Neufeld, K., Ch., Ming, K., Ruth and Hendriksen, P. (2012), Improved Oxidation Resistance of Ferritic Steels with LSM Coating for High Temperature Electrochemical Applications. *International Journal of Hydrogen Energy*, 37: 8087–8094.

Pendyala, V., Jacobs, G., Mohandas, J. C., Luo, M., Hamdeh, H. H., Ji, Y., Ribeiro, M.C. and Davis, B. H. (2010), Fischer-Tropsch Synthesis: Effect of Water over Iron-Based Catalysts. *Catalysis Letters*, 140: 98–105.

Piermartini, P., Boeltken, T., Selinsek, M. and Pfeifer, P. (2017), Influence of Channel Geometry on Fischer-Tropsch Synthesis in Microstructured Reactors. *Chemical Engineering Journal*, 313: 328–335.

Placido, A., Challman, D., Liu, K., Andrews, R., Jacobs, Gary, Davis, B., Ma, Wenping and Darkwah, K. (2018), *Small-Scale Pilot Plant for Gasification of Coal and Coal/Biomass Blends and Conversion of Derived Syngas to Liquid Fuels via Fischer-Tropsch Synthesis*. Kentucky.

Porosoff, M. D., Yan, B. and Chen, J. G. (2016), Catalytic Reduction of CO_2 by H_2 for Synthesis of CO, Methanol and Hydrocarbons: Challenges and Opportunities. *Energy and Environmental Science*, 9(1): 62–73.

Qian, W., Ma, H., Li, T., Ying, W. and Fang, D. (2012), Modeling of a Slurry Bubble Column Reactor for Fischer-Tropsch Synthesis. *Journal of Coal Science and Engineering*, 18(1): 88–95.

Reuel, R. C. and Bartholomew, C. H. (1984), Effects of Support and Dispersion on the CO Hydrogenation Activity/Selectivity Properties of Cobalt. *Journal of Catalysis*, 85(1): 78–88.

Reytier, M., Di Iorio, S., Chatroux, A., Petitjean, M., Cren, J., De Saint Jean, M., Aicart, J. and Mougin, J. (2015), Stack Performances in High Temperature Steam Electrolysis and Co-Electrolysis. *International Journal of Hydrogen Energy*, 40: 11370–11377.

Riedel, M., Heddrich, M. P. and Friedrich, K. A. (2020), Experimental Analysis of the Co-Electrolysis Operation under Pressurized Conditions with a 10 Layer SOC Stack. *Journal of The Electrochemical Society*, 167: 024504.

Riedel, T., Claeys, M., Schulz, H., Schaub, G., Nam, S., Jun, K., Choi, M., Kishan, Gurram and Lee, K. (1999), Comparative Study of Fischer–Tropsch Synthesis with H_2/CO and H_2/CO_2 Syngas Using Fe- and Co-Based Catalysts. *Applied Catalysis A: General*, 186: 201–213.

Rodrigues, C. Dinis, M. and Lemos de Sousa, M. (2015), Review of European Energy

Policies Regarding the Recent "Carbon Capture, Utilization and Storage" Technologies Scenario and the Role of Coal Seams. *Environmental Earth Sciences*, 74(3): 2553–2561.

Rosa, R. (2017), The Role of Synthetic Fuels for a Carbon Neutral Economy. *C- Journal of Carbon Research*, 3(2): 11.

Saeidi, S., Amiri, M., Amin, N. and Rahimpour, M. (2014), Progress in.Reactors for High-Temperature Fischer-Tropsch Process: Determination Place of Intensifier Reactor Perspective. *International Journal of Chemical Reactor Engineering*, 12(1): 639–664.

Saeidi, S., Najari, S., Hessel, V., Wilson, K., Keil, F. J., Concepción, P., Suib, S. L. and Rodrigues, A. E. (2021), Recent Advances in CO_2 Hydrogenation to Value-Added Products — Current Challenges and Future Directions. *Progress in Energy and Combustion Science*, 85: 100905.

Saeidi, S., Nikoo, M., Mirvakili, A., Bahrani, S., Saidina A., Nor A. and Rahimpour, M. (2015), Recent Advances in Reactors for Low-Temperature Fischer-Tropsch Synthesis: Process Intensification Perspective. *Reviews in Chemical Engineering*, 31(3): 209–238.

Samavati, M., Martin, A., Nemanova, V. and Santarelli, M. (2018), Integration of Solid Oxide Electrolyser, Entrained Gasification, and Fischer-Tropsch Process for Synthetic Diesel Production: Thermodynamic Analysis. *International Journal of Hydrogen Energy*, 43: 4785–4803.

Scalbert, J., Clémençon, I., Lecour, P, B, Laure, D., Fabrice and Legens, Christèle (2015), Simultaneous Investigation of the Structure and Surface of a Co/Alumina Catalyst during Fischer-Tropsch Synthesis: Discrimination of Various Phenomena with Beneficial or Disadvantageous Impact on Activity. *Catalysis Science and Technology*, 5: 4193–4201.

Sehested, J., Gelten, J. A.P. and Helveg, S. (2006), Sintering of Nickel Catalysts: Effects of Time, Atmosphere, Temperature, Nickel-Carrier Interactions, and Dopants. *Applied Catalysis A: General*, 309(2): 237–246.

Sehested, J., Gelten, J. A.P., Remediakis, I.N., Bengaard, H. and Nørskov, J. K. (2004), Sintering of Nickel Steam-Reforming Catalysts: Effects of Temperature and Steam and Hydrogen Pressures. *Journal of Catalysis*, 223: 432–443.

Selvatico, D., Lanzini, A. and Santarelli, M. (2016), Low Temperature Fischer-Tropsch Fuels

from Syngas: Kinetic Modeling and Process Simulation of Different Plant Configurations. *Fuel*, 186: 544–560.

Seyednejadian, S., Rauch, R., Bensaid, S., Hofbauer, H., Weber, G. and Saracco, G. (2018), Power to Fuels: Dynamic Modeling of a Slurry Bubble Column Reactor in Lab-Scale for Fischer Tropsch Synthesis under Variable Load of Synthesis Gas. *Applied Sciences*, 8(4): 514.

Shi, Z., Yang, H., Gao, P., Chen, X., Liu, H., Zhong, L., Wang, H., Wei, W. and Sun, Y. (2018), Effect of Alkali Metals on the Performance of CoCu/TiO_2 Catalysts for CO_2 Hydrogenation to Long-Chain Hydrocarbons. *Chinese Journal of Catalysis*, 39: 1294–1302.

Shimura, Katsuya, Miyazawa, Tomohisa, Hanaoka, Toshiaki and Hirata, Satoshi (2015), Fischer-Tropsch Synthesis over Alumina Supported Cobalt Catalyst: Effect of Promoter Addition. *Applied Catalysis A: General*, 494: 1–11.

Slade, R. and Bauen, A. (2013), Micro-Algae Cultivation for Biofuels: Cost, Energy Balance, Environmental Impacts and Future Prospects. *Biomass and Bioenergy*, 53: 29–38.

Snoeckx, R. and Bogaerts, A. (2017), Plasma Technology-a Novel Solution for CO_2 Conversion? *Chemical Society Reviews*, 46(19): 5805–5863.

Sohal, M. S., O'Brien, J. E., Stoots, C. M., Sharma, V. I., Yildiz, B. and Virkar, A. (2012), Degradation Issues in Solid Oxide Cells during High Temperature Electrolysis. *Journal of Fuel Cell Science and Technology*, 9(1): 1–10.

Sönnichsen, N. (2022), Demand Outlook for Selected Oil Products Worldwide from 2020 to 2045. available at https://www.statista.com/statistics/282774/global-product-demand-outlook-worldwide [27 February 2022].

Stempien, J., Liu, Q., Ni, M., Sun, Q. and Chan, S. (2014), Physical Principles for the Calculation of Equilibrium Potential for Co-Electrolysis of Steam and Carbon Dioxide in a Solid Oxide Electrolyzer Cell (SOEC). *Electrochimica Acta*, 147: 490–497.

Stempien, J., Ni, M., Sun, Q. and Chan, S. (2015), Thermodynamic Analysis of Combined Solid Oxide Electrolyzer and Fischer–Tropsch Processes. *Energy*, 81: 682–690.

Stempien, J., Sun, Q. and Chan, S. (2013a), Solid Oxide Electrolyzer Cell Modeling: A Review. *Journal of Power of Technologies*, 93(4): 216–246.

Stempien, J., Sun, Q. and Chan, S. (2013b), Performance of Power Generation Extension System Based on Solid-Oxide Electrolyzer Cells under Various Design Conditions. *Energy*, 55: 647–657.

Stoots, C., O'Brien, J., Condie, K. and Hartvigsen, J. (2010), High-Temperature Electrolysis for Large-Scale Hydrogen Production from Nuclear Energy – Experimental Investigations. *International Journal of Hydrogen Energy*, 35: 4861–4870.

Stoots, C., O'Brien, J., Herring, J. and Hartvigsen, J. J. (2009), Syngas Production via High-Temperature Coelectrolysis of Steam and Carbon Dioxide. *Journal of Fuel Cell Science and Technology*, 6(1): 0110141–01101412.

Stratas Advisors (2021), *Phase-out of RON 80 Gasoline Progresses in the CIS*. available at https://stratasadvisors.com/Insights/2021/09302021-Global-Octane-Market-Share

Styring, P. and Armstrong, K. (2011), Catalytic Carbon Dioxide Conversions to Value-Added Chemicals. *Chimica oggi*, 29(6): 34–37.

Sun, Xiufu, Chen, Ming, Liu, Yi-Lin, Hjalmarsson, Per, Ebbesen, Sune Dalgaard, Jensen, Søren Højgaard, Mogensen, Mogens Bjerg and Hendriksen, Peter Vang (2013), Durability of Solid Oxide Electrolysis Cells for Syngas Production. *Journal of The Electrochemical Society*, 160(9): F1074–F1080.

Tao, Zhichao, Yang, Yong, Zhang, Chenghua, Li, Tingzhen, Wang, Jianhua, Wan, Haijun, Xiang, Hongwei and Li, Yongwang (2006), Effect of Calcium Promoter on a Precipitated Iron-Manganese Catalyst for Fischer-Tropsch Synthesis. *Catalysis Communications*, 7: 1061–1066.

Tarasov, A. L., Isaeva, V. I., Tkachenko, O. P., Chernyshev, V. V. and Kustov, L. M. (2018), Conversion of CO_2 into Liquid Hydrocarbons in the Presence of a Co-Containing Catalyst Based on the Microporous Metal-Organic Framework MIL-53(Al). *Fuel Processing Technology*, 176: 101–106.

Teimouri, Z., Abatzoglou, N. and Dalai, A. K. (2021), *Kinetics and Selectivity Study of Fischer-Tropsch Synthesis to C5+ Hydrocarbons: A Review*.

The Royal Society (2017), *The Potential and Limitations of Using Carbon Dioxide: Policy Briefing*. available at royalsociety.org/low-carbon-energy-programme [25 September 2021].

Todic, B., Bhatelia, T., Froment, G., Ma, W., Jacobs, G., Davis, B. H. and Bukur, D. B. (2013), Kinetic Model of Fischer-Tropsch Synthesis in a Slurry Reactor on Co-Re/Al$_2$O$_3$ Catalyst. *Industrial and Engineering Chemistry Research*, 52: 669–679.

Todic, B., Nowicki, L., Nikacevic, N. and Bukur, D. (2016), Fischer-Tropsch Synthesis Product Selectivity over an Industrial Iron-Based Catalyst: Effect of Process Conditions. *Catalysis Today*, 261: 28–39.

Todić, B., Ordomsky, V., Nikačević, N., Khodakov, A. and Bukur, D. (2015), Opportunities for Intensification of Fischer-Tropsch Synthesis through Reduced Formation of Methane over Cobalt Catalysts in Microreactors. *Catalysis Science and Technology*, 5(3): 1400–1411.

Tu, X., Gallon, H.J. and Whitehead, J.C. (2013), Plasma-Assisted Reduction of a NiO/Al$_2$O$_3$ Catalyst in Atmospheric Pressure H$_2$/Ar Dielectric Barrier Discharge. *Catalysis Today*, 211: 120–125.

Varrone, C., Skiadas, I. V. and Gavala, H. N. (2018), Effect of Hydraulic Retention Time on the Modelling and Optimization of Joint 1,3 PDO and BuA Production from 2G Glycerol in a Chemostat Process. *Chemical Engineering Journal*, 347: 525–534.

de Vasconcelos, B. and Lavoie, J. (2019), Recent Advances in Power-to-X Technology for the Production of Fuels and Chemicals. *Frontiers in Chemistry*, 7: 392.

Vázquez, F., Koponen, J., Ruuskanen, V., Bajamundi, C., Kosonen, A., Simell, P., Ahola, J., Frilund, C., Elfving, J., Reinikainen, M., Heikkinen, N., Kauppinen, J. and Piermartini, P. (2018), Power-to-X Technology Using Renewable Electricity and Carbon Dioxide from Ambient Air: SOLETAIR Proof-of-Concept and Improved Process Concept. *Journal of CO$_2$ Utilization*, 28: 235–246.

Virkar, A. V. (2010), Mechanism of Oxygen Electrode Delamination in Solid Oxide Electrolyzer Cells. *International Journal of Hydrogen Energy*, 35(18): 9527–9543.

Wang, C., Chen, M., Liu, M. and Yan, J. (2020), Dynamic Modeling and Parameter Analysis Study on Reversible Solid Oxide Cells during Mode Switching Transient Processes. *Applied Energy*, 263: 114601.

Wang, L., Yi, Y., Guo, H. and Tu, X. (2018), Atmospheric Pressure and Room Temperature Synthesis of Methanol through Plasma-Catalytic Hydrogenation of CO$_2$. *ACS Catalysis*,

8(1): 90–100.

Wang, L., Chen, M., Küngas, R., Lin, T., Diethelm, S., Maréchal, F. and Van herle, J. (2019), Power-to-Fuels via Solid-Oxide Electrolyzer: Operating Window and Techno-Economics. *Renewable and Sustainable Energy Reviews*, 110: 174–187.

Wang, M., Lawal, A., Stephenson, P., Sidders, J. and Ramshaw, C. (2011), Post-Combustion CO_2 Capture with Chemical Absorption: A State-of-the-Art Review. *Chemical Engineering Research and Design*, 89: 1609–1624.

Wang, X., Wang, H. and Sun, Y. (2017), Synthesis of Acrylic Acid Derivatives from CO_2 and Ethylene. *Chem*, 3: 211–228.

Wang, Y., Kazumi, S., Gao, W., Gao, X., Li, H., Guo, X., Yoneyama, Y., Yang, G. and Tsubaki, N. (2020), Direct Conversion of CO_2 to Aromatics with High Yield via a Modified Fischer-Tropsch Synthesis Pathway. *Applied Catalysis B: Environmental*, 269: 118792.

Wei, J., Ge, Qingjie, Y., Ruwei, W., Zhiyong, F., Chuanyan, G., Lisheng, X., Hengyong and Sun, J. (2017), Directly Converting CO_2 into a Gasoline Fuel. *Nature Communications*, 8: 15174.

Wei, Jian, Yao, Ruwei, Ge, Qingjie, Wen, Zhiyong, Ji, Xuewei, Fang, Chuanyan, Zhang, Jixin, Xu, Hengyong and Sun, Jian (2018), Catalytic Hydrogenation of CO_2 to Isoparaffins over Fe-Based Multifunctional Catalysts. *ACS Catalysis*, 8: 9958–9967.

Williams, P. J., Le B. and Laurens, L. L. (2010), Microalgae as Biodiesel & Biomass Feedstocks: Review & Analysis of the Biochemistry, Energetics & Economics. *Energy and Environmental Science*, 3(5): 554–590.

Wu, J., Huang, Y., Ye, W. and Li, Ya. (2017), CO_2 Reduction: From the Electrochemical to Photochemical Approach. *Advanced Science*, 4(11): 1–29.

Wu, J. and McLachlan, D. S. (1997), Percolation Exponents and Thresholds in Two Nearly Ideal Anisotropic Continuum Systems. *Physical Review B*, 56(3): 1236–1248.

Xu, Y., Liu, Da. and Liu, X. (2018), Conversion of Syngas toward Aromatics over Hybrid Fe-Based Fischer-Tropsch Catalysts and HZSM-5 Zeolites. *Applied Catalysis A: General*, 552: 168–183.

Yang, C., Li, J., Newkirk, J., Baish, V., Hu, R., Chen, Y. and Chen, F. (2015), Co-Electrolysis of H_2O and CO_2 in a Solid Oxide Electrolysis Cell with Hierarchically Structured Porous Electrodes. *Journal of Materials Chemistry A*, 3(31): 15913–15919.

Yang, C., Wei, W. and Roosen, A. (2004), Reaction Kinetics and Mechanisms between $La_{0.65}Sr_{0.3}MnO_3$ and 8 Mol% Yttria-Stabilized Zirconia. *Journal of American Ceramic Society*, 7(6): 1110–1116.

Yang, J., Sun, Y., Tang, Y., Liu, Y., Wang, H., Tian, L. et al. (2006), Effect of Magnesium Promoter on Iron-Based Catalyst for Fischer-Tropsch Synthesis. *Journal of Molecular Catalysis A: Chemical*, 245: 26–36.

Yao, B., Xiao, T., Makgae, O., Jie, X., Gonzalez-Cortes, S., Guan, S., Kirkland et al. (2020), Transforming Carbon Dioxide into Jet Fuel Using an Organic Combustion-Synthesized Fe-Mn-K Catalyst. *Nature Communications*, 11: 6395.

Ye, R., Ding, J., Gong, W., Argyle, M., Zhong, Q., Wang, Y. et al. (2019), CO_2 Hydrogenation to High-Value Products via Heterogeneous Catalysis. *Nature Communications*, 10: 5698.

Zhang, Q., Kang, J. and Wang, Y. (2010), Development of Novel Catalysts for Fischer-Tropsch Synthesis: Tuning the Product Selectivity. *ChemCatChem*, 2: 1030–1058.

Zhang, Y., Jacobs, G., Sparks, D., Dry, M. E. and Davis, B. H. (2002), CO and CO_2 Hydrogenation Study on Supported Cobalt Fischer–Tropsch Synthesis Catalysts. *Catalysis Today*, 71(3–4): 411–418.

Zheng, Y., Luo, Y., Shi, Y. and Cai, N. (2017), Dynamic Processes of Mode Switching in Reversible Solid Oxide Fuel Cells. *Journal of Energy Engineering*, 143(6): 1–8.

Zheng, Y., Wang, J., Yu, B., Zhang, W., Chen, J., Qiao, J. and Zhang, J. (2017), A Review of High Temperature Co-Electrolysis of H_2O and CO_2 to Produce Sustainable Fuels Using Solid Oxide Electrolysis Cells (SOECs): Advanced Materials and Technology. *Chemical Society Reviews*, 46(5): 1427–1463.

Zhu, J. and Lin, Z. (2018), Degradations of the Electrochemical Performance of Solid Oxide Fuel Cell Induced by Material Microstructure Evolutions. *Applied Energy*, 231(April): 22–28.

Appendices

Appendix A.1: Repartition of mass fractions among hydrocarbon types. Data collected from Wei et al. (2017).

Carbon No	Distribution	Hydrocarbon distribution (%)				
		n-Paraffins	i-Paraffins	Olefins	Naphthenes	Aromatics
1	7.83	100.00	0.00	0.00	0.00	0.00
2	1.71	54.39	0.00	45.61	0.00	0.00
3	5.16	89.73	0.00	10.27	0.00	0.00
4	11.28	30.59	56.47	12.94	0.00	0.00
5	8.79	21.05	69.28	8.87	0.80	0.00
6	6.09	11.66	69.46	3.61	8.70	6.57
7	8.15	3.44	29.33	3.07	20.49	43.68
8	16.70	0.24	15.75	1.44	12.10	70.48
9	19.47	0.36	12.94	2.00	5.65	79.04
10	10.25	0.39	18.73	2.34	3.41	75.12
11	3.12	0.00	28.53	0.00	0.00	71.47
12	0.53	5.66	0.00	0.00	0.00	94.34
13	0.07	0.00	0.00	0.00	0.00	100.00

Appendix A.2: Initial ASF calculations.

Carbon number (i)	Mass fraction (Wi)	Selectivity	n-Paraffin	Olefin	i-Paraffin	Naphthene	Aromatic
1	0.0900	0.0783	7.83E-02				
2	0.0180	0.0171	9.30E-03	7.80E-03			
3	0.0542	0.0516	4.63E-02	5.30E-03			
4	0.1235	0.1128	3.45E-02	1.46E-02	6.37E-02		
5	0.1080	0.0879	1.85E-02	7.65E-03	6.09E-02	7.03E-04	
6	0.0908	0.0609	7.10E-03	2.20E-03	4.23E-02	5.30E-03	4.00E-03
7	0.0741	0.0815	2.80E-03	2.50E-03	2.39E-02	1.67E-02	3.56E-02
8	0.1633	0.1670	4.01E-04	2.40E-04	2.63E-02	2.02E-02	1.18E-01
9	0.1824	0.1947	7.01E-04	3.89E-03	2.52E-02	1.10E-02	1.54E-01
10	0.1012	0.1025	4.00E-04	2.40E-03	1.92E-02	3.50E-03	7.70E-02
11	0.0280	0.0312			8.90E-03		2.23E-02
12	0.0626	0.0093	5.26E-04				8.77E-03
13	0.0100						
14	0.0080						
15	0.0063						
16	0.0050						
17	0.0040						
18	0.0032						
19	0.0026						
20	0.0021						
21	0.0017						
22	0.0013						
23	0.0011						
24	0.0009						
25	0.0007						
26	0.0006						
27	0.0005						
28	0.0004						
29	0.0003						
30	0.0002						
31	0.0002						

32	0.0002						
33	0.0001						
34	0.0001						
35	0.0001						
36	0.0001						
37	0.0001						
38	0.0000						
39	0.0000						
40	0.0000						
41	0.0000						
42	0.0000						
43	0.0000						
44	0.0000						
45	0.0000						
46	0.0000						
47	0.0000						
48	0.0000						
49	0.0000						
50	0.0000						

Appendix A.3: Lumping of components

Component	Selectivity (C-mol)	Lumped selectivity
CH4	4.00E-02	CH4
C2H6	9.30E-03	C3H8
C2H4	7.80E-03	9.01E-02
C3H8	4.63E-02	C3H6
C3H6	5.30E-03	2.77E-02
n-C4H10	3.45E-02	i-C4H10
i-C4H10	6.37E-02	6.37E-02
C4H8 (olef)	1.46E-02	
n-C5H12	1.85E-02	n-C8H18
i-C5H12	6.09E-02	2.99E-02
C5H10 (olef)	7.65E-03	i-C8H18
C5H10 (naph)	7.03E-04	2.07E-01
n-C6H14	7.10E-03	C8H16 (olef)
i-C6H14	4.23E-02	1.89E-02
C6H12 (olef)	2.20E-03	C8H16 (naph)
C6H12 (naph)	5.30E-03	5.74E-02
C6H6	4.00E-03	C8H10
n-C7H16	2.80E-03	4.10E-01
i-C7H16	2.39E-02	
C7H14 (olef)	2.50E-03	C12+
C7H14 (naph)	1.67E-02	9.30E-03
C7H8	3.56E-02	
n-C8H18	4.01E-04	
i-C8H18	2.63E-02	
C8H16 (olef)	2.40E-04	
C8H16 (naph)	2.02E-02	
C8H10	1.18E-01	
n-C9H20	7.01E-04	
i-C9H20	2.52E-02	
C9H18 (olef)	3.89E-03	
C9H18 (naph)	1.10E-02	

C9H12	1.54E-01	154
n-C10H22	4.00E-04	
i-C10H22	1.92E-02	
C10H20 (olef)	2.40E-03	
C10H20 (naph)	3.50E-03	
C10H14	7.70E-02	
i-C11H24	8.90E-03	
C11H16	2.23E-02	
C12+	9.30E-03	